

Global Reaction Kinetics for Oxidation and Storage in Diesel Oxidation Catalysts

by

Chaitanya S. Sampara

A dissertation submitted in partial fulfillment
of the requirements for the degree of
Doctor of Philosophy
(Mechanical Engineering)
in The University of Michigan
2008

Doctoral Committee:

Professor Dionissios N. Assanis, Co-Chair

Edward J. Bissett General Motors Research and Development, Co-Chair

Professor Panos Y. Papalambros

Professor Philip E. Savage

Professor Johannes W. Schwank

*Shree Rama Rama Rameti
Rame Raame Manorame
Sahasra Naama Tat Tulyam
Rama Nama Varanane*

- Vishnu Sahasranamam

© Chaitanya Sampara 2008
All Rights Reserved

DEDICATION

To my parents Sanku and Shobha, and my grandmothers
Prabhavathi and Subhadra Devi for teaching me the way of life.

ACKNOWLEDGEMENTS

There are several people who have guided and supported me over the course of my journey towards a doctoral degree. I am grateful to everyone of them.

I would like to thank my co-advisor Professor Dennis Assanis who has been a source of support and inspiration throughout my graduate student career. His engines class, ME 438, is probably the best course I have ever taken at the University of Michigan. He introduced me to engine aftertreatment catalysis through the General Motors Collaborative research labs, and I will be ever grateful for his support, trust and friendship.

I would like to thank Dr. Edward Bissett, my co-advisor, for being a father away from home. I do not have enough words to describe my gratitude towards him for teaching me how to not only be a better researcher and but also a better person. I would like to thank him for sharing his office space at GM R&D for the past 3 years, and for all the lunch money and pop he lent me over this period of time. I promise to remember and use everything he taught me about modeling, kinetics, math, life and love throughout my life.

I would like to thank my other committee members Professor Johannes Schwank, Professor Philip Savage and Professor Panos Papalambros for agreeing to serve on

my doctoral committee. I would also like to acknowledge Professor Zoran Filipi at UM for his support and help during the last stages of my doctoral work.

I would like to thank several people at GM R&D for teaching me the nuances of industry research. I would like to thank Calvin Koch for patiently teaching and assisting me in understanding the functioning of the bench scale reactor. I would like to thank Dr. Richard Blint for taking care of several bureaucratic details and helping me in conducting my research at GM R&D. This work would not have been possible without his involvement. I would like to thank Dr. Se Oh for his astute critique and invaluable advice about each of the pieces of my work. Every discussion I had with him has been a source of inspiration.

I would like to thank Dr. Alex Knaff for his friendship and advice on a number of things. I would also like to appreciate his help for answering any questions regarding the engine data that is shown in this document.

I would like to thank Dr. Chris Depcik who took me under his wing when I first came to Michigan and helped me with my research work. Also thanks to Dr. Aris Babajimopolous for all the interesting discussions on a variety of topics at odd hours. I would like to thank my peers at the Walter E. Lay Automotive Laboratory without whom this experience would not have been complete. My sincere thanks to Chandra, Orgun, Jason, Jonathan, Rob, Alberto, Manbae, Mark, Ashwin and many others. May the good times always roll!

I have made several new Indian friends over the course of my stay in Ann Arbor.

I would like to thank Shak, Jaggi, Shrav, Bharti and Umang for their friendship and love. I would like to thank the foodfun group - Dhruv, Yusuf, Hima, Vaishno, Malavika and Aniket for all the fun times. Indian classical music and dance group has been a source of inspiration and comfort. I would like to thank everyone who has been involved with me in this group. Special thanks to Ravi (Dr. Subramanian) for encouraging me to play the flute. Special thanks also to Ashish (Dr. Deshpande) for motivating me learn TeX and playing with me for most of the ICMD concerts. You guys are awesome!.

My undergraduate friends Guru, Manoj, Parikshit, Raju and Madan have always been there to support me. My sincere thanks to them.

A big “Thanks” to my family for their support. My greatest thanks to my grandmothers Subhadra Devi and Prabhavati who taught me so much about life. I would also sincerely like to thank my parents Shankar Kumar and Shobha and my sister Sathya for putting up with my stubbornness and supporting me through ups and downs in life.

Last but not least, I would like to thank Suparna for her support and love over the past several years. My sincere thanks to her for putting up with my stubbornness, idiosyncracies and outright craziness (at times), and helping me to get through my graduate student career.

TABLE OF CONTENTS

DEDICATION	ii
ACKNOWLEDGEMENTS	iii
LIST OF FIGURES	ix
LIST OF TABLES	xiii
LIST OF SYMBOLS	xv
ABSTRACTxviii
CHAPTER	
I. Introduction	1
1.1 Diesel Engine Emissions	1
1.2 Environmental Regulations	3
1.3 Advanced Combustion Strategies - Low Temperature Com- bustion (LTC)	7
1.4 Diesel Aftertreatment	9
1.4.1 NO _x Abatement - LNT and SCR	10
1.4.2 PM Abatement - Diesel Particulate Filter	14
1.4.3 HCs and CO oxidation and more - Diesel Oxidation Catalyst	14
1.5 Kinetics Modeling for Aftertreatment Systems	17
1.6 Thesis Objectives	21
1.7 Thesis Outline	21
II. Global kinetics for a platinum diesel oxidation catalyst with one exhaust hydrocarbon	24
2.1 Introduction	24
2.2 Experimental	28
2.2.1 Concentration/Temperature Domain	28
2.2.2 Pre-testing Catalyst Preparation	30
2.2.3 Reactor Setup	30

2.2.4	Analysis	31
2.3	Modeling	33
2.3.1	Scaling of Species Equations	36
2.3.2	Scaling Optimization Parameters	37
2.3.3	Definition of Objective Function	39
2.4	Results and Discussion	42
2.4.1	C ₃ H ₆ , CO and H ₂ Oxidation	42
2.4.2	NO Oxidation	45
2.4.3	Optimization of the Full Problem	49
2.4.4	Engine Validation	55
 III. Global kinetics for a commercial diesel oxidation catalyst with two exhaust hydrocarbons		 59
3.1	Introduction	59
3.2	Experimental	62
3.2.1	Definition of Test Matrix	62
3.2.2	Pre-testing	64
3.2.3	Reactor Set-up	64
3.3	Modeling	66
3.3.1	Inner Problem	67
3.3.2	Transport Property of Diesel Fuel	68
3.3.3	Outer Problem	71
3.4	Results and Discussion	73
3.4.1	Initial Rate Forms and Guesses for Optimization	73
3.4.2	NO Oxidation	74
3.4.3	Optimization of the Full Problem	77
3.4.4	Reactor Validation	86
3.4.5	Engine Validation	87
3.5	Conclusions	90
 IV. Hydrocarbon storage modeling for diesel oxidation catalysts		 94
4.1	Introduction	94
4.1.1	Test Matrix	100
4.1.2	Reactor Set-up and Analysis	101
4.1.3	Typical Experimental Results	104
4.2	Modeling	104
4.2.1	Equilibrium Calculations	107
4.2.2	Transient Calculations	110
4.2.3	Validation	114
4.2.4	Full Scale 1D Adiabatic Reactor Model	117
4.3	Results and Discussion	118
4.3.1	A Representative Storage + Oxidation Catalyst	120

4.3.2	Effect of Heat-up Rate	122
4.3.3	Varying Heat-up Rates	126
V.	Conclusions and Future Work	133
5.1	Conclusions	133
5.2	Thesis Contributions	137
5.3	Recommendations for Future Work	138
BIBLIOGRAPHY	140

LIST OF FIGURES

Figure

1.1	Production and composition of particulate matter (PM)	2
1.2	United States Environmental Protection Agency proposed legislation for NO_x vs. PM and HCs and CO	4
1.3	European Union Regulations on Diesel Engine Emissions	6
1.4	Corporate Average Fuel Economy performance for passenger cars and light trucks (National Highway Traffic Safety Administration, 2007)	6
1.5	Structure of the monolithic catalytic converter	10
1.6	Typical design of a Diesel Particulate Filter used to reduce PM emissions in diesel engines	14
1.7	1D representation of the monolith - film approach	18
2.1	Experimental set-up of the bench scale reactor for DOC kinetics development - Platinum catalyst and C_3H_6 as HC	32
2.2	x_g comparison between model and experiment	40
2.3	Δx_g comparison between model and experiment	41
2.4	Initial guess for $A_{\text{C}_3\text{H}_6}$ and $E_{\text{C}_3\text{H}_6}$ from optimization at individual temperatures	46
2.5	Comparison of Δx_{NO} between model and experiment for cases which has only NO, NO_2 and O_2 in feed-stream (no reductant)	47
2.6	Comparison of Δx_{NO} between model and experiment (all temperatures) in the presence of reductants in the feed-stream using the rate form of equation 2.4.5.	48

2.7	Comparison between experiment and model predictions - Δx_g and x_g^{exit} for C_3H_6	52
2.8	Comparison between experiment and model predictions - Δx_g and x_g^{exit} for CO	53
2.9	Comparison between experiment and model predictions - Δx_g and x_g^{exit} for H_2	53
2.10	Comparison of Δx_g for NO between experiment and model predictions - Feeds with and without reductant	54
2.11	THC validation with engine generated light-off curves	56
2.12	CO validation with engine generated light-off curves	56
3.1	Experimental set-up of the bench scale reactor for DOC kinetics development - Commercial catalyst with C_3H_6 and DF as representative HCs	66
3.2	Experimental conversion plotted against transport limited conversions for DF with $\Sigma_{DF} = 289$	69
3.3	Experimental conversion plotted against transport limited conversions for DF with $\Sigma_{DF} = 80$	70
3.4	Initial guess for A_{DF} and E_{DF} from optimization at individual temperatures	75
3.5	Comparison of Δx_{NO} between model and experiment for cases which has only NO, NO_2 and O_2 in the feed-stream (no reductant)	76
3.6	Comparison of Δx_{NO} between model and experiment in the presence of reductants in the feed-stream using the rate form of equation (2.4.5).	77
3.7	Comparison of NO light-off curves between model which used NO rate based on CO and NO inhibition and small-scale reactor experiments. The inlet NO was 40 ppm.	80
3.8	Comparison of NO light-off curves between model which used NO rate based on DF and NO inhibition and reactor small-scale experiments	81

3.9	Comparison between experiment and model predictions - Δx_g for DF	84
3.10	Comparison between experiment and model predictions - Δx_g and x_g^{exit} for C_3H_6	85
3.11	Comparison between experiment and model predictions - Δx_g and x_g^{exit} for CO	85
3.12	Comparison between experiment and model predictions - Δx_g and x_g^{exit} for H_2	86
3.13	Comparison between experiment and model predictions - Δx_g for NO - Feed consists of points with and without reductant	86
3.14	Model validation with reactor data under simulated exhaust conditions at $60,000\text{ h}^{-1}$ for DF and C_3H_6	88
3.15	Model validation with reactor data under simulated exhaust conditions at $60,000\text{ h}^{-1}$ for CO and H_2	89
3.16	Model validation with engine data obtained for 2300rpm with engine employing conventional combustion	91
3.17	Model validation with engine data obtained for 2300rpm with engine employing PCI combustion	92
4.1	Experimental set-up of the bench scale reactor for HC storage kinetics development	102
4.2	Typical adsorption/desorption experimental results for dodecane (a) and toluene (b)	105
4.3	Measured temperatures during the three phases of the experiment	106
4.4	Langmuir isotherms generated with the four concentration and two temperature combinations	110
4.5	Arrhenius plot of the ratio of rate constants	111
4.6	Experimental results and model predictions during adsorption phase for the four test points at the optimized value of $A_{ads} = 13.5$. All concentrations are ppm dodecane on a C_{12} basis.	115

4.7	Validation using desorption data. All concentrations are ppm dodecane on a C ₁₂ basis.	116
4.8	DF1 emissions for a 10°C/min ramp rate	123
4.9	Profiles at various times when the inlet gas phase temperature is ramped up at 10°C/min	124
4.10	Rate plots for varying ramp rates for inlet gas temperature	127
4.11	DF1 (adsorbable hydrocarbon) emissions for varying ramp rates	128
4.12	η comparison for varying heat-up rates and space velocities	129
4.13	η comparison for varying heat-up rates and CO concentrations	130

LIST OF TABLES

Table

2.1	Concentration and temperature levels for various species	28
2.2	Concentration constraints for test matrix	29
2.3	NO, NO ₂ and O ₂ concentration levels	30
2.4	Final norm values after various terms in the inhibition terms were removed	49
2.5	Rate constants as a result of the final optimization of the full problem	52
3.1	Test matrix for simulated exhaust; THC = DF+C ₃ H ₆	63
3.2	Constraints for generating the test matrix; THC = DF+C ₃ H ₆	63
3.3	NO, NO ₂ and O ₂ concentration levels	64
3.4	Final norm after various terms in the inhibition terms were dropped	78
3.5	Rate constants as a result of the final optimization of the full problem - Final norm = 0.4529 and DF is C _{14.6} H _{24.8}	83
3.6	Heats of combustion	84
3.7	Inlet conditions for light-off curves generated with small-scale reactor with realistic space velocities	87
4.1	Test matrix for generating a Langmuir isotherm	101
4.2	$n_{eq,DF1}$ calculated for the experimental combinations of temperature and n-dodecane concentration. Concentrations were evaluated at the 1.15 atm of the experiments	109
4.3	Catalyst parameters for storage + oxidation studies	120

4.4	Species inlet concentrations for storage + oxidation studies	121
-----	--	-----

LIST OF SYMBOLS

a_j	active site density for reaction j	$\text{mol-site} \cdot \text{m}^{-3}$
a_{ze}	storage site density	$\text{mol-site} \cdot \text{m}^{-3}$
A	face area	m^2
A_{ads}	rate constant for adsorption	$\text{m}^3 \text{mol}^{-1} \text{s}^{-1}$
A_{des}	rate constant for desorption	s^{-1}
A_i	pre-exponential for rate constant	$\text{m}^6 \text{mol}^{-1} \text{mol-site}^{-1} \text{s}^{-1}$
Aa_i	pre-exponential for adsorption constant	$\text{mol}^{-1} \text{m}^{-3}$
c	total molar concentration of gas	$\text{mol} \cdot \text{m}^{-3}$
c_{pg}	molar specific heat of gas	$\text{J} \cdot \text{mol}^{-1} \text{K}^{-1}$
$C_{ps, sb}$	specific heat of substrate	$\text{J} \cdot \text{kg}^{-1} \text{K}^{-1}$
$C_{ps, wc}$	specific heat of washcoat	$\text{J} \cdot \text{kg}^{-1} \text{K}^{-1}$
c_R	total molar concentration at 1 atm	$\text{mol} \cdot \text{m}^{-3}$
$\vec{c}_s, c_{s,i}$	vector and component, respectively, of molar concentration of trace species at catalyst surface	$\text{mol} \cdot \text{m}^{-3}$
D_h	hydraulic diameter of channel	m
$D_{i,m}$	binary diffusion coefficient of species i in the mixture	$\text{m}^2 \text{s}^{-1}$
$DF1$	hydrocarbon component which can be both adsorbed and oxidized	
$DF2$	hydrocarbon component which can be oxidized but not adsorbed	
E_i	activation energy for rate constant	$\text{J} \cdot \text{mol}^{-1}$
Ea_i	activation energy for adsorption constant	$\text{J} \cdot \text{mol}^{-1}$
E_{des}	activation energy for desorption constant	$\text{J} \cdot \text{mol}^{-1}$
f_{sb}	solid fraction of the substrate	
f_{wc}	solid fraction of the washcoat	
G, G_1, G_2	inhibition terms in rate expressions	
h	interphase heat transfer coefficient	$\text{J} \cdot \text{m}^{-2} \text{s}^{-1} \text{K}^{-1}$
K	ratio of rate constants for adsorption-desorption	$\text{mol} \cdot \text{m}^3$
k_i	rate constant	varies
\bar{k}_i	rate constant for rates in Oh <i>et al.</i>	$\text{mol} \cdot \text{K}^{-1} \text{cm}^{-2} \text{s}^{-1}$
$k_{m,i}$	mass transfer coefficient for species i	$\text{mol} \cdot \text{m}^{-2} \text{s}^{-1}$

K_i	adsorption constant for species i	$\text{m}^3 \cdot \text{mol}^{-1}$
\bar{K}_i	adsorption constant for rates in Oh <i>et al.</i>	
K_{eq}	equilibrium constant for NO-NO ₂ reaction	
L	length of reactor	m
M_i	molecular weight of species i	$\text{kg} \cdot \text{mol}^{-1}$
n_{DF1}	number of moles of DF1 adsorbed on the zeolite surface	mol
$n_{eq,DF1}$	number of moles of DF1 adsorbed on the zeolite surface at equilibrium	mol
\dot{n}_{DF1}	mole flow rate of DF1	$\text{mol} \cdot \text{s}^{-1}$
N_{tot}	total number of moles of zeolite available for storage	mol
p	total pressure	$\text{N} \cdot \text{m}^{-2}$
R	gas constant	$\text{J} \cdot \text{mol}^{-1}\text{K}^{-1}$
r_{ads}	adsorption rate onto zeolite	$\text{mol} \cdot \text{mol}^{-1}\text{site}^{-1}\text{s}^{-1}$
r_{des}	desorption rate from zeolite	$\text{mol} \cdot \text{mol}^{-1}\text{site}^{-1}\text{s}^{-1}$
r_j	rate of production of reaction j	$\text{mol} \cdot \text{mol}^{-1}\text{site}^{-1}\text{s}^{-1}$
S	surface area per reactor volume	m^{-1}
Sh	Sherwood number for mass transfer	
$s_{i,j}$	stoichiometric coefficient of species i in reaction j	
T	temperature	K
T_g	temperature of bulk gas phase	K
T_s	temperature of solid phase	K
T_r	reference temperature	K
V	volume of reactor	m^3
w	molar flow rate	$\text{mol} \cdot \text{s}^{-1}$
\mathcal{W}	inlet mass flow rate	$\text{kg} \cdot \text{s}^{-1}$
w_r	reference molar flow rate	$\text{mol} \cdot \text{s}^{-1}$
wsb	substrate wall thickness	m
wwc	washcoat wall thickness	m
x_i^0	inlet mole fraction of species i	
$x_{g,i}$	mole fraction of species i in bulk gas phase	
$x_{i,r}$	reference mole-fraction of species i	
$x_{s,i}$	mole fraction of species i in gas at catalyst surface	
z	axial position	m
ΔG	free energy for the NO-NO ₂ reaction	$\text{J} \cdot \text{mol}^{-1}$
ΔH	Enthalpy of reaction	$\text{J} \cdot \text{mol}^{-1}$
Δx_g	change in mole fraction across the reactor	
λ_g	thermal conductivity of gas	$\text{J} \cdot \text{m}^{-1}\text{s}^{-1}\text{K}^{-1}$
λ_{sb}	thermal conductivity of substrate	$\text{J} \cdot \text{m}^{-1}\text{s}^{-1}\text{K}^{-1}$
$\vec{\theta}, \theta_k$	vector and component, respectively, of surface coverages	

ρ_{sb}	density of substrate	$\text{kg} \cdot \text{m}^{-3}$
ρ_{wc}	density of washcoat	$\text{kg} \cdot \text{m}^{-3}$
ψ_s	effective heat capacity of reactor (defined by eq. 4.2.17)	$\text{J} \cdot \text{m}^{-3}\text{K}^{-1}$
Σ_i	diffusion volume of species i	

ABSTRACT

Global Reaction Kinetics for Oxidation and Storage in Diesel Oxidation Catalysts

by
Chaitanya S. Sampara

Chairs: Dionissios N. Assanis and Edward J. Bissett

Realizing the need for effective kinetic models that could be used over wide operating regimes, oxidation and storage kinetics for a diesel oxidation catalyst (DOC) were developed in this work. As a first step towards kinetics development, a simple catalyst formulation including only Platinum was chosen. Kinetics were generated by assuming that propylene was representative all the hydrocarbons (HCs) in the exhaust. A systematic methodology was formulated which consisted of (1) careful choice of concentration/temperature domain (2) measurement of reactor conversions of aged catalyst samples at chosen test points using a high space velocity integral reactor (3) developing a simplified 1D reactor model (4) defining an objective function which is critically sensitive to the differences between model predictions and experiments at all conversions (5) generating proper initial guesses and finally (6) modifying Langmuir-Hinshelwood rate expressions to arrive at the final rate forms. This methodology can be used to generate steady state global kinetics in general.

Comparison of model predictions with light-off curves generated using a 1.7L Isuzu diesel engine revealed that propylene is not representative of all the HCs in the diesel exhaust. As a next step towards oxidation kinetics development, a commercially available DOC catalyst was used with HCs in the diesel exhaust speciated as propylene, representing partially oxidized HCs, and diesel fuel, representing unburnt fuel component in diesel exhaust. The systematic methodology developed previously was successfully used to generate oxidation kinetics for all the species of interest. Light-off curves comparison revealed excellent agreement between model predictions and engine data. Finally, reaction kinetics were developed for capturing hydrocarbon adsorption/desorption processes on zeolite. For this study the fuel components in the exhaust were further speciated as n-dodecane and toluene. A minimum of four experiments were found to be sufficient to generate the necessary kinetic constants for each adsorbable HC species. Studies on simplified warm-up process using a 1D adiabatic reactor model that incorporated both the oxidation and storage kinetics indicated that the storage component reduces the overall cold start HC emissions by at least a factor of 2 if the warm-up rate achieves 45-65°C/min, a range commonly observed during start-up.

CHAPTER I

Introduction

The modern diesel engine (DE) is one of the most versatile power sources available for automotive applications. The high fuel economy and torque benefits coupled with excellent drivability of the turbo-charged DE is leading to its global use in heavy and light duty applications. The DE has superior thermal efficiency than its gasoline counterpart owing to its increased compression ratio. Also, fuel is directly injected into the cylinder based on the accelerator pedal position, thus minimizing the throttling losses in a DE. Krieger *et al.* [1] report that the fuel consumption for diesel is 35% lower than a similar gasoline engine.

1.1 Diesel Engine Emissions

The DE, along with these advantages of superior performance, presents a very challenging problem in terms of its emissions reduction and control. Typical DE emissions consists of four major components, namely, particulate matter (PM), oxides of nitrogen (collectively referred to as NO_x), hydrocarbons (HCs) and CO. These exhaust components are typically present in an oxygen rich environment, at temperatures ranging between $\sim 150^\circ\text{C}$ - 450°C .

PM in diesel exhaust consists mainly of agglomerated solid carbonaceous material and ash, with condensed volatile organic and sulfur compounds on the periphery. A simple illustration of particulate matter and its composition are shown in figure 1.1(a) and 1.1(b) [2]. PM has adverse effects on human health and is reported to cause lung inflammation, reduced vision and cancer [3].

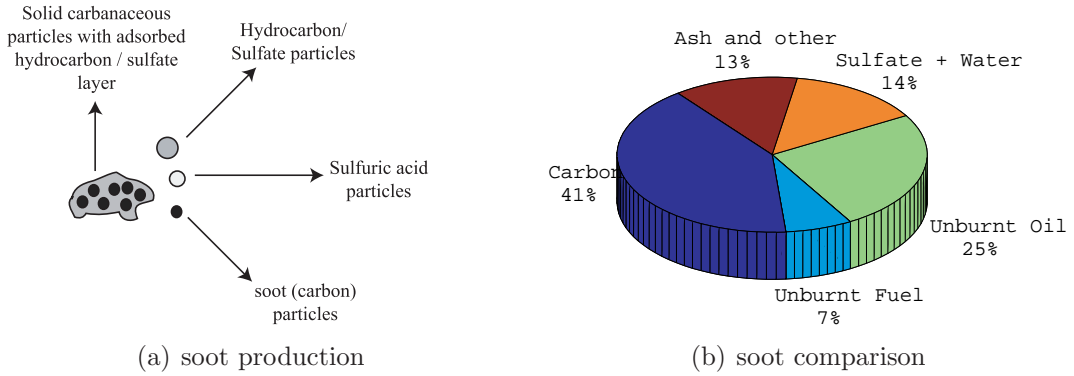
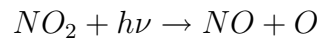
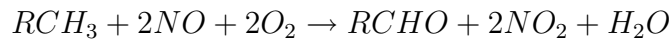


Figure. 1.1: Production and composition of particulate matter (PM)

The oxides of nitrogen, mainly, NO and NO₂, are collectively referred to as NO_x. NO_x is produced in the combustion process (expansion stroke of the engine) due to the reaction of N₂ with O₂ at elevated temperatures (> 1800K) based on the popular extended Zeldovich mechanism [4]. NO_x is a major factor in environmental pollution where it reacts with volatile organic fraction (VOC) to form ozone (O₃) smog. The overall reaction between VOC and NO (the main NO_x component) leading to the production of O₃ is given as follows:



(1.1.1)

Here RCH_3 and $RCHO$ are the HCs involved and M is a “third body” that removes energy that would otherwise cause the dissociation of O_3 . Ozone causes inflammation in the respiratory tract; it reduces forced capacity and worsens airflow, specifically for people with asthma. In addition to these adverse effects of PM and NO_x , there exists an inverse relation between their production in the cylinder, wherein the factors commonly known to reduce the production of one of the components promotes the production of the other.

For DEs which utilize conventional modes of combustion, the concentration levels of HCs (on a C_3 basis) and CO in the exhaust are typically 700 ppm and 1200 ppm respectively. However, these concentrations can be as high as 3000 ppm and 5000 ppm for some advanced combustion modes, such as pre-mixed compression ignition (PCI) (see section 1.3), currently being employed to simultaneously reduce both PM and NO_x from the exhaust. It has also been well reported in the literature that exposure to high concentrations of HCs and CO causes respiratory inflammations, allergy response, airflow limitations and asthmatic disorders [5],[6].

1.2 Environmental Regulations

Owing to these problems from the various engine emissions, the Environmental Protection Agency (EPA) in the United States and the European Emissions Standards in European Union established regulations for all the four emissions components.

The EPA established its standards for HCs, CO, NO_x and PM based on the Clean Air Act Ammendments (CAAA) of 1990 as Tier 1 emissions standards which were

phased in progressively between 1994 and 1997 [7]. Standards were established based on the engine i.e. gasoline or diesel, and on the weight of the vehicle i.e., passenger car, light-duty vehicle or heavy-duty vehicle. The Tier 2 regulation introduced more stringent numerical emission limits relative to the previous Tier 1 requirements. Under the Tier 2, the same upper bounds for each of the emissions components were applied to all vehicle weight categories, i.e., cars, minivans, light-duty trucks, and SUVs. These standards are being phased in between 2004 and 2009. There are eight different classification bins in the Tier 2 regulation. While any vehicle can operate in any one of the 8 certification levels, the fleet average must be within Bin 5. A comparison between Tier 1 and Tier 2, Bin 5 emission levels is shown in figure 1.2. The maximum sulfur that could be present in the diesel fuel was also reduced to

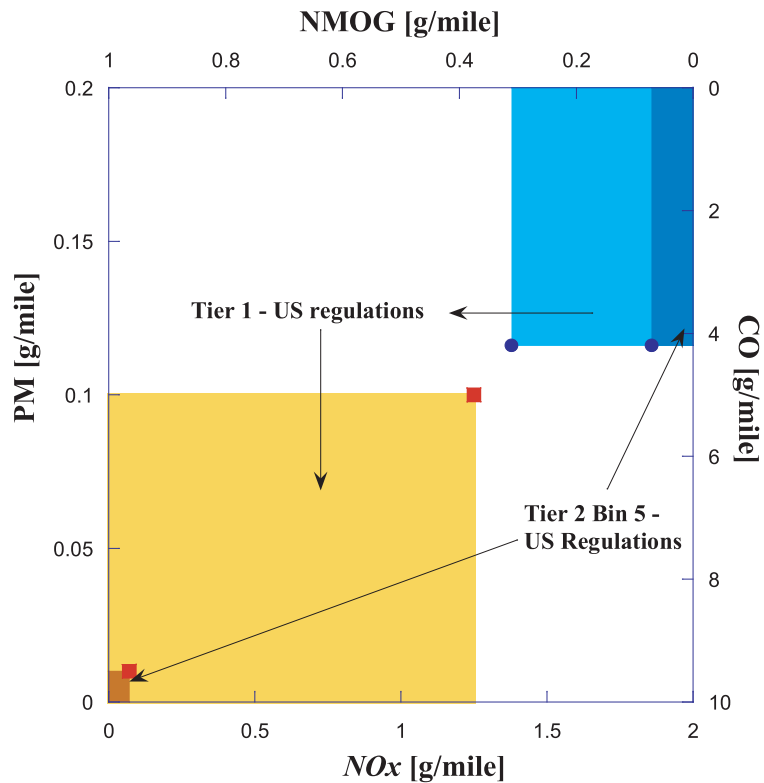


Figure. 1.2: United States Environmental Protection Agency proposed legislation for NO_x vs. PM and HCs and CO

15 ppm. The vehicle is also needed to maintain these emissions levels for a span of 120,000 miles, and should not exceed 150% of these bounds for 250,000 miles. A more detailed description of the emissions standards for each of the two stages can be found in [7].

The standards set by the EU were first established as Euro 1 standards in 1993 based on the Directive 70/220/EEC. These have been modified over the years and the Euro 5 which have been established in 2007 will phase-in before 2009. In contrast to the Tier 1 regulations, Euro 1 standards imposed a combined limit on the HCs and NO_x . The current Euro 5 standards have a limit on both the HC+ NO_x level and the total NO_x . Vehicles are classified based on the weight as passenger cars and light or heavy commercial vehicles and each classification had its own bound for the various emissions. Sulfur free diesel fuel was supposed to be made available by 2005 and, is mandatory by 2009. A comparison between Euro 1 and Euro 5 emissions is presented in figure 1.3.

In addition to these emissions regulations, the Corporate Average Fuel Economy standards were established in 1978 in response to the oil crisis in 1973-74, with a goal to double new car fuel economy by model year 1985. Since CO_2 is directly proportional to the amount of fuel burnt in the engine, increasing the fuel economy would also decrease the CO_2 emissions. The CAFE performance from 1978 through 2007 for passenger and light trucks is illustrated in figure 1.4.

To meet these ever increasing standards for reduced emissions and improvements in fuel economy, researchers around the world are exploring advanced combustion

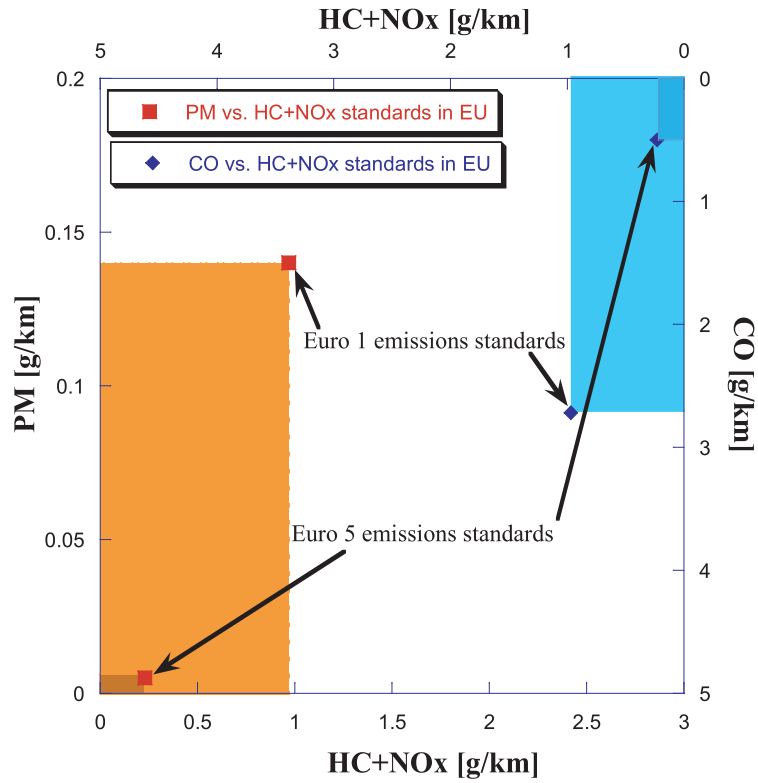


Figure. 1.3: European Union Regulations on Diesel Engine Emissions

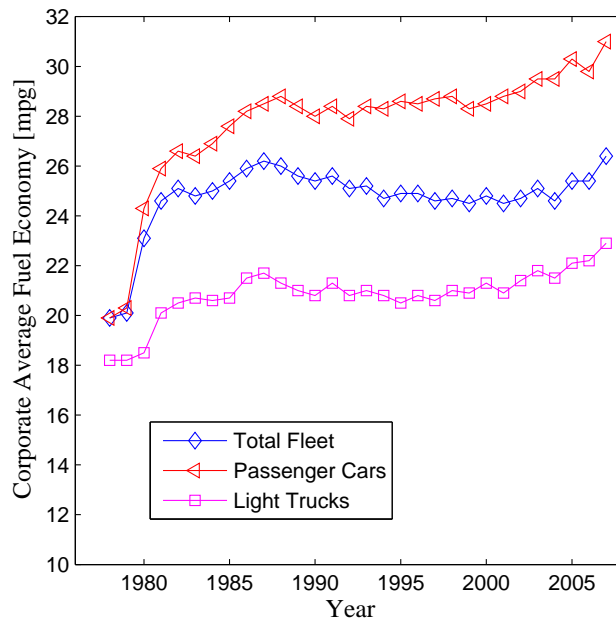


Figure. 1.4: Corporate Average Fuel Economy performance for passenger cars and light trucks (National Highway Traffic Safety Administration, 2007)

modes and the development of complex aftertreatment systems. The strategies which are currently being employed in the automotive industry for DE emissions reduction are discussed briefly in the following sections.

1.3 Advanced Combustion Strategies - Low Temperature Combustion (LTC)

Due to the heterogeneous nature of the fuel and air mixture in the combustion chamber of a DE, local temperatures in the combustion zones are much higher than the bulk gas temperatures. It is well reported in the literature that NO_x is typically formed in or around the flame at around ~ 2000 K [8], and soot is formed starting at equivalence ratios of ~ 2 [8] at temperatures greater than 1500 K but less than 2300 K. So, while NO_x production can be reduced by avoiding high local gas temperatures, PM can be reduced by ensuring that no fuel rich pockets are present. A combination of the following strategies are currently being employed to reduce the heterogeneity of the fuel-air mixture and local gas temperature in the cylinder to simultaneously reduce the formation of PM and NO_x .

- Injection Timing (Retard/Advance)
- Split Injection
- Reduced Compression Ratio
- Charge Air Cooling
- Water-Fuel Emulsions
- Exhaust Gas Recirculation (EGR)

While these strategies provide a way to reduce emissions, they also reduce the overall combustion efficiency.

Premixed Compression Ignition - PCI

The most popular advanced combustion mode which is proven to reduce PM and NO_x emissions simultaneously in the mid-speed, mid-load range for diesel engines is the Premixed Compression Ignition (PCI) combustion [9], [10], [11]. In this mode the fuel-air mixture homogeneity is increased by elevated injection pressures, charge motion and extended ignition delay times. Due to the high cetane number of the diesel fuel, it is never possible to obtain a truly premixed combustion. Local gas temperatures are reduced by lowering the compression ratio, using large amounts of cooled EGR and retarding combustion phasing.

Despite the inherent advantages of the PCI combustion concept in terms of PM and NO_x reduction, numerous obstacles exist in its implementation for commercial use. The poor volatility of diesel fuel in low temperature environments limits fuel and air mixing. For the existing compression ratios, the high cetane number of diesel fuel leads to early auto-ignition, resulting in excessive knock [12]. Decreasing the compression ratio leads to lower gas temperatures which in-turn lead to lower Carnot efficiency. The high levels of EGR and advancement of fuel injection lead to higher HC and CO emissions [13], and additional means to effectively reduce these species is required. The use of EGR also reduces the specific heat ratio for the combustion gases (γ), thus reducing the thermal efficiency. HCs in EGR are known to be soot precursors and hence increase the overall PM production. These problems are mag-

nified when this concept is applied to high load conditions and hence this concept is more suited for medium and low load operating range.

1.4 Diesel Aftertreatment

The production of high levels of NO_x and PM from conventional diesel combustion, and high levels of HCs and CO from advanced combustion modes such as PCI, and a need to reduce these emissions to comply with the emissions regulations, has necessitated the use of complex catalytic systems. These catalytic systems, also commonly referred to as aftertreatment systems, use a solid catalyst to accelerate various reactions which help reduce these reactants to unharmed products.

A typical converter design illustrated in figure 1.5, consists of monoliths coated with catalytic material, and placed in a steel canister. These monoliths have a number of parallel channels to facilitate the gas flow in the axial direction, and are made up of either ceramic or metal substrates. The substrates provide a high geometric surface area for gas contact. This substrate is coated with highly porous inorganic oxides such as $\gamma\text{-Al}_2\text{O}_3$, SiO_2 or ZrO_2 , that can retain the noble metal. Noble metals such Pt, Pd, Rh etc., are then deposited on the washcoat. Exhaust gas flowing through the catalytic converter diffuses to the catalyst surface where heterogeneous reaction takes place. The following section discusses briefly the various aftertreatment technologies currently being employed to reduce the various emissions in DEs. A combination of these components is currently being used to reduce tailpipe emissions.

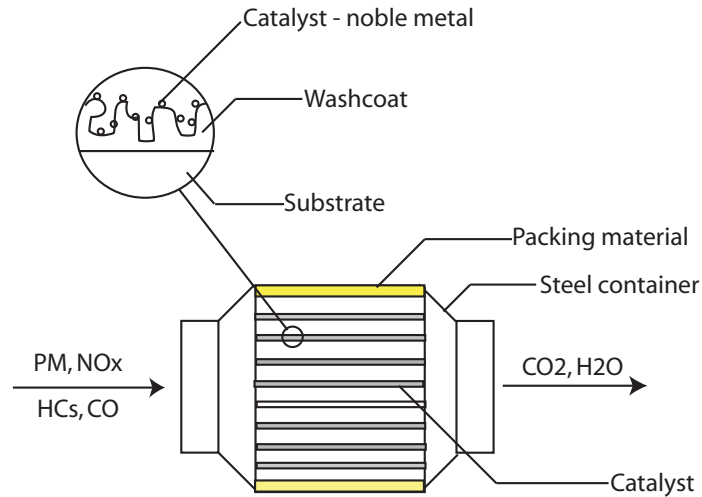


Figure. 1.5: Structure of the monolithic catalytic converter

1.4.1 NO_x Abatement - LNT and SCR

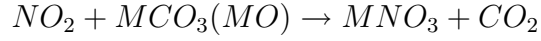
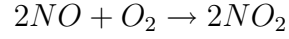
The use of EGR as a diluent during cylinder combustion is the most convenient method to reduce NO_x emissions. However, since increased EGR leads to higher PM emissions, there is a trade-off with the use of EGR for NO_x control. The Lean NO_x trap and selective catalytic reduction are the two popular alternatives to catalytically reduce the NO_x from the exhaust to harmless N₂, even at low exhaust gas temperatures. These two NO_x reduction components are discussed below.

Lean NO_x trap - LNT

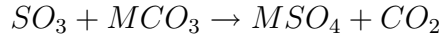
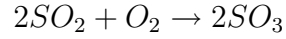
A LNT catalyst consists of an alkali or alkaline earth metal oxide or carbonate mixed with a noble metal (typically Pt) on the same washcoat. During lean operation (excess oxygen), the NO oxidizes to NO₂ in the presence of the noble metal catalyst. The NO₂ then chemisorbs onto the metal oxide or metal carbonate forming metal nitrate. Over a period of time all the metal oxide (carbonate) is consumed to form nitrate. Hence, it has to be periodically regenerated, where the nitrate decomposes

back to metal oxide (carbonate).

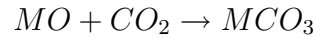
Desirable reactions during lean operation



Undesirable reactions during lean operation



Desirable reactions during rich operation



(1.4.1)

This regeneration is generally obtained by creating a rich environment with high levels of HCs or CO or H₂. The NO formed due to the decomposition of the nitrate reacts with the reductant to form N₂. The undesirable reactions under LNT operation are the oxidation of SO₂ to form metal sulfates.

NO oxidation to NO₂ occurs on the noble metal between 250 and 450°C. This reaction is kinetically limited below 250°C and thermodynamically limited beyond 450°C. Also the stability of the nitrate formed is severely limited beyond this temperature. There are two important problems with using an LNT for NO_x reduction. First, the saturated LNT with metal nitrate (MNO₃) should be periodically regenerated by providing a reducing environment, which contains high levels of HCs or

CO or both. This is typically achieved by running the engine rich or by having a secondary fuel injection late in the exhaust stroke. This involves additional fuel penalties, and complications with respect to control and design. Second, the sulfur in the fuel generally reacts with the metal carbonate or metal oxide to form metal sulfates (MSO_4). Reducing these back to its original form needs high temperatures of the order of 600°C [14].

Selective Catalytic Reduction - SCR

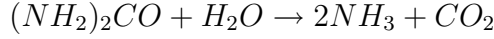
A number of different strategies have been researched for achieving SCR of NO_x to N_2 [15]. NO_x can be reduced by:

- Soot particulate
- Ammonia (Urea)
- Hydrocarbons over zeolite based catalysts
- Hydrocarbons over metal oxide catalysts
- Hydrocarbons over multi-staged catalysts
- Hydrocarbons over noble metal catalysts

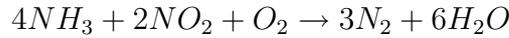
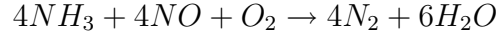
Among these options, the use of Ammonia and hydrocarbons over zeolite based catalyst are the most popular.

SCR of NO with ammonia (NH_3) under lean conditions is a widely commercialized technology for NO_x removal from stationary sources [15]. Vanadium based catalysts are commonly used for this application. Sources of NH_3 can be compressed gas, or

compounds such as urea ($(\text{NH}_2)_2\text{CO}$), which readily decompose to give NH_3 .



This hydrolysis reaction occurs at temperatures beyond 160°C . Over an SCR catalyst, NH_3 reacts with NO_x according to the following reactions.



(1.4.2)

Among the above reactions, the reaction of NH_3 with NO and NO_2 is most facile and therefore occurs at lower reaction temperatures. Thus, an external source which can provide a 1:1 $\text{NO}:\text{NO}_2$ ratio would be ideal to achieve best SCR performance.

Zeolite-based catalysts have received much attention due to their high activity and relatively wide temperature window since the 1990s [15]. Metal catalysts such as Pt [16], Copper (Cu) [17] Iridium (Ir) [18], and more recently Silver (Ag) [19], are mixed along with the zeolite on the same washcoat. The activity of these catalysts are closely related to the type of zeolite and their structure. As a rule of thumb, zeolite structures with lower acidity lead to smaller carbonaceous deposits, leading to higher NO_x conversions. HCs are trapped in the zeolite structures to increase the local HC concentration. NO is oxidized to NO_2 at the catalyst surface which contains noble metal. The NO_2 thus formed reacts with the trapped HCs to produce N_2 . The main obstacle to the use of this system is the hydrothermal stability of the zeolite. Also, this method presents a problem at higher temperatures where HC desorption

is significant, which reduces the local HC concentration at the catalyst surface.

1.4.2 PM Abatement - Diesel Particulate Filter

Substantial improvements in PM emission reduction is made possible by the use of a diesel particulate filter (DPF). More than an order of magnitude improvement has been reported [20]. The design of a DPF, which is traditionally a wall flow filter, is different when compared to the traditional automotive catalytic convertor. It consists of a honeycomb monolith structure made of porous material with alternate channels plugged at both ends so that exhaust gas is forced through the channel walls, trapping the PM in the process. An illustration of a DPF is shown in figure 1.6. The main

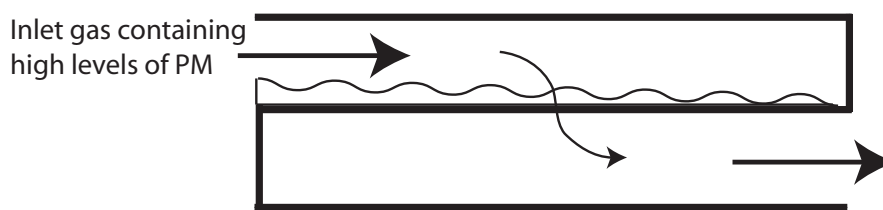


Figure. 1.6: Typical design of a Diesel Particulate Filter used to reduce PM emissions in diesel engines

challenge in the use of the DPF is the need for periodically regenerating the filter by oxidizing the PM which has accumulated during the trapping process. Although plenty of O_2 is available due to the overall lean engine operation, soot oxidation needs substantially high temperatures of the order of $600^\circ C$, and an external source is needed to supply this heat.

1.4.3 HCs and CO oxidation and more - Diesel Oxidation Catalyst

Currently all the diesel vehicles, particularly in Europe, are equipped with a diesel oxidation catalyst (DOC). The DOC will remain a principal aftertreatment device for future vehicles, either used alone or in conjunction with a more advanced

aftertreatment system [20]. Whereas the principal reactions in a DOC have some commonality with the three way catalytic convertor used in gasoline engines, the DOC's operation has a completely different operating regime.

HCs, CO and SOF oxidation

The primary function of a DOC is to oxidize the high levels of HCs and CO produced during advanced combustion modes such as PCI. The major reactions in a DOC are as follows:

- $C_nH_m + (n + \frac{m}{4}) O_2 \rightarrow n CO_2 + \frac{m}{2} H_2O$
- $CO + \frac{1}{2} O_2 \rightarrow CO_2$
- $NO + \frac{1}{2} O_2 \rightleftharpoons NO_2$
- $H_2 + \frac{1}{2} O_2 \rightarrow H_2O$

The exhaust is typically lean, implying high levels of O_2 concentrations of around 5-15%.

DPF Regeneration and LNT Desulfation

It has been previously discussed how the implementation of a DPF or an LNT in the diesel aftertreatment architecture needs the periodic regeneration of these components to enable their successful usage. The DOCs have been demonstrated for these purposes as a source of heat to oxidize the soot in the DPF [21], or decompose the metal sulfates formed in the LNTs [22]. Since the oxidation of HCs is highly exothermic, large quantities of HCs are provided upstream of the DOC by either

injecting fuel directly into the exhaust stream, or by injecting fuel late in the exhaust stroke within the cylinder. The primary concern for its use as a heat source, is however, to have a stable catalyst that can withstand the high temperatures over the entire life-cycle of the vehicle.

Cold Start HC Emissions

The use of zeolites to capture cold start HC emissions has been successfully demonstrated by several researchers ([23] [24] [25]). DOCs with the noble metal and the zeolite coated the same washcoat are being proposed for better heat management [26]. During cold-start when the noble metal is inactive for any reaction, the HCs are adsorbed on the zeolite pores. As temperature increases, these HCs desorb from the zeolite pores. However, for an optimally designed catalyst formulation, this desorption would occur only after the noble metal is active for reaction, thus providing very low HC emissions.

Catalyst Selection for DOCs

Platinum (Pt) is widely reported as the most active component in the removal of CO and HC from diesel exhaust [27], [28], [29], [30], [31]. However, upon exposure to high temperatures ($\sim 800^{\circ}\text{C}$), Pt coagulates, thus decreasing the number of sites available for reaction. Also, Pt promotes sulfate formation at low temperatures, which in-turn increases the PM in the exhaust [32]. Addition of Palladium (Pd) is proven to decrease the sulfate formation and also to stabilize the crystalline size over high temperature exposure [32], [28], [33], maintaining its dispersion over wide operating range [34].

For applications which commonly involve the removal of HCs and CO from the exhaust, a 2:1 Pt/Pd catalyst (wt basis) is used. This ratio has been proven to be successful over a wide operating regime [34]. For applications, where the DOC is used as a heat source (by burning the HCs in the exhaust), a 1:2 Pt/Pd catalyst (wt basis) is found to be more stable in its operation. Addition of ceria (CeO_2) is also reported to provide superior performance by lowering the light-off temperature [35], [36], [37]. Ceria is known to adsorb O_2 during lean excursions and release O_2 during oxygen deficient engine operation.

1.5 Kinetics Modeling for Aftertreatment Systems

Modern diesel aftertreatment systems consist of a NO_x reduction system - LNT or SCR, particulate trap - DPF and one or more DOCs depending upon the engine design and operating range [20]. Studying the various configurations needs accurate models for each of the sub-components over their entire domain of operation. 1D models have been successfully used for modeling the various exhaust aftertreatment components for gasoline and diesel applications [38], [63], [39], [66]. These models employ a ‘film approach’, which assumes that the monolith can be modeled as a single channel. It further divides the monolith interior into gas phase, where the bulk gas flows, and surface phase, where the reactant gas is adsorbed on the noble metal sites. A simple illustration of this idea is shown in figure 1.7.

Gas species which do not show any appreciable concentration gradients along the length of the reactor are termed as excess species, and the gases which exhibit

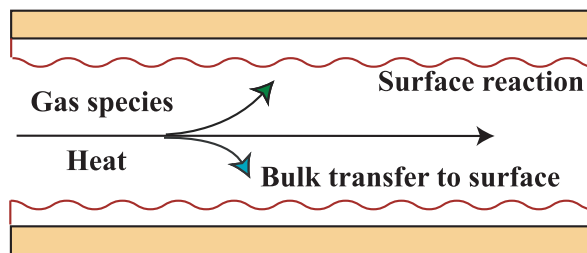


Figure. 1.7: 1D representation of the monolith - film approach

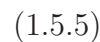
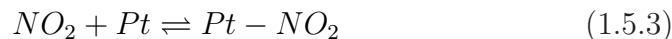
concentration gradients are termed as trace species. The equations for the species are written only for the trace species. Radial gradients for species concentrations and temperature resulting from the transport between the bulk gas and the surface are captured by asymptotic Nusselt and Sherwood numbers. This representation of transport has been found adequate since the internal pore diffusion resistance which occurs within the washcoat is negligible for the wall thicknesses commonly used for aftertreatment applications [40]. Accumulation of the mass and heat in the gas phase, and mass in the surface phase are neglected since their time constants are typically much smaller than the solid state temperature response [41]. The general equations used for the 1D reactor modeling are presented in chapter 4.

While these 1D models are known to well describe the heat and mass transfer effects, the biggest problem with their reliability and accuracy lies in having accurate reaction kinetics for all the reacting species over the specified catalyst. “Model development” for aftertreatment components often means “kinetics development”.

Micro-kinetics vs. Global kinetics

Reaction kinetics for a catalytic system can be developed by using either a micro-kinetic approach or a global kinetics approach. In the micro-kinetic approach a detailed reaction pathway between the reactants and products is described over the

specific catalyst. The rate constants for each of the elementary reactions in the overall reaction scheme are determined by fitting the experimental data to the reactor model. Typically pre-exponentials are determined from the kinetic gas theory [42]. The transition state theory is used to investigate whether the entropy changes due to adsorption are reasonable [42], [43]. Finally, the rate-limiting step is assigned to the step/steps that consumes the most free energy [44]. An example of micro-kinetic study for NO oxidation on Pt/Al₂O₃, adapted from Olsson *et al.* [58] is shown below:



The activation and pre-exponential values for each of these individual reaction change depending on the orientation of the noble metal (in this case Pt), and hence assumptions regarding the noble metal and reactant molecule orientation need to be made before suggesting a reaction scheme. In addition, the complexity of the problem increases tremendously once other species are included in the system, which might interfere with the behavior of a particular reactant molecule. Diesel exhaust, as described in the previous sections, consists of several different compounds and a micro-kinetic approach for the purpose of generating the oxidation kinetics for various species is nearly impossible.

An alternative procedure which is very popular in the exhaust aftertreatment kinetic modeling community is the global kinetics approach. With proper algebraic

manipulations, the reaction pathway described in equations 1.5.1 can often be described by single algebraic expression that is a function of the reactant concentrations. Owing to the complexity presented by the micro-kinetic approach, it is widely accepted that developing these algebraic expressions, which are also called global reaction kinetics, is a more practical way of generating kinetics for these systems. The kinetics are typically of Langmuir-Hinshelwood (LH) structured rate equations as described in equation 1.5.6.

$$r_i = \frac{A_i e^{\frac{-E_i}{RT}} c_i^{\alpha_i} c_j^{\beta_j}}{(1 + K_i e^{\frac{-\Delta H_i}{RT}} c_i + K_j e^{\frac{-\Delta H_j}{RT}} c_j)^{n_i} (1 + K_k e^{\frac{-\Delta H_k}{RT}} c_k)^{n_k}} \quad (1.5.6)$$

There are two different ways of generating steady state global reaction kinetics [45]. For the first method, reaction rates with little or no mass transfer effects, often referred to as differential rates, are measured over varying temperatures and reactant concentrations. A log-log plot of reactant concentration versus the rate is plotted for each of the temperatures, and based on these plots an empirical rate model is predicted. The experimental data is then fitted to the rate model to assess its performance over the wide operating range. This method is often employed when new rate forms need to be generated. In the second method, existing rate expressions from the literature are evaluated against experimental data generated over a specified catalyst. Rate constants are determined by minimizing the error between the assumed rate model predictions and the experimental data. Many researchers have used this modeling strategy successfully [46], [47], [48], [49], [50]. The major point to note when using the second approach is that the test matrix over which the rate expressions are calibrated should be representative of the range over which the model (device) would be used. The rate forms and constants can change appreciably when the operating regime is changed even slightly. Although this approach

presents additional challenges in terms of generating truly intrinsic kinetics (without mass transfer effects), prescribing a proper initial guess for the optimization of the various constants and minimizing the degrees of freedom for the optimization (rate forms), it is considered to be a realistic method to generate reaction kinetics for aftertreatment applications.

1.6 Thesis Objectives

Reliable steady state oxidation kinetics for HCs, CO, NO and H₂, and transient HC storage kinetics, which are applicable over a wide DOC operating range, have not been reported in the literature to the author's knowledge. Acknowledging the need for these kinetic models, the main objectives of this thesis are detailed as follows:

- Formulate a systematic methodology for the development of steady state global reaction kinetics and further apply the same to generate oxidation kinetics for the various species typically observed in the diesel exhaust over a DOC.
- For modeling purposes, generate a realistic representation for all the HCs in the diesel exhaust using minimum number of HC species.
- Generate a rate model which can accurately capture the transient adsorption and desorption processes of HCs on zeolites.
- Use simulation results from a model that contains both oxidation and storage capabilities to prescribe DOC design parameters

1.7 Thesis Outline

The motivation behind studying various emissions systems for diesel engine applications and the need for developing accurate reactor models (kinetics) are detailed

in chapter 1.

Chapter 2 discusses the development of global reaction kinetics for HCs, CO, H₂ and NO over a Pt DOC using C₃H₆ to represent HCs in the diesel exhaust. The development of an methodology which could be used to generate global reaction kinetics in general is detailed. Bench scale integral reactor set-up, modeling procedures and engine validation are discussed. Finally, the assumption that C₃H₆ could be used to represent all the HCs in the diesel exhaust is evaluated. The work reported in this chapter has been published as a journal in Industrial and Engineering Chemistry Research [51].

Chapter 3 discusses the development of global oxidation reaction kinetics over a commercial DOC using two hydrocarbons to represent all the HCs in the diesel exhaust. The methodologies developed in chapter 2 were used to develop these kinetics. Reaction kinetics were validated against reactor and engine light-off curves. This work has been published as a journal in Industrial and Engineering Chemistry Research [52].

Chapter 4 discusses the development of HC storage and release kinetics over zeolites which are used in DOCs for cold-start HC emissions reduction. A methodology for the development of these kinetics using minimum number of experiments is detailed. Finally, oxidation kinetics developed in chapter 3 and storage-release kinetics developed in this work are integrated in a 1D adiabatic reactor model which accounts for heat transfer, mass transfer and reaction kinetics to predict the performance of a typical DOC under start-up conditions. This work has been submitted for publi-

cation as a journal in Chemical Engineering Science [53].

Finally, chapter 5 discusses the conclusions and provides some recommendations for future work.

CHAPTER II

Global kinetics for a platinum diesel oxidation catalyst with one exhaust hydrocarbon

This chapter discusses the development of global reaction kinetics for C_3H_6 , CO, H_2 , NO and NO_2 under lean conditions over a platinum DOC. C_3H_6 was used to represent all the HCs in the diesel exhaust. A systematic methodology that is applicable for the generation of steady global reaction kinetics in general is detailed. The assumption for the simple HC representation is evaluated.

2.1 Introduction

Differential data under isothermal conditions is ideally suited for global rate generation since it provides direct measurement of the concentrations and temperature at which the measured rates are obtained. With very little knowledge about the form of the rate one can arrive at conclusions for order of the reactants and also the inhibition and enhancement effects due to various species present in the feed stream. Measured rate, which can be calculated from known reactant concentrations, space velocity and conversion, can be plotted against reactant concentrations (log-log scale) to determine the apparent reaction order of a particular species for the corresponding

rate. Temperature for this exercise should be maintained (nearly) constant. Using such plots at different temperature levels one can propose reasonable rate forms, including inhibition terms in typical Langmuir-Hinshelwood forms, and then use the experimental data to calibrate the various constants. However, the necessary experiments to generate such differential data might require extreme space velocities. Also simultaneously non-negligible but differential rates for multiple reactions cannot be handled easily when the rates are too different.

It is a common practice in the literature to use rate forms suggested by Voltz *et al.* [54] and calibrate the rate constants with engine data. This data is either in the form of light-off curves (conversion vs. temperature) or as FTP data measured over the entire cycle of operation. The problem with using light-off curves is that the data useful for kinetic analysis is often confined to a narrow temperature window. The rates obtained in this way will be best, by construction, at nominal inlet concentrations and near the light-off temperature, and they may not be adequate when used to model other reactor operating conditions. On the other hand FTP data contains little kinetic information and, is often in the transport controlled regime.

Voltz *et al.* [54] reported oxidation kinetics for propylene (C_3H_6) and CO for slightly lean exhaust for temperatures between 200°C and 370°C . The experiments for the kinetics study were carried out with simulated gasoline engine exhaust with C_3H_6 as the representative hydrocarbon. A Langmuir-Heinshelwood type rate expression with CO and C_3H_6 inhibition terms was proposed for both CO and C_3H_6 oxidation reactions. Their reaction orders with respect to the corresponding reactants was found to be 1. NO, which is mostly inert under the oxidizing conditions

considered, was found to inhibit the respective reactions. They proposed an empirical term to represent its effect on the rates.

Yu Yao [55] and Morooka *et al.* [56] studied $\text{CO}+\text{O}_2$ and $\text{C}_3\text{H}_6+\text{O}_2$ reactions at 300°C and between $122\text{-}200^\circ\text{C}$ respectively. The reaction rates which were reported in the form of a power law exhibited positive order with respect to O_2 and negative order with respect to C_3H_6 . Yentekakis *et al.* [57] studied $\text{C}_3\text{H}_6+\text{NO}+\text{O}_2$ system and reported that NO had significant inhibition on C_3H_6 oxidation for a Platinum catalyst. Since the feed studied in this work is more complicated ($\text{C}_3\text{H}_6+\text{CO}+\text{NO}+\text{H}_2+\text{O}_2$), a possibility for exhibiting rate forms which are different from usual convention is allowed for the data reported in this work.

Olsson *et al.* [58] and Despreà *et al.* [59] reported microkinetics for NO oxidation on a Pt and Pt-BaO catalysts respectively. The feed stream in either case did not include any reductants such as THC , CO or H_2 . Majewski *et al.* [60] reported that platinum catalysts support NO-NO_2 reaction rather than other reactions involving NO such as $\text{C}_3\text{H}_6+\text{NO}$ or $\text{CO}+\text{NO}$ etc.

This chapter discusses the development of a methodology which can be used for generating global reaction kinetics in general. As a first step towards oxidation kinetics development for DOCs, a simplified system which consists of a catalyst with only Platinum is studied. To further simplify the problem, it is assumed that all the hydrocarbons in the diesel exhaust can be represented by C_3H_6 . While this may seem as an oversimplification, several researchers in the literature routinely make this assumption, and it is hence important to understand and evaluate the assumption in

the case of DOCs. A more complex HC representation is studied in the subsequent chapter III [52].

This work starts by discretizing the entire concentration and temperature domain as seen by a typical DOC. Then a representative but manageable set is selected from the full matrix of the inlet conditions to generate low and medium conversion data using an integral reactor with high space velocity capability. An objective function is developed which critically evaluates the model predictions against experimental observations at all conversions. This objective function is very well suited for global rate generation in general. Model predictions of the exit concentrations for each data point of interest within the objective function are generated with a 1D reactor code which solves the species equations. MATLAB's 'fmincon', a constraint minimization tool is used to minimize the objective function to obtain a set of rate parameters which best describe the experimental results over the entire domain. A modified form of a rate expression which is widely used in the literature is used as a starting point for the optimization process. After we obtain a converged solution from the minimizer at the end of optimization, we successively simplify the overall rate form by adding or removing terms which may significantly affect the objective function. Optimization is done every time we add or remove a term from the rate form. Once the final rate forms and corresponding rate parameters are obtained, they are validated by comparing the model predictions which incorporate these rate forms with light-off curves generated with a full scale DOC reactor used in conjunction with a 1.7L Isuzu diesel engine. The validity of the assumption that C_3H_6 is a representative species for all the HCs present in the diesel exhaust for modeling purposes, is evaluated.

2.2 Experimental

2.2.1 Concentration/Temperature Domain

An important first step in generating useful kinetic rates is to properly define the ranges of concentrations and temperatures for which the resulting rates are intended and to choose the actual test points within this domain that will be used to inform the optimizer of the measured rates. While a domain that is too small does not encompass all intended applications, one that is too large may force global rates to reflect unnecessarily complex behavior not observed in engine applications.

The upper bounds for inlet concentrations of reactants which encompass practical operation were determined. Test conditions for lower concentrations were established by stepping down in factors of three based on work reported by Bissett *et al.* [61]. Since the kinetic rates developed here are intended to be used locally throughout our DOC reactors, it is also important to include the small concentrations expected in the downstream portions of the reactor as well as expected inlet concentrations. The HC and CO concentrations were chosen high enough to describe engine output during PCI combustion, but not so high to describe what could be achieved with post-injection of fuel. For all tests, water concentration was held constant at 8.7%,

HC (C ₃), ppm	CO, ppm	O ₂ , %	NO, ppm	H ₂ , ppm	T, °C
2000	900	13	400	200	200
600	300	4	100	70	255
200	100				325
60	30				415
20					

Table 2.1: Concentration and temperature levels for various species

and CO_2 at 10%. Four temperature levels were chosen based on typical DOC operation. The temperature spacing was equidistant in $1/T$ when the temperature is in K. The various species concentrations and temperature levels are given in table[2.1]. A full factorial covering all 6 variables would result in 640 tests. However such a

$\text{HC} < 3 \cdot \text{CO}$
$\text{HC} > \text{CO}/3$
$\text{H}_2 < \text{CO}$
$\text{H}_2 > \text{CO}/10$

Table 2.2: Concentration constraints for test matrix

full-matrix is not representative of the diesel exhaust in general. For e.g., we do not observe very high levels of HC with very low levels of CO (HC = 2000 ppm and CO = 30 ppm) for the scope of this study. The test matrix generated in this study is specifically aimed to mimic the concentration and temperature domain as seen by a “clean-up” DOC, whose primary purpose is to oxidize the HCs and CO from the exhaust. To achieve this realistic set of DOC conditions, additional constraints, as given in table 2.2, are imposed on the full factorial. Approximately 25 test points (concentration combinations) at each temperature were then randomly selected for testing.

Because NO oxidation rate was greatly suppressed in the presence of other species, separate experiments with the test matrix given in 2.3, were conducted to infer the NO rate. While NO_2 was not in the inlet feed for lower temperatures (200 and 255°C), where the reverse reaction is negligible, it was added to the inlet stream for higher temperature cases (325 and 415°C).

NO, ppm	NO ₂ , ppm	O ₂ , %	T, ppm
450	150	13	200
150	50	5	255
			325
			415

Table 2.3: NO, NO₂ and O₂ concentration levels

2.2.2 Pre-testing Catalyst Preparation

A Pt loading of 7.7 g/ft³ on a γ -Al₂O₃ washcoat was used for all the experiments. The monolith supported catalyst (400 cells/in², wall thickness of .007 in) was hydrothermally aged in a furnace at 650°C for 16 hours. A constant 2.2 L/min flow of 10% H₂O in air was fed to the furnace for the entire 16 hour aging period. For CO chemisorption, the catalyst cores were ground into powder and reduced in H₂ at 300°C for 20 minutes. After cooling the sample to room temperature, CO was pulsed over the samples to determine CO uptake. The data reported for CO chemisorption is based on the average of two measurements. The active site density determined based on this method was 0.080 mol-site/m³, corresponding to a Pt dispersion of 5.7%. For the purpose of the calculation of surface site density, the ratio of CO uptake to the active Pt sites was assumed to be 1.

2.2.3 Reactor Setup

Experiments were carried out in a well insulated vertical stainless steel tubular reactor containing either 1 inch OD for 3/4 inch diameter samples, or 2 inch OD for 1.5 inch diameter samples. Samples were held in place using a compressible ceramic paper wrap that also ensured that reactor flow passed through the catalyst channels. Volumetric space velocities between 50,000 hr⁻¹ and 2,000,000 hr⁻¹ were

achieved by varying the reactor flow rates and catalyst size. Full range of feed concentrations for C_3H_6 , CO, H_2 and NO were achieved by using two concentration levels of BOC certified compressed gas bottles. Heating of the catalyst was achieved by flowing air, N_2 , CO_2 and vaporized water through two inline heaters. Reactor section temperatures were monitored using three Type K thermocouples. The first thermocouple was placed just above the inlet face of the catalyst. The second was placed 3/4 inch below the first. The third could be adjusted axially, to accommodate catalysts of varying length and was placed just after the outlet face of the catalyst. Reactor system pressure was maintained at 1.6 atm to ensure proper flow through the FTIR. A sketch of the experimental set-up is shown in figure 2.1.

2.2.4 Analysis

The reactor inlet and outlet flows were analyzed using a MKS MultiGas 2030 process stream FTIR for CO, CO_2 , NO, NO_2 , N_2O , NH_3 , C_3H_6 , formaldehyde, CH_4 and water. Hydrogen (H_2) was analyzed using a mass spectrometer.

There are a few important details regarding the experiments highlighted below.

- Due to the presence of excess amounts of oxygen as is typical for diesel exhaust, the oxidation reactions were assumed to be more dominant than other side reactions such as water gas shift.
- Monolith samples with thin washcoats (about 20 μm) were used to minimize diffusion resistance within the washcoat.
- Monoliths are known to have excellent but not perfect heat and mass transfer characteristics. Just as in actual applications, when the surface reaction rates are sufficiently fast, such as at higher temperatures, total reaction rate will be

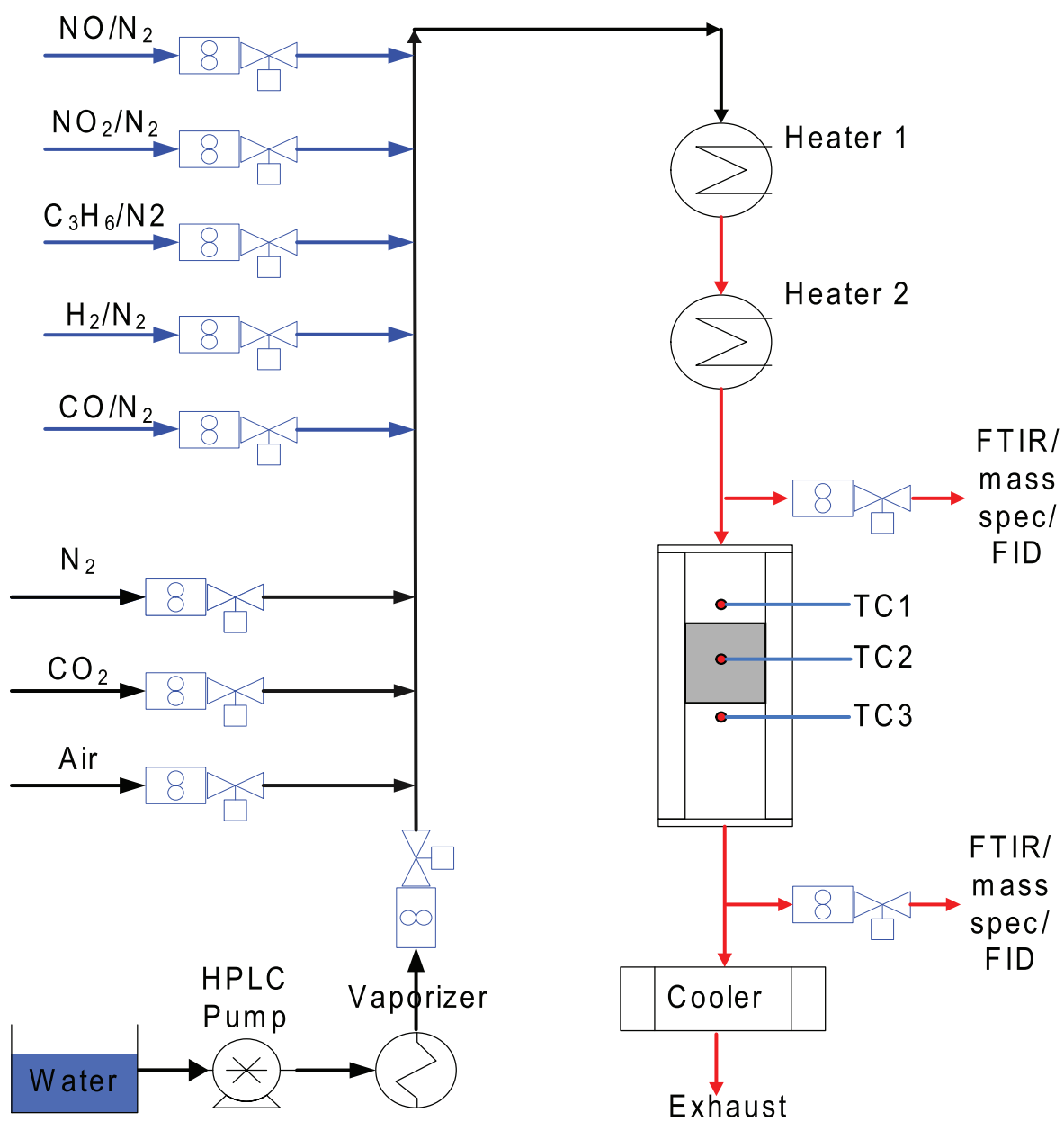


Figure. 2.1: Experimental set-up of the bench scale reactor for DOC kinetics development - Platinum catalyst and C_3H_6 as HC

limited by the rate of transport from the gas to the catalyst surface and so will become insensitive to the surface kinetics. For this reason, kinetics were not even measured in transport limited regimes.

- Individual experiments that essentially produce either complete or no conversion of a particular species are locally insensitive to reaction kinetics and so are of little quantitative value for our methods of kinetics extraction. Therefore, a wide range of space velocities available with the experimental setup was exploited by adjusting the space velocity of each individual experiment to avoid conversion extremes.
- H_2 which was the most reactive species was often the limiting factor. To obtain non-negligible rate of other species, higher H_2 conversions were allowed as a trade-off. All the other species (C_3H_6 , CO and NO) were close to differential at lower temperatures (200°C and 255°C) and showed modest conversions at the higher temperatures (325°C and 415°C) respectively.
- No measurable quantities of N_2O , NH_3 or other hydrocarbons (e.g. CH_4 , aldehyde etc.) were detected during any of the experiments.

2.3 Modeling

The general requirement to generate global kinetics involves solving an outer problem and a corresponding inner problem. The outer problem is the optimization which minimizes an objective function that measures the difference between the measured exit concentration/conversion and the calculated exit concentration/conversion for all the tested conditions. The output from the optimizer is, finally, a set of rate parameters which correspond to the smallest objective function value. The rate

parameters are changed after every iteration to adjust the calculated exit concentration/conversions and thereby improve (lower) the value of the objective function, which is a reflection of how well the calculated provisional reaction rates are in agreement with the experimental measurements. The objective function is calculated based on the solutions from the inner problem which calculates exit concentrations for each of the inlet condition. This inner problem is non-trivial for cases which have non-differential data and species conservation equations were used to solve it.

This section begins by describing the methodology that was developed for the global rate generation process. First, the assumptions made to solve the inner problem (to evaluate the exit for each inlet) are described. Then, the equations used for the same and their scaling are discussed. Thirdly, the need for scaling the parameters outer problem and their scaling is explained. Finally, an objective function is defined for the optimization process and its salient features are detailed.

For the inner problem a simplified 1D reactor code was used which can solve the species equations for a given temperature field. The main assumptions for the simplified 1D model are stated below:

1. Steady state operation
2. Temperature field is prescribed by experimentally measured temperatures. No energy equation is solved.
3. Difference between surface and gas phase temperatures is negligible
4. Transport in transverse direction is modeled using mass transfer coefficient
5. No pore diffusion effects within the washcoat layer

6. Gas species of C₃H₆, CO, H₂, NO and NO₂ are considered trace. Other species - O₂, N₂, H₂O and CO₂ are considered to be in excess. Only the trace species exhibit appreciable change in concentration across the length of the reactor
7. For calculation of bulk properties such as molecular weight and diffusion volume, the bulk gas is the same as N₂

Assumption 3 is justified by the small exotherms obtained from at most moderate conversion of trace species well-distributed over the length of our sample catalyst, and the effective interphase heat transfer in our monolith samples. Regarding assumption 2, reaction exotherms were small to modest by design. Heat loss to the surroundings for small laboratory reactor system like ours can be proportionally large and requires nonstandard modeling compared to full-scale applications. Since the relatively small or negligible axial temperature gradients across the reactor were adequately captured by the three thermocouples, the energy balance equation was not modeled. The three measured temperatures were used to infer the temperature field along the length of the reactor. A second-order polynomial was used to interpolate the three measured temperatures along the length of the reactor to provide the temperatures needed to solve for the trace species. Most of the other assumptions mentioned above are common to aftertreatment reactor modeling and hence their discussion is skipped.

With these assumptions the equations used to solve for the species concentrations can be described by a system of DAEs (differential algebraic equations) shown in equation 2.3.1. The definitions of various terms are detailed in the list of symbols.

$$\frac{w}{A} \frac{dx_{g,i}}{dz} = -k_{m,i} S(x_{g,i} - x_{s,i}) = \sum_{j=1}^{nrct} a_j s_{ij} r_j \quad \text{for } i = 1, \dots, nsp \quad (2.3.1)$$

The boundary condition for equation[2.3.1] is

$$x_{g,i}(0) = x_i^0 \quad (2.3.2)$$

The mass transfer coefficient was calculated based on the asymptotic Sherwood number and the binary diffusivity of individual trace species.

$$k_{m,i} = \frac{Sh}{D_h}(cD_{i,m}) \quad (2.3.3)$$

The binary diffusion coefficients for each trace species in the gas mixture was taken as though the mixture were nitrogen. The correlation given by Fuller *et al.* [62] for the calculation of the binary diffusion coefficient is shown in equation 2.3.4.

$$cD_{i,m} = \frac{3.85 \times 10^{-5} T^{0.75} \sqrt{\frac{1}{M_i} + \frac{1}{M_{N_2}}}}{[\Sigma_i^{1/3} + \Sigma_{N_2}^{1/3}]^2} \quad (2.3.4)$$

2.3.1 Scaling of Species Equations

Scaling of equations is necessary to make the system more robust to solve for a wide variety of combinations of inlet conditions and rate constants. To this end let \hat{a} represent the scaled version of variable a . The scaling of the variables which go into the species equations are presented in equations [2.3.5-2.3.12].

$$z = L\hat{z} \quad (2.3.5)$$

$$T = T_r\hat{T} \quad (2.3.6)$$

$$x_{g,i} = x_{r,i}\hat{x}_{g,i} \quad (2.3.7)$$

$$x_{s,i} = x_{r,i}\hat{x}_{s,i} \quad (2.3.8)$$

$$w = w_r\hat{w} \quad (2.3.9)$$

$$\hat{k}_{m,i}(\hat{T}) = \frac{SV}{w_r}k_{m,i}(T) \quad (2.3.10)$$

$$\hat{s}_{ij} = \frac{s_{ij}}{x_{r,i}} \quad (2.3.11)$$

$$\hat{r}_j(\hat{z}, \hat{T}, \vec{\hat{x}}_s, p) = \frac{V}{w_r}a_j(z)r_j(T, \vec{c}_s), \quad \text{where } c_{s,i} = c * x_{s,i} \text{ and } c = \frac{p}{RT} \quad (2.3.12)$$

The transformation to scaled variables requires the introduction of reference values, T_r , $x_{r,i}$, and w_r , for the temperature, mole fractions, and molar flow rates, respectively. These reference values only need to be roughly specified, just capturing their orders of magnitude for the scaling to be effective. Finally the dimensionless form of equation 2.3.1 is given as

$$\hat{w} \frac{d\hat{x}_{g,i}}{d\hat{z}} = -\hat{k}_{m,i}(\hat{x}_{g,i} - \hat{x}_{s,i}) = \sum_{j=1}^{nrct} \hat{s}_{ij} \hat{r}_j \quad \text{for } i = 1, \dots, nsp \quad (2.3.13)$$

The equations are solved using MATLAB's DAE solver - 'ode15s'. The solver was modified to account for concentration jumps by changing the error test to be a function of only the gas phase concentrations of the trace species. The perturbations for the jacobian calculations were increased from 10^{-8} to 10^{-5} . Other minor modifications were done to increase the performance of the DAE solver.

2.3.2 Scaling Optimization Parameters

For the optimization process MATLAB's constrained minimizer, called 'fmincon', was used. Although there is internal scaling for the optimization parameters within fmincon, the variables can be better scaled with the problem specific information available than any generic choices in the optimizer. Note that the pre-exponentials and activation energies can be scattered anywhere in the real space and that the optimizer would have extreme difficulty trying to obtain a minima without proper scaling (Pre-exponentials can be $\sim 10^{-10}$ while the activation energy can be $\sim 10^4$).

Activation energies always occur in the form $e^{-E/RT}$, so the proper dimensionless activation energy to give the proper scaling near $T = T_r$ is

$$\hat{E} = \frac{E}{RT_r}. \quad (2.3.14)$$

Whenever Arrhenius forms appear, we can then consider the exponential portion to be, in dimensionless scaled form,

$$e^{-E/RT} = e^{-\widehat{E}/\widehat{T}}. \quad (2.3.15)$$

The magnitude of this factor, near $T = T_r$, where $\widehat{T} = O(1)$, should then be estimated as $e^{-\widehat{E}}$.

When the forms of global rate expressions are of a Langmuir-Hinshelwood type, the constants in the denominator are often referred to as adsorption constants. Although our exercise was to generate global kinetics directly, we loosely refer to the Arrhenius constants in the denominator of a rate expressions as adsorption constants. The individual terms containing the adsorption constants in the inhibition terms, such as those that appear in the denominator of the rate expression, equation 2.4.3, should be roughly $O(1)$ if it is meaningful to write these terms as $(1 + K_i c_{s,i} + \dots)$. The term K_i is the adsorption constant with Arrhenius temperature dependency ($Aa_i e^{-Ea_i/RT}$) and $c_{s,i}$ is the concentration at the corresponding partial pressure and temperature. Now, estimating the exponential as above, the desired dimensionless pre-exponential is given as,

$$\widehat{Aa}_i = Aa_i e^{-\widehat{E}a_i} c_r x_{r,i}, \quad \text{where } c_r = c(T_r) = \frac{p}{RT_r}, \quad (2.3.16)$$

and $x_{r,i}$ is some reference mole-fraction for species i . In summary, each individual inhibition can be considered to be transformed to,

$$K_i c_{s,i} = \widehat{Aa}_i e^{\widehat{E}a_i(1-1/\widehat{T})} \widehat{x}_{s,i}. \quad (2.3.17)$$

With this scaling method, \widehat{Aa}_i and $\widehat{E}a_i$ can be reasonably expected to be $O(1)$ and properly scaled for input to the optimizer.

To scale the pre-exponentials in $k_i = A_i e^{-E_i/RT}$, the rate constants for the overall global rates as in equation 2.4.3, we need an estimate of the corresponding rate. When equation 2.3.13 is properly scaled, it should be such that $\sum \hat{s}_{ij} \hat{r}_j$ is $O(1)$. Each of the non-zero \hat{s}_{ij} is expected to be somewhat large because each contains a large factor of $1/x_{r,i}$. Therefore, each of the \hat{r}_j are somewhat smaller than normal, but we are not too far off for this purpose to assume that $\hat{r}_j = O(1)$. Then, proceeding as above and assuming the total inhibition, $G = O(1)$, the desired scaled pre-exponential is given as,

$$\widehat{A}_i = \frac{V a_j}{w_r} A_i e^{-\widehat{E}_i} c_r^2 x_{r,i} x_{s,O_2}, \quad (2.3.18)$$

where a_j is the site-density and x_{s,O_2} is the typical excess O_2 mole fraction.

2.3.3 Definition of Objective Function

As mentioned earlier, the objective functions should represent the disparity between calculated and measured conversion/exit concentration and help the optimizer to make a decision on which direction to move to minimize this difference. For these kinds of exercises generally an Euclidean norm based on model vs. experiments is used. Because the concentration domain covers several order of magnitude, a logarithm of the ratio between model vs. experiments was chosen. Necessarily then, these terms are already scaled in a relative sense, so that relative errors of small concentrations enter into the objective function with the same implied weight as relative errors in large concentrations.

While for C_3H_6 , CO and NO exhibited conversions less than 60%, H_2 due to its higher reactivity showed conversions $\sim 90\%$ for some cases. These high conversions were less than the transport limited solution and hence non-trivial kinetic informa-

tion was contained in this data.

Figures 2.2 and 2.3 are parity plots showing the comparison between model pre-

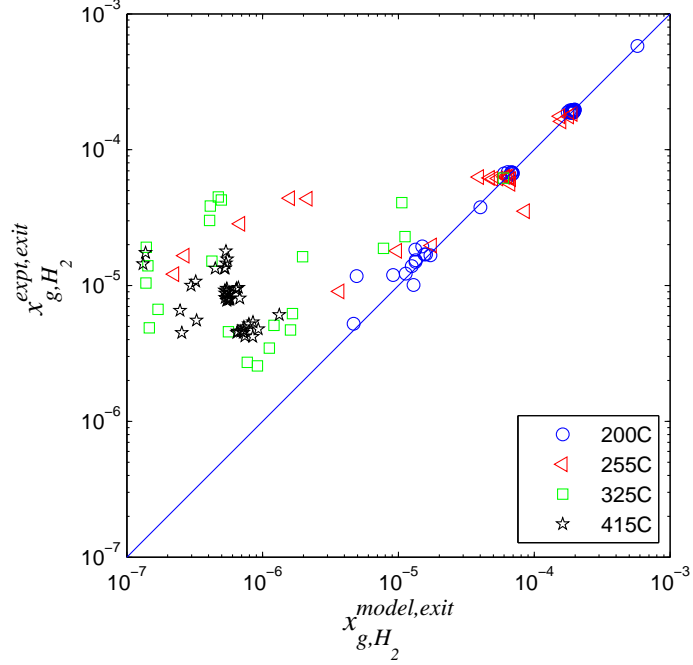


Figure. 2.2: x_g comparison between model and experiment

dictions and experiments for H_2 for a typical solution (set of A_i and E_i) generated in the optimization process. Both figure 1 and 2 represent the same data but plotted in different fashions. While figure 1 shows H_2 exit concentration (x_g) comparison, figure 2 shows the H_2 comparison between $x_g^{in} - x_g^{out}$ ($\Delta x_g = \text{conversion} * x_g^{in}$). While the x_g comparison is critical of data at higher conversion (which in our case were at higher temperatures), the Δx_g comparison is more critical of data at lower conversions (which in our case were at lower temperatures). Thus while x_g comparison cannot meaningfully distinguish between 0-5% conversions, Δx_g comparison cannot meaningfully distinguish between 100 and 95% conversions which have small exit concentrations. We hence define a norm which uses x_g comparison for all data above

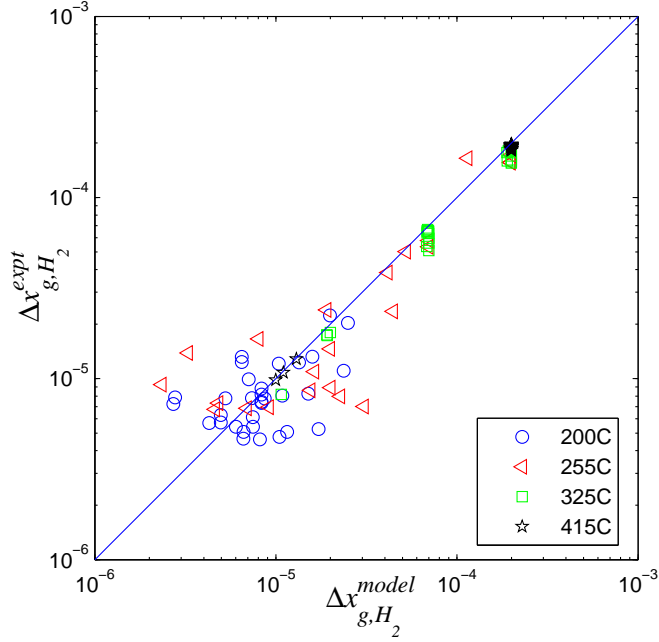


Figure. 2.3: Δx_g comparison between model and experiment

50% conversion and Δx_g comparison for the data below 50% conversion. The 50% barrier is picked for simplicity since either choice works equally well for moderate conversions.

This norm is suitably scaled by the number of species being considered in any particular optimization ($n_{sp'}$), the number of temperatures being considered (n_T), and the number of points at each temperature, n_j , such that each data point contributes equally at each temperature, and each temperature and species contributes equally to the overall norm calculation. The norm definition is given in equation 2.3.19, where the sum of the two log terms is interpreted as taking one term or the other depending on the conversion for that species.

$$\text{norm}^2 = \frac{1}{n_{sp'}} \sum_{i=1}^{n_{sp'}} \frac{1}{n_T} \sum_{j=1}^{n_T} \frac{1}{n_j} \sum_{k=1}^{n_j} \left[\log^2 \left[\frac{\Delta x_{g,i}^m}{\Delta x_{g,i}^e} \right]_{\text{conv} \leq 50\%} + \log^2 \left[\frac{x_{g,i}^m}{x_{g,i}^e} \right]_{\text{conv} > 50\%} \right] \quad (2.3.19)$$

It should be noted that the data points likely to be strongly influenced by mass

transport effects (for example, high temperatures) would be expected to contribute little to the norm since we have good confidence in the model’s ability to describe transport behavior. The errors in our measurements were incorporated in the norm by removing from the summation any test points for which $\Delta x_{g,i}^e$ or $x_{g,i}^e$ was less than 5 ppm (3 ppm for H₂). This was based on the accuracy of our FTIR/mass spectrometer measurements.

2.4 Results and Discussion

2.4.1 C₃H₆, CO and H₂ Oxidation

As described earlier, the general procedure for generation of global rates includes first assuming particular forms for the relevant rates and then optimizing for the rate parameters to best fit the experimental data. The evaluation of how well the rate form represents the data is based on the norm or the objective function which is obtained at the end of the optimization. For the scope of this work, conventional Langmuir-Hinshelwood rate forms that have been used for similar purposes in the literature were used as a starting point. Inhibition/enhancement terms were successively added or removed to check if there was significant improvement in the norm value. Adjusting the degrees of freedom available to the optimizer in this additive fashion would always result in improved fits with more terms, hence subjective judgement was exercised in determining “significant” improvements based on inspection of the corresponding parity plots. A premium was also placed on simplicity of the rate forms and on precedents in the literature.

As discussed in the introduction section, the oxidation rates for C₃H₆ and CO

from Voltz *et al.*, as written in Oh *et al.* [63], are widely used throughout the literature for inferring these rates. Oh *et al.* also assumed that the H₂ rate is similar to that of CO. The rate form as given in Oh *et al.* is

$$r_i = \frac{\bar{k}_i x_{s,i} x_{s,O_2}}{G_1} \quad \left[\frac{\text{mol}}{\text{cm}^2_{Pt} \cdot \text{s}} \right], \quad (2.4.1)$$

where

$$G_1 = T(1 + \bar{K}_{CO} x_{s,CO} + \bar{K}_{C_3H_6} x_{s,C_3H_6})^2 (1 + \bar{K}_{CO \cdot C_3H_6} x_{s,CO}^2 x_{s,C_3H_6}^2) (1 + \bar{K}_{NO} x_{s,NO}^{0.7}). \quad (2.4.2)$$

Although this exercise does not involve generating microkinetics, the constants in the denominator of the Langmuir-Hinshelwood rate forms used here will be referred to as adsorption constants. All rate and adsorption constants have Arrhenius form, $A * e^{-E/RT}$. A modified version of this rate expression was used as a starting point.

First, the rates were converted to be functions of molar concentrations per unit volume (mol/m³) instead of mole-fractions. When obtaining rates from elementary steps one naturally arrives at global rates in terms of concentrations and not mole-fractions. The pressure effect is then automatically absorbed in the rates, and they can be expected to apply at any pressure, in particular, at the elevated 1.6 atm at which reactor experiments were conducted. This was done by multiplying and dividing the mole fractions with $c = p/RT$, the molar concentration. Half of these c 's are absorbed into $c_{s,i} = c * x_{s,i}$. The other half, along with the temperature, T , in the inhibition term of equation 2.4.1 are absorbed into the new rate constants below. To do this, p (at the 1 atm of Voltz) and R are constants, so that the new approximate rate constants below are formally Arrhenius forms multiplied by various factors of T . These approximate rate constants were forced into pure Arrhenius form by replotting

at a few representative temperatures and refitting.

Next the second term in the inhibition was removed. Voltz *et al.* [54] stated that this term was included for empirical reasons only, so this term was disregarded initially to minimize the degrees of freedom. Finally, the exponent on the concentration of NO in the inhibition term was set to unity. Although this term is empirical, it was initially retained here to capture the effect of NO on the rates (if any). However, if the exponent of the NO concentration is less than 1, the resulting rate is not differentiable at zero, making the rate infinitely sensitive to the concentration of NO as the NO concentration approaches zero ($dr_i/d[NO] \rightarrow \infty @ [NO] = 0$). While NO is relatively inert compared to the oxidation of CO and C₃H₆, as in the case Voltz considered, there are regimes of interest for DOC operation where depletion of NO is possible. The rate forms which we used as a starting point for our optimizations are therefore given by equation 2.4.3.

$$r_i = \frac{k_i c_{s,i} c_{s,O_2}}{G_2} \left[\frac{\text{mol}}{\text{mol-site} \cdot \text{s}} \right], \quad (2.4.3)$$

where

$$G_2 = (1 + K_{C_3H_6} c_{s,C_3H_6} + K_{CO} c_{s,CO})^2 (1 + K_{NO} c_{s,NO}). \quad (2.4.4)$$

Initial Guess for Optimization

Global optimization methods generally have the advantage of being less sensitive to the choice of initial guess compared to local optimization methods. For the approach described in this work, a careful, controlled, incremental improvement of the rates was preferred. So the optimization was restricted to local methods while accepting more stringent demands for good initial guess. Working from the modified rate constants inferred from Oh *et al.* was not generally effective, at least partially

because the concentration regime of interest for this work is substantially different from that in Oh *et al.*. Hence an alternative approach was developed to generate initial guess as described below.

The division of the temperature regime into discrete bins aids the process of generating a proper initial guess. For generating rate and adsorption constants for C₃H₆, CO and H₂, NO was assumed to linearly vary between inlet and exit. Since in most of the cases there was very little NO conversion, the linear approximation for NO is well justified. The optimization is performed on individual k_i and K_i (rate and adsorption constants) for the rate forms given in equation 2.4.3 at a fixed temperature. Since the scaling ensures that the variables (scaled k_i and K_i) are $O(1)$, any number which is $O(1)$ is suitable as a starting guess. The results from the optimization at individual temperatures are plotted in an Arrhenius plot ($\log k_i$ vs $1/T$) to generate proper initial guesses for all pre-exponentials and activation energies. A typical Arrhenius plot generated for the initial guess of the rate constant for C₃H₆ is shown in figure 2.4.

2.4.2 NO Oxidation

The oxidative environment promotes the NO oxidation reaction rather than the NO reduction reactions which occur over three-way catalysts (CO+NO or C₃H₆+NO etc.). The measurements commonly indicated that the net NO oxidation reaction is greatly suppressed in the presence of reductants in the stream. Hence separate experiments were conducted to infer the NO \rightleftharpoons NO₂ rate with only NO, NO₂ and O₂ present in the feed. Note that this reaction is reversible and is limited by equilibrium. All the data obtained from these sets of experiments gave differential conversions.

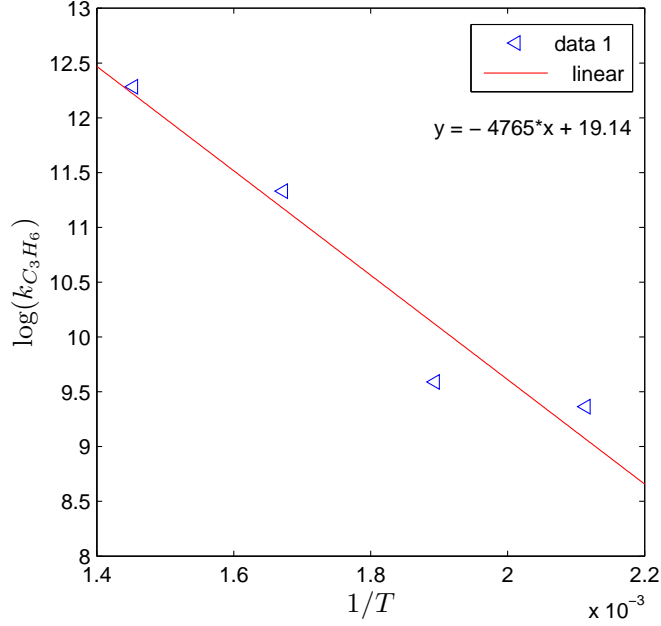


Figure. 2.4: Initial guess for $A_{C_3H_6}$ and $E_{C_3H_6}$ from optimization at individual temperatures

Initially, using only the data which contained NO and O₂ at the inlet was used to infer the forward rate. Simple log-log plots of NO oxidation rate vs. concentration at individual temperatures indicated that a simple power law formulation was not adequate but that a Langmuir-Hinshelwood rate form involving NO inhibition effects was well suited. The oxygen dependence on the rate remained nearly constant for this exercise. The choice for stoichiometric coefficients for the reactant concentrations in the rate was based on the power law results from individual temperatures and the simplest, commonly-used algebraic form that ensures a vanishing global rate at equilibrium. From these observations the following rate form was proposed for NO oxidation.

$$r_{NO} = \frac{k_{NO}c_{s,NO}\sqrt{c_{s,O_2}}}{(1 + K_{NO}c_{s,NO})} \left[1 - \frac{c_{s,NO_2}}{K_{eq}c_{s,NO}} \sqrt{\frac{c_R}{c_{s,O_2}}} \right] \quad (2.4.5)$$

This form is physically reasonable and it vanishes at equilibrium. Also, the ap-

parent reaction orders in the numerator respect the stoichiometric coefficients of the reaction and the term in the denominator appropriately captures the self inhibition of NO that we observed in the preliminary analysis. c_R is the concentration at the reference pressure of 1 atm. K_{eq} is the equilibrium constant, based on the free energy of the NO oxidation reaction.

$$K_{eq} = 1.5 \times 10^{-4} e^{6864/T} \quad (2.4.6)$$

k_{NO} and K_{NO} represent the rate constant and adsorption constants respectively with Arrhenius forms of temperature dependency.

The rate expression given in equation 2.4.5 was optimized using the data obtained with feeds containing NO, NO₂ and O₂. A parity plot obtained with the optimized parameters appears in figure 2.5. Note that only Δx_g ($x_g^{in} - x_g^{out}$) is plotted when comparing experimentally measured values with model predictions using optimized

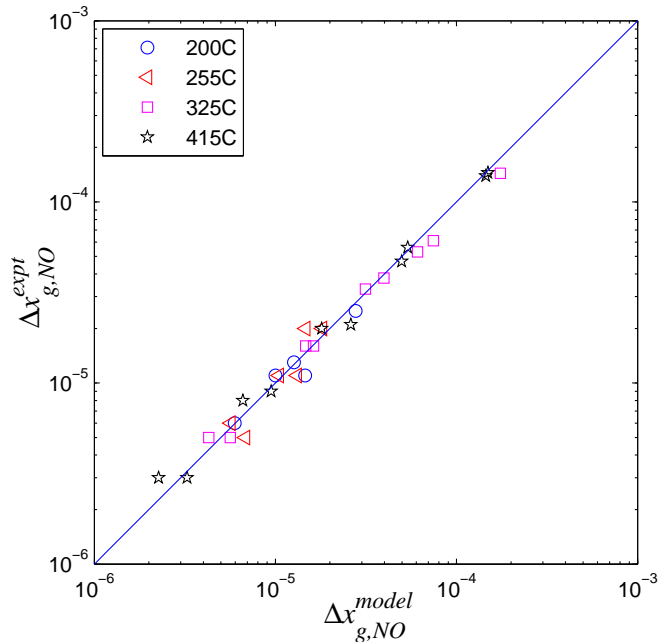


Figure. 2.5: Comparison of Δx_{NO} between model and experiment for cases which has only NO, NO₂ and O₂ in feed-stream (no reductant)

parameters, because all the data generated for $\text{NO}+\text{NO}_2+\text{O}_2$ in the stream had conversions less than 50%. We conclude that this model captures the experimental data well over the entire concentration and temperature regimes. It is however important to check if this rate expression predicts small NO conversions in the presence of reductants in the stream, since no significant net NO oxidation is observed in the presence of reductants. To evaluate this we plot in figure 2.6 the experimental Δx_{NO} against model Δx_{NO} for the cases in the original test matrix which contained C_3H_6 , CO and H_2 (reductants) along with NO in the stream.

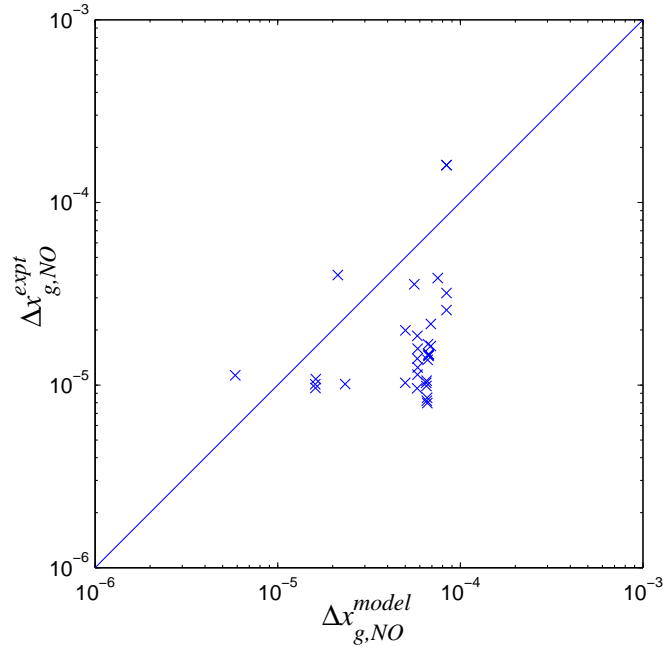


Figure. 2.6: Comparison of Δx_{NO} between model and experiment (all temperatures) in the presence of reductants in the feed-stream using the rate form of equation 2.4.5.

Clearly the model over-predicts the NO conversions by an order of magnitude in comparison to the experimental data when reductants are present in the feed. The rate expression hence needs to be modified when being used for these cases. We take advantage of not just the similarity in the NO inhibition terms between equations 2.4.4 and 2.4.5, but also their equality when reductants are absent ($c_{s,\text{C}_3\text{H}_6} = c_{s,\text{CO}} =$

0), to generalize equation 2.4.5 to equation 2.4.7, which can be used when reductant is also present.

$$r_{NO} = \frac{k_{NO} c_{s,NO} \sqrt{c_{s,O_2}}}{G_2} \left[1 - \frac{c_{s,NO_2}}{K_{eq} c_{s,NO}} \sqrt{\frac{c_R}{c_{s,O_2}}} \right], \quad (2.4.7)$$

Here G_2 is given by equation 2.4.4. Final optimization of the rate constant k_{NO} in this last form is performed when the optimization of the full problem is considered in the next section.

2.4.3 Optimization of the Full Problem

With the rate forms (equations 2.4.3 and 2.4.7) and initial guesses known, all the reactions (C_3H_6 , CO, H_2 , NO and NO_2) are optimized for the entire concentration and temperature domains. The objective function (norm) value at the end of the optimization was **0.4870**. The next step is to systematically add or remove terms accounting for inhibition/enhancement to see if any improvement is obtained in the norm value.

For the first pass terms from the inhibition are removed one at a time, namely $K_{CO} c_{s,CO}$, $K_{C_3H_6} c_{s,C_3H_6}$ or $K_{NO} c_{s,NO}$, to estimate which term, when removed and a subsequent re-optimization of A 's and E 's is performed, results in a solution with the least perturbation to the norm. Table 2.4 gives the values of the norm when each of the inhibition terms for C_3H_6 , CO and NO were removed individually.

Term removed	Final norm value
$K_{CO} c_{s,CO}$	0.9345
$K_{C_3H_6} c_{s,C_3H_6}$	0.4873
$K_{NO} c_{s,NO}$	0.6932

Table 2.4: Final norm values after various terms in the inhibition terms were removed

These values show that the removal of the C_3H_6 term from the denominator resulted in the smallest perturbation in the norm, and that the perturbation is small enough to justify removal of this term in the denominator. That is, the gain in the simplicity of the rate form was judged to outweigh the nearly imperceptible loss in ability to represent data. Removal of any terms in addition to C_3H_6 , namely CO or NO, is pointless since the values in table 2.4 demonstrate that in either case the re-optimized norm was significantly increased even with one more degree of freedom (presence of C_3H_6).

H_2 was present in the feed stream, and hence a possible enhancement effect of H_2 on the other rates was also studied. A term, $(1 + K_{H_2}c_{s,H_2})$, was included in the numerator of all the rates to represent any H_2 enhancement. Re-running the optimization gave a very marginal improvement in the overall norm value. The final norm value with the inclusion of the H_2 enhancement term was **0.4868**. Since this was not a substantial improvement in the norm value we concluded that the H_2 effect is not worth including in the rate expressions.

The absence of the terms for HC inhibition or H_2 enhancement should not be interpreted as denying the existence of these effects. Detailed experiments designed specifically to elucidate these details for these individual reactions could very likely reveal these commonly-observed effects. Rather, we claim that these effects are not large enough to require representation within this global reaction scheme to describe rates over several orders of magnitude in concentration and wide temperature regime, especially when it is desired to keep the total degrees of freedom represented by the kinetic parameters small. While these results are designed to capture the overall

trends quantitatively, the parity plots below show the predictions for some of the individual cases can still contain substantial errors that could mask additional chemical effects.

The final rate forms that were used for the kinetic parameter optimization are given by equations 2.4.8 and 2.4.9.

$$r_i = \frac{k_i c_{s,i} c_{s,O_2}}{G} \quad i=\text{CO, C}_3\text{H}_6 \text{ or H}_2 \quad \left[\frac{\text{mol}}{(\text{mol-site}) \cdot \text{s}} \right] \quad (2.4.8)$$

$$r_{NO} = \frac{k_{NO} c_{s,NO} \sqrt{c_{s,O_2}}}{G} \left[1 - \frac{c_{s,NO_2}}{K_{eq} c_{s,NO}} \sqrt{\frac{c_R}{c_{s,O_2}}} \right] \quad \left[\frac{\text{mol}}{(\text{mol-site}) \cdot \text{s}} \right] \quad (2.4.9)$$

where

$$G = (1 + K_{CO} c_{s,CO})^2 (1 + K_{NO} c_{s,NO}), \quad (2.4.10)$$

$$k_i = A_i * e^{-E_i/RT}, \quad (2.4.11)$$

and

$$K_i = A_{a_i} * e^{-E_{a_i}/RT}. \quad (2.4.12)$$

The rate constants for these reaction rates are given in table 2.5.

Figures 2.7, 2.8, 2.9 and 2.10 show the parity plots comparing the model predictions versus the experimental observations for C₃H₆, CO, H₂ and NO (NO₂) for all the operating points. All points with conversions less than 50% (experimental conversion) are plotted in a Δx_g ($x_g^{in} - x_g^{out}$) plot and all points with conversions greater than 50% (experimental conversion) are plotted in a x_g (x_g^{out}) plot (exit concentrations) for the reasons discussed in the objective function definition section. Note that the proposed rate forms capture the experimental behavior over several orders of magnitude of concentrations and a wide temperature range.

Rate constants	Value
A_{HC}	1.123×10^9
E_{HC}	5.156×10^4
A_{CO}	3.725×10^6
E_{CO}	2.213×10^4
A_{H_2}	1.335×10^7
E_{H_2}	3.032×10^4
A_{NO}	1.086×10^3
Aa_{CO}	10.57
Ea_{CO}	-9.709×10^3
Aa_{NO}	32.19
Ea_{NO}	-1.901×10^4

Table 2.5: Rate constants as a result of the final optimization of the full problem

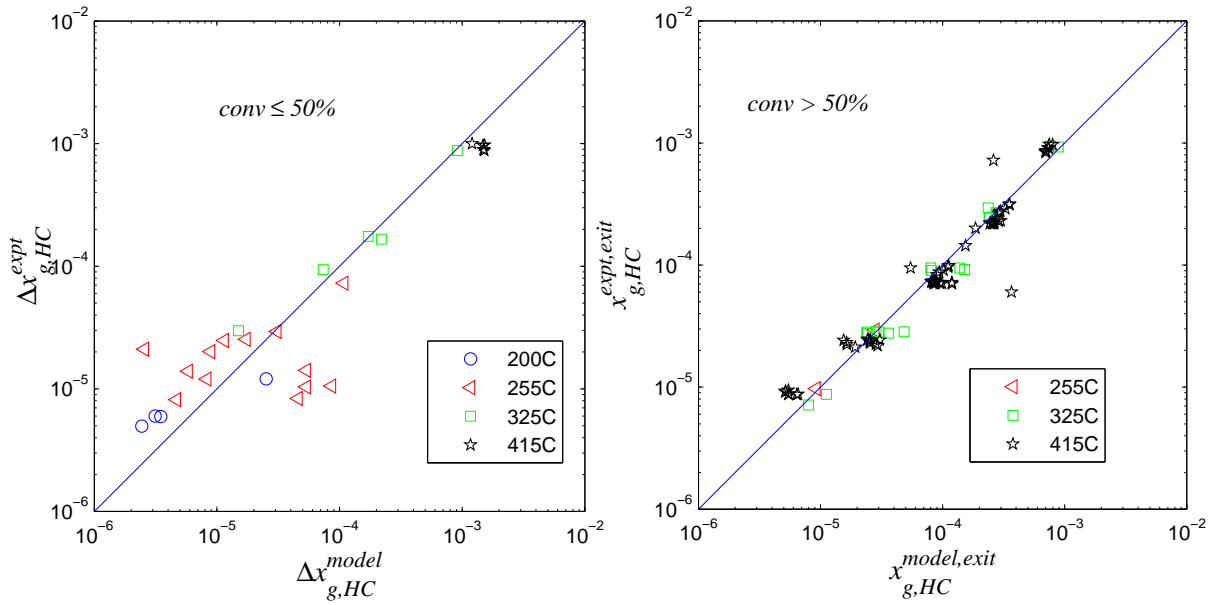


Figure. 2.7: Comparison between experiment and model predictions - Δx_g and x_g^{exit} for C_3H_6

The clustering of points in the x_g plot for C_3H_6 is mainly because some of the experimental conversions at this end were very close to being transport limited (very fast reaction rate), so the outlet concentrations depend primarily on inlet C_3H_6 concentration and space velocity, which themselves cluster at discrete values. In these

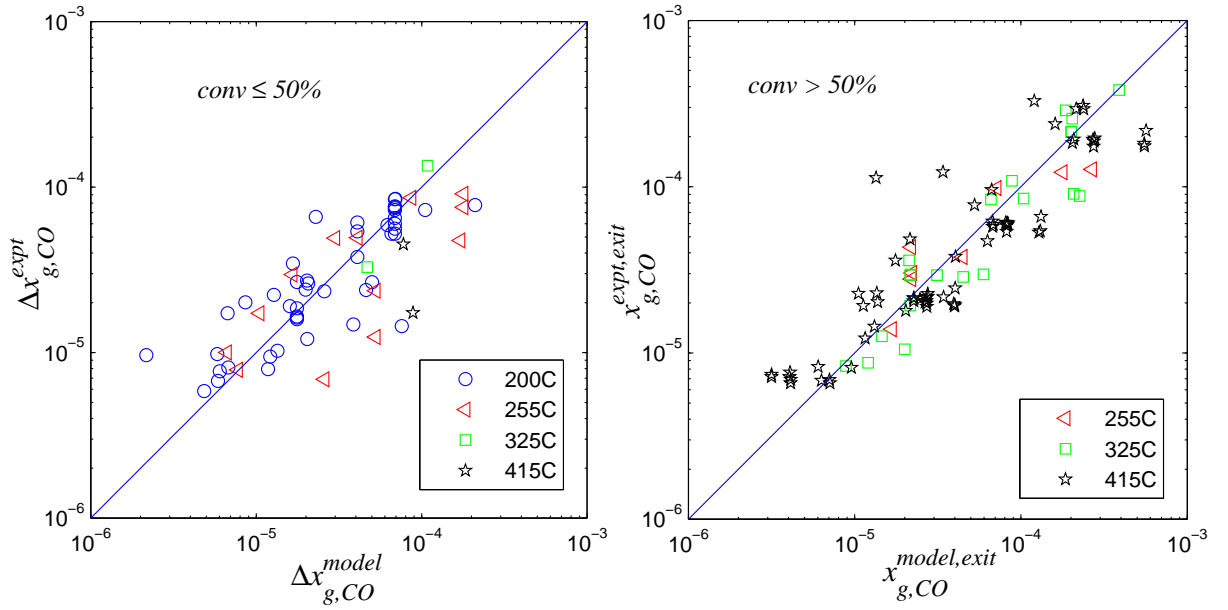


Figure. 2.8: Comparison between experiment and model predictions - Δx_g and x_g^{exit} for CO

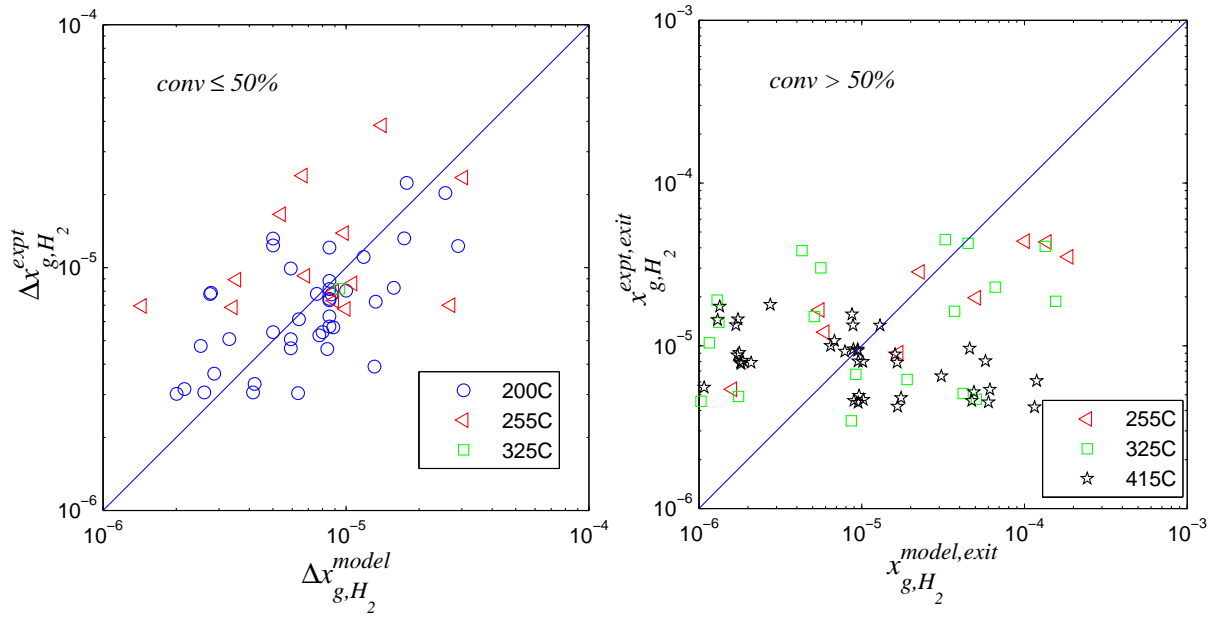


Figure. 2.9: Comparison between experiment and model predictions - Δx_g and x_g^{exit} for H₂

cases we would want the model to predict a transport limited solution as it rightly does. The H₂ plots (figure 2.9) show that the kinetic model does a better job at low

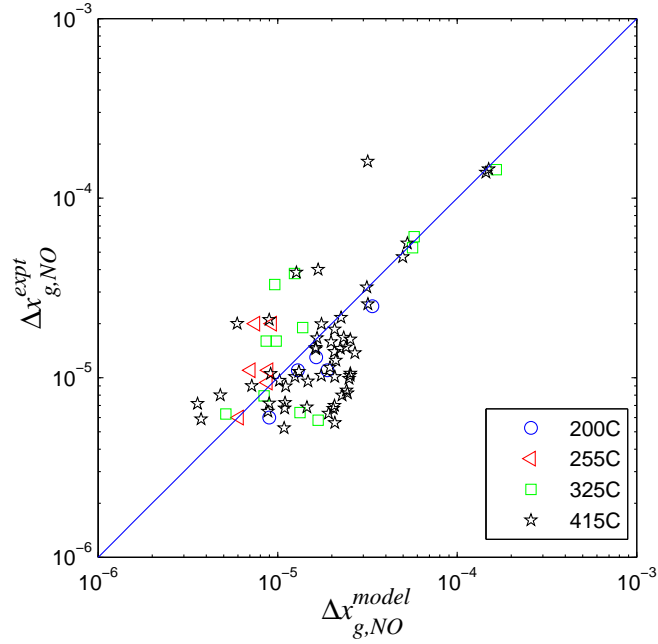


Figure. 2.10: Comparison of Δx_g for NO between experiment and model predictions - Feeds with and without reductant

temperatures than at higher temperatures. Most of these measured H_2 conversions are close to the transport limited solution and have very high conversions ($\geq 90\%$), leaving only a few ppm (≤ 10 ppm) at the exit of the reactor. (Also the maximum H_2 inlet concentration was 200 ppm implying that for such high conversions we would only have a few tens of ppm left in the stream.) This makes the plot look poor even if the kinetic model predicts only slightly higher or lower than the measured value.

The final optimization step produced zero NO activation energy for its rate constant. This was because we forced the same NO inhibition terms in equation 2.4.3 and 2.4.7. For this simplification, namely having the same inhibition term for all the rate expressions, we sacrificed 2 degrees of freedom and the resulting goodness-of-fit compared to fitting relevant data separately with independent inhibition terms. The results in figure 2.10 obtained with this simplification were still satisfactory,

however, because the resulting NO adsorption constant, K_{NO} , necessarily changed from its value obtained without reductants (figure 2.5), and the rate constant for NO oxidation, k_{NO} , compensated as much as possible which, in this case, produced zero activation energy for this rate constant, a lower limit that was imposed upon the optimizer.

2.4.4 Engine Validation

Light-off curves were generated for total hydrocarbons (THC) and CO using an engine-dynamometer system with a full scale DOC with the same formulation (Pt catalyst) mounted in the exhaust stream. The engine is a 1.7 liter Isuzu diesel engine. The details of the engine set-up can be found in Knafl *et al.* [64]. The light-off curves used for validation here correspond to the M2 condition described in [64]. Due to the lack of reliable NO_x and H_2 measurements with the engine only the CO and THC validations are reported in this work. Rate expressions developed in this were used to simulate the light-off curves generated by the engine. All the points on the light-off curves are generated by conventional combustion modes in the cylinder (no PCI combustion). The comparison of model predicted versus experimentally measured hydrocarbon conversions is plotted in figure 2.11, and the similar comparison between CO conversions is plotted in figure 2.12. The surface site-density (a_j) was adjusted to match the 50% conversion for the THC when comparing against engine curves. This was because the DOC mounted on the engine was aged differently than the sample used for the reactor studies. A series of degreening tests were conducted on the engine mounted DOC before the light-off data was taken.

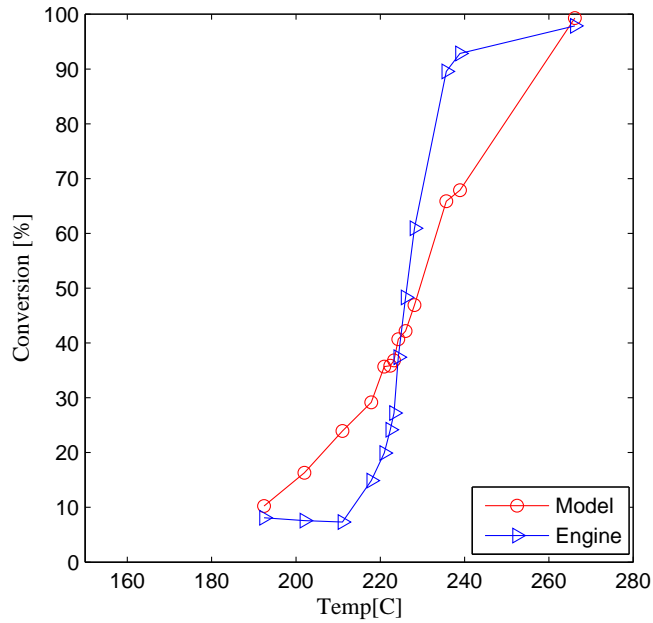


Figure. 2.11: THC validation with engine generated light-off curves

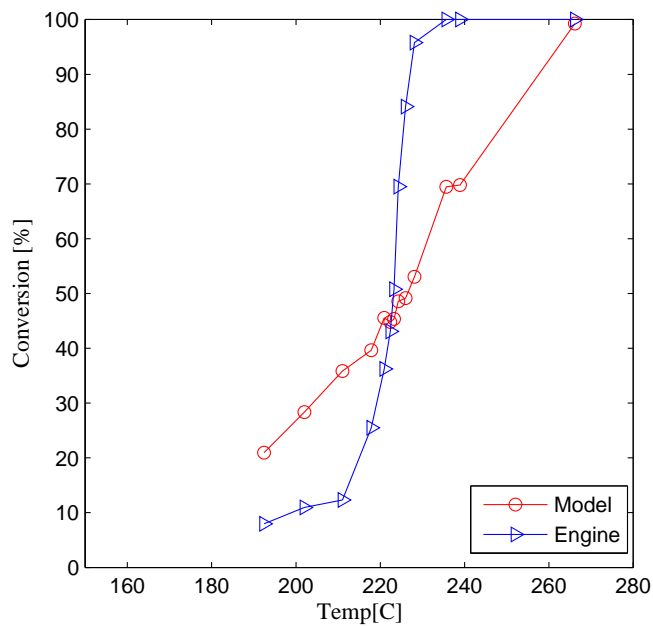


Figure. 2.12: CO validation with engine generated light-off curves

There are several reasons behind the disagreement of the light-off curves over the entire range of temperatures for total hydrocarbons (THC) and CO.

- In the engine exhaust, only the gas-phase temperatures upstream and downstream of the DOC were measured. As in the kinetic analysis, these two tem-

peratures were used to generate a linear interpolant for the temperatures inside the DOC for modeling purposes. Since this procedure ignores any potential local sharp temperature rise produced by the rapid exotherms within the reactor, the temperature sensitivity of reactor response to light-off conditions could be underestimated.

- The assumption that C_3H_6 represents the THC of the entire diesel exhaust is a very crude one. Diesel exhaust, based on this work, should be split into at least two categories: one that consists of heavier hydrocarbons (e.g., unburned fuel components) and the other partially oxidized lighter hydrocarbons which (e.g., combustion products).
- Since the NO concentrations and conversions were not entirely reliable, and since all the rates are a function of NO through the inhibition, the rates would not be able to capture the experimental behavior fully.
- Finally the aging procedure followed for the catalyst used in the reactor (16 hour hydrothermal aging) was different from that followed for the catalyst used with the engine tests (using engine exhaust as reported in Knafel *et al.* [64]).

Conclusions

Global oxidation reaction rates for C_3H_6 , CO, H_2 and NO in the presence of excess O_2 were developed over wide temperature and concentration ranges. A common inhibition term, containing only factors for CO and NO for all the rates, was found to satisfactorily represent our data. An attempt to simply and directly capture potential enhancement due to H_2 in our rate expressions showed that this effect did not significantly affect this representation. The following necessary machinery for global

reaction rate generation was used: careful choice of temperature and concentration domain, random sampling of data for reactor measurements, a reactor capable of high space velocities, optimization routines, reactor codes, and finally an optimization methodology to generate proper initial guesses and successively improve the rate form. An objective function which critically evaluates all model vs. experiment comparisons is defined. All the rates gave reasonable agreement with the laboratory experimental data. Attempts to validate the kinetic model against the results of engine tests with a full-size DOC show that the measured CO and THC conversions increase more rapidly with temperature during catalyst light-off. Further work would be required to clarify the origins of this discrepancy.

CHAPTER III

Global kinetics for a commercial diesel oxidation catalyst with two exhaust hydrocarbons

This chapter continues the discussion on the global oxidation reaction kinetics for the various species over a DOC. Understanding the need for a more complex HC representation, the HCs in the diesel exhaust are represented by two HC species. A commercial DOC catalyst with more realistic catalyst formulation was used for the study reported in this chapter. Reaction kinetics were generated by utilizing the methodologies developed in the previous chapter. Model predictions are finally compared against light-off curves generated with a full scale DOC catalyst in conjunction with a 1.7L isuzu diesel engine.

3.1 Introduction

Global kinetics developed for a Pt DOC were discussed in chapter 2. The work in chapter 2 led to a conclusion that C_3H_6 cannot be used to represent all the HCs in the diesel exhaust, and that a more complex representation is required to capture the overall behavior accurately. Moreover, as discussed in chapter 1, although Pt catalysts give superior performance at low temperatures, their prolonged exposure to

high temperatures and high concentrations of water lead to substantial depreciation in terms of catalytic activity. While diesel exhaust is typically at low temperature ($\sim < 300^\circ\text{C}$), advanced combustion modes such as PCI provide high concentrations of HCs and CO, which when oxidized on the catalyst surface lead to high temperatures. Palladium (Pd) is often added to Pt to prevent coagulation of the Pt crystals at high temperatures. Commercially available DOC catalysts currently have a combination of Pt and Pd to ensure longevity of the catalyst. In this chapter a commercially available DOC catalyst is used for the purpose of DOC kinetics generation. The HC species used to represent the THC in the exhaust are also revisited based on a literature review.

The total hydrocarbons (THC) are traditionally separated as fast oxidizing (C_3H_6 -like) and slow oxidizing (CH_4 -like) when modeling gasoline exhaust. Hydrocarbons in diesel exhaust are substantially different in comparison to its gasoline counterpart, and hence this classification may not be entirely applicable. Traditionally diesel exhaust is known to contain heavier hydrocarbons. Bohac *et al.* [65] conducted speciation studies for diesel exhaust with a DOC. They reported that while C_2 and C_{11} are the most abundant hydrocarbons for conventional and lean PCI combustion cases, C_2 , C_6 and C_{11} are the most abundant hydrocarbons for rich PCI cases. Kryl *et al.* [66] reported oxidation rates for typical DOC conditions for a Pt/ γ - Al_2O_3 catalyst. For THC representation they used C_3H_6 to represent easy-to-oxidize HC's, toluene ($\text{C}_6\text{H}_5\text{-CH}_3$) for adsorbable aromatics, and decane ($\text{C}_{10}\text{H}_{22}$) for heavy, adsorbable, hard-to-oxidize HC's for their modeling purposes. The activation energies and pre-exponentials for $\text{C}_6\text{H}_5\text{-CH}_3$ and $\text{C}_{10}\text{H}_{22}$ were reported to be nearly identical. Tanaka *et al.* [67] assumed C_3H_6 as a representative HC for their modeling purposes.

The “global kinetics” approach developed in the previous chapter was used for the work reported in this chapter. The major differences between the work in chapter 2 [51] and this work are as follows. Firstly, in the current study, a commercial catalyst intended for more practical applications was used as opposed to a model Pt catalyst. This choice was motivated by the need to study and model a more realistic DOC catalyst which is currently used in the industry. Secondly, the upper bounds for the concentrations of THCs, CO and H₂ in the test matrix were substantially increased to incorporate concentration combinations that would result from a more aggressive PCI operation. The choice of the commercial DOC catalyst allowed the coverage of a wider concentration domain than that typically used with a Pt catalyst. Finally, since the earlier work suggested that C₃H₆ was not sufficient to represent all the hydrocarbons in the diesel exhaust, the THCs were speciated into two groups: partially oxidized HCs, represented by C₃H₆, and unburnt fuel represented by Swedish low sulfur diesel fuel (DF). For modeling purposes this DF was assumed to be C_{14.6}H_{24.8} which is quoted as ‘heavy diesel’ by Heywood [68]. The mass transfer properties of DF are estimated using experiments conducted on the bench scale reactor. These choices were motivated by the desire for more practical kinetic expressions.

The kinetics to be derived here are intended to be used within a comprehensive DOC reactor model that includes transport and inlet exhaust conditions from a realistic transient driving cycle. Care was taken in the selection of the test matrix below to include

- concentrations and temperatures that span the expected range in diesel exhaust,

- concentrations small enough to reflect the low concentrations expected in the downstream portions of an effective DOC reactor,
- elevated HC concentrations sufficient to include the result of late cylinder injection or limited HC injection directly into the upstream exhaust.

Since the oxidation reactions considered here are relatively fast, it is sufficient to consider only steady-state reaction rates relative to the time scales of a transient driving cycle (~ 1 s). Moreover, the catalyst contains no storage components, either for O_2 , as is typical when treating in stoichiometric gasoline exhaust, or for HC's. In the absence of such storage components, steady-state rates are sufficient to represent the chemical response of the reactor.

3.2 Experimental

3.2.1 Definition of Test Matrix

For the generation of reaction kinetics, the first and most important step involves defining the concentration and temperature ranges over which the resulting rates are intended, and choosing the actual test points (concentration and temperature combinations) within this domain. The upper bounds for the concentration of various species studied in this work were generated using FTP, US06 and US 2010-PCI calibration data from a production diesel engine. Concentration combinations for the species as seen at various sections of the reactor were generated by using these upper bounds and stepping them down in factors of three. Concentrations for each species were chosen to incorporate both conventional and PCI type exhaust conditions. As discussed in the 'introduction' section of this chapter, for testing purposes the total THC in diesel exhaust were speciated into two bins, namely, propylene (C_3H_6), which was used to represent the partially oxidized component of THCs, and diesel

fuel (DF), which was used to represent the unburnt portion of the THC_s. Hence the test matrix included both DF and C₃H₆. Four discrete temperatures, which were equally spaced in $1/T$, when written in K, were chosen for the test matrix. The various concentrations of the species in the test matrix are given in table 3.1.

Reasonable constraints were established on the combinations of the various con-

DF, ppm (C ₃)	C ₃ H ₆ , ppm	CO, ppm	O ₂ , %	NO, ppm	H ₂ , ppm	T, °C
2000	1000	3000	13	400	700	200
600	300	900	4	100	200	255
200	100	300		40	70	325
60	30	100				415
20	0	30				

Table 3.1: Test matrix for simulated exhaust; THC = DF+C₃H₆

centrations (e.g. THC not too low when CO is high) as shown in table 3.2 before randomly sampling 25 concentration combinations at each temperature. This ran-

THC < 2000
CO/3 < THC < 3*CO
CO/12 < H ₂ < CO

Table 3.2: Constraints for generating the test matrix; THC = DF+C₃H₆

dom sampling resulted in an acceptably small number of experimental test points while maintaining approximately uniformly coverage of the application domain to avoid biasing the results toward a particular sub-domain during the optimization procedure later.

For the NO oxidation which was observed to be substantially slower than the others, separate experiments without HC, CO, or H₂ were performed to obtain data

on the NO oxidation rate in isolation. While no NO₂ was included in the feed stream at the lower temperatures (200°C and 255°C), where the reverse reaction is negligible (informed by equilibrium), it was added to the inlet feed stream for higher temperatures (325°C and 415°C). The test matrix to infer the NO \rightleftharpoons NO₂ rate is given in table 3.3.

NO, ppm	NO ₂ , ppm	O ₂ , %	T, ppm
450	150	13	200
150	50	5	255
			325
			415

Table 3.3: NO, NO₂ and O₂ concentration levels

3.2.2 Pre-testing

A commercial DOC catalyst with 400 cpsi and proprietary noble metal composition supported on γ -Al₂O₃ was obtained from General Motors R&D and was used for all the experiments. The monolith supported catalyst was hydro-thermally aged in a furnace at 650°C for 16 hours. A constant 2.2 L/min flow of 10% H₂O in air was fed to the furnace for the entire 16 hour aging period. Without any knowledge of the catalyst formulation, one can effectively use the global kinetics reported in this work with the help of the site density. The surface site-density (a_j) based on CO chemisorption was 0.331 mol-site/m³. A detailed description of the chemisorption procedure was described in section 2.2.

3.2.3 Reactor Set-up

Experiments were conducted in a stainless tubular reactor with 1 in. o.d. for 3/4 in. diameter samples and 2 in. o.d. for 1.5 in. diameter samples. Volumetric space velocities between 50 000 and 2 000 000 h⁻¹ were achieved by varying catalyst

size and overall flow rates. In comparison to the work in chapter 2 it was necessary to inject Swedish low sulfur diesel fuel (properties of the fuel can be found in Han *et al.* [69]). Fuel was injected into the system with a Cole-Parmer 74900-10 syringe pump. Fuel was vaporized and introduced into the system by passing the heated feed stream over a high temperature fiberglass wick attached to the syringe pump. All experiments were conducted at 1.6 atm to ensure proper flow into the FTIR. The catalyst sample was heated by flowing a mixture of air, N₂, CO₂ and vaporized water through two inline heaters. Three type-K thermocouples were used to monitor the temperatures upstream, downstream and 3/4 in. from the entrance of the reactor. All measurements were taken with 10% CO₂ and 8.7% water in the feed stream. The reactor set-up used for this work is shown in figure 3.1.

The reactor inlet and outlet flows were analyzed using a MKS MultiGas 2030 process stream FTIR for CO, CO₂, NO, NO₂, N₂O, NH₃, C₃H₆, formaldehyde, CH₄ and water. No measurable quantities of N₂O, NH₃ or other hydrocarbons (e.g., CH₄, aldehydes (R-CHO)) were detected with the FTIR during any of the experiments. Hydrogen (H₂) was analyzed using a V&F H-sense mass spectrometer. A Horiba hot flame ionization analyzer was used to detect the THC in the system. The DF concentration was obtained by subtracting the C₃H₆ concentration, measured with the FTIR, from this THC measurement, based on the assumption that DF contains very little of any low-molecular weight species, C₃H₆ in particular [69]. Inlet concentrations of all species were adjusted to within 2% of the desired inlet concentration for each run based on the analyzer readings.

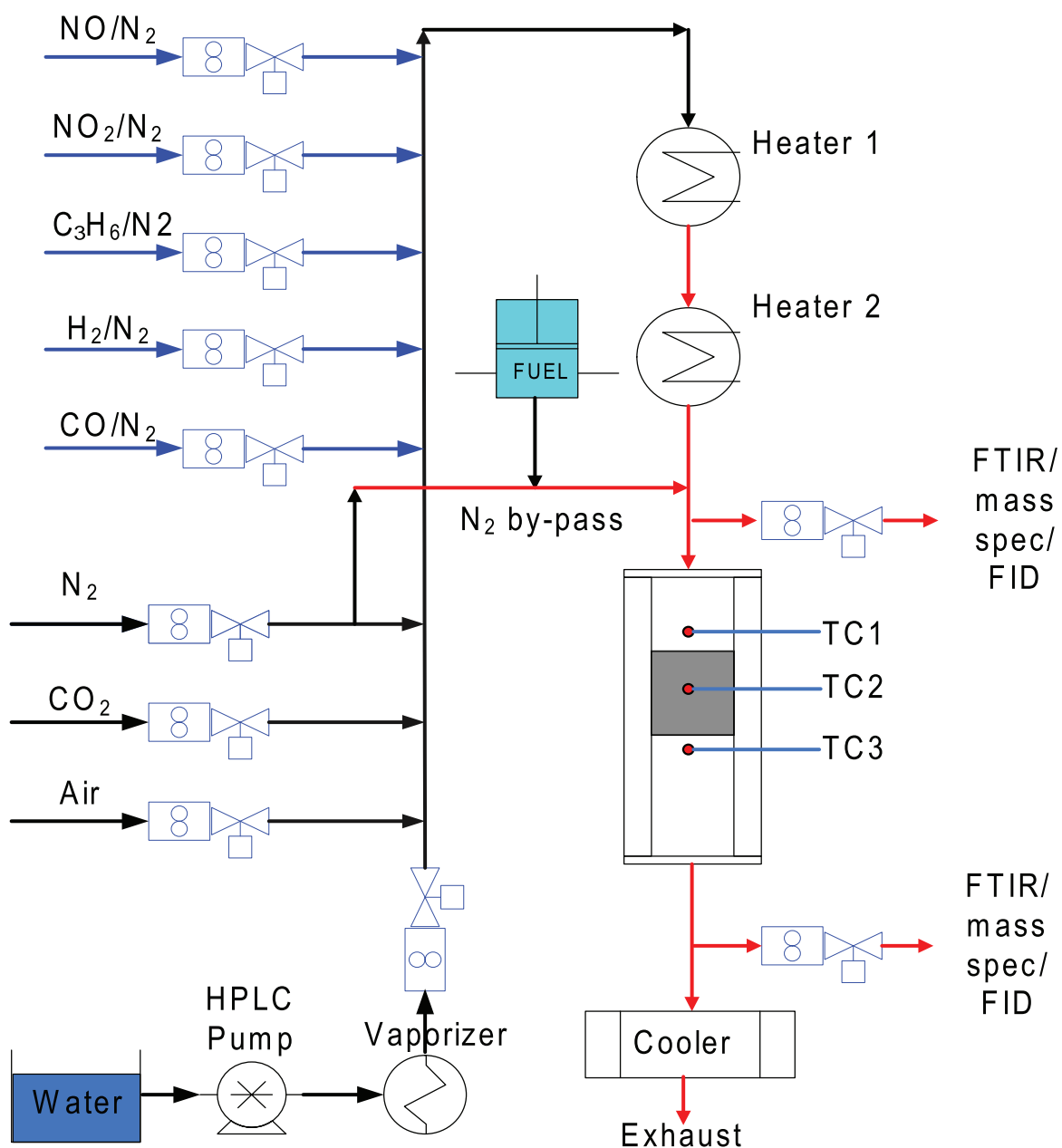


Figure. 3.1: Experimental set-up of the bench scale reactor for DOC kinetics development - Commercial catalyst with C_3H_6 and DF as representative HCs

3.3 Modeling

The problem of generating global reaction kinetics involves solving an outer problem and a corresponding inner problem. The outer problem involves assuming a rate

form for each of the reactions under consideration, and performing an optimization to minimize the difference between the experimental data and the predictions based on these assumed rates to generate a set of reaction parameters (A_i and E_i) which best describe the experiments. The outer problem would hence need an objective function which reflects on this difference between model results and experiments. For each evaluation of the objective function, an inner problem needs to be solved, where the exit concentrations for all the test points (experimental conditions) are evaluated, for a given set of reaction rates and inlet conditions. For the solution of the inner problem one would also need the transport properties of all the species. In this section the equations used to construct the inner and outer problems are briefly defined for continuity. For more detailed discussions on each of these sections, the reader is referred to chapter 2.

3.3.1 Inner Problem

The equations used to solve for the species concentrations can be described by a system of DAEs (differential algebraic equations) shown in equation (3.3.1). These equations are used to evaluate the exit concentrations for various inlet conditions. An energy balance equation is not solved. Rather, we the temperatures measured with the three thermocouples in the reactor setup are used to estimate the temperature field. The basic governing equations are given in equation (3.3.1). The definition of various terms are given in the appendix.

$$\frac{w}{A} \frac{dx_{g,i}}{dz} = -k_{m,i} S(x_{g,i} - x_{s,i}) = \sum_{j=1}^{nrct} a_j s_{ij} r_j \quad \text{for } i = 1, \dots, nsp \quad (3.3.1)$$

The boundary condition for equation (3.3.1) is

$$x_{g,i}(0) = x_i^0 \quad (3.3.2)$$

The mass transfer coefficient is calculated based on the asymptotic Sherwood number and the binary diffusivity of individual trace species.

$$k_{m,i} = \frac{Sh}{D_h}(cD_{i,m}) \quad (3.3.3)$$

The binary diffusion coefficients for each trace species in the gas mixture was taken as though the mixture were nitrogen. We use the correlation given by Fuller *et al.* [62] for each of these as shown in equation (3.3.4).

$$cD_{i,m} = \frac{3.85 \times 10^{-5} T^{0.75} \sqrt{\frac{1}{M_i} + \frac{1}{M_{N_2}}}}{[\Sigma_i^{1/3} + \Sigma_{N_2}^{1/3}]^2} \quad (3.3.4)$$

3.3.2 Transport Property of Diesel Fuel

The mass transfer coefficient is unique for each of the species because it is based on the binary diffusivity of each trace species with respect to the mixture, approximated by N_2 for the purpose of this work. As mentioned in its definition, the binary diffusivity for each species requires the molecular weight and diffusion volumes of the respective species and N_2 (equation (3.3.4)). The diffusion volume for simpler molecules is well reported in the literature, viz. CO, H_2 , NO, NO_2 and N_2 . For other hydrocarbons not specifically reported, such as C_3H_6 , one can use the generic correlation given in Poling *et al.* [70], namely, $\Sigma_{C_xH_y} = 15.9x + 2.31y$. For the calculations reported in this work diesel fuel was assumed as ‘‘Heavy Diesel’’ as given in Heywood [68]. The molecular weight of this compound is 200 and its molecular formula is $C_{14.6}H_{24.8}$. Therefore, this characterization of the unburnt fuel (‘‘Diesel fuel’’ = DF) in the exhaust enters the model calculations through this molecular weight and the diffusion volume of DF, Σ_{DF} . Based on the generic formula above for HC’s, we obtain $\Sigma_{DF} = 289$.

One can calculate a mass-transport limited solution for any particular species by assuming infinitely fast reaction ($x_s = 0$) and then simply integrating the LHS of equation (2.3.1). The transport limited solution presents the upper bound for the conversion of a particular species.

$$\int_{x_{g,i}^{in}}^{x_{g,i}^{out}} \frac{dx_{g,i}}{x_{g,i}} = \frac{-k_{m,i}SA}{w} \int_0^L dz \quad (3.3.5)$$

This gives

$$\text{conv} \equiv \frac{x_{g,in} - x_{g,out}}{x_{g,in}} = 1 - e^{\frac{-k_{m,i}SV}{w}} \quad (3.3.6)$$

Figure (3.2) shows the transport limited solution resulting from equation (3.3.6) for DF, compared against its corresponding experimental conversions. An average

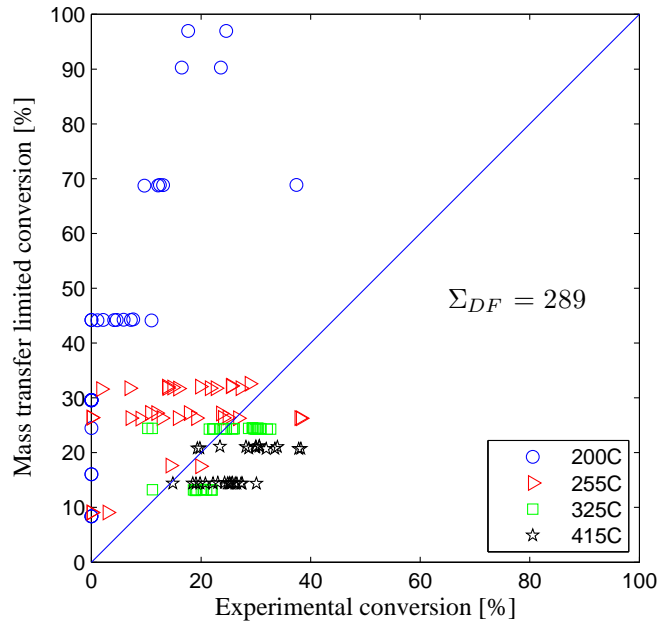


Figure. 3.2: Experimental conversion plotted against transport limited conversions for DF with $\Sigma_{DF} = 289$

between the inlet and exit temperatures was used to calculate the scaled mass transfer coefficient $k_{m,i}$. The value here of $\Sigma_{DF}=289$ was obtained from the generic recommendation for an arbitrary HC mentioned above [70]. It can be seen from the plot

that experimental conversions for DF at high temperatures (325°C and 415°C), exceed the upper bound of the transport limited solution. This behavior was commonly not observed for the other species. Even though the length of our reactor channels was relatively short, any enhancement of mass transfer rates due to entrance effects, which are neglected in this model, was too small to account for this discrepancy. This anomaly was interpreted as an opportunity to infer a more reasonable value for Σ_{DF} , in view of the attempt to represent the complex mixture of diesel fuel as a single simple molecule $C_{14.6}H_{24.8}$. Also this value for Σ_{DF} did not incorporate several correction factors given in Poling *et al.* which account for the presence of ring or oxygenated compounds. A Σ_{DF} of 80 was found to be sufficient to eliminate this un-physical behavior (See figure (3.3)). Since temperature was approximated with an average value (between inlet and outlet) when calculating the transport limited solution, a few points at the higher end of the temperature are beyond the transport limited solution. For all the subsequent work in this paper, a Σ_{DF} of 80 was used.

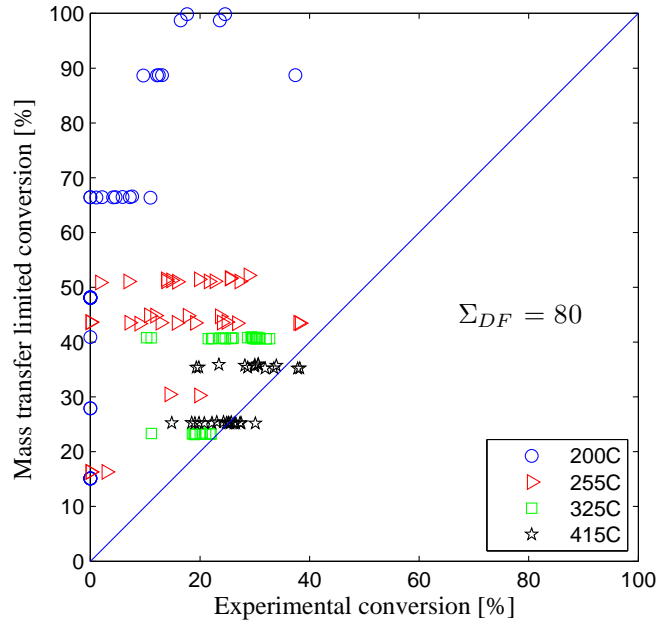


Figure. 3.3: Experimental conversion plotted against transport limited conversions for DF with $\Sigma_{DF} = 80$

3.3.3 Outer Problem

For the optimization process we used MATLAB's constrained minimizer, namely 'fmincon'. Based on the experience with the work in chapter 2, the optimization parameters are scaled based on the discussion presented in section 2.3. For the sake of continuity, the details of this scaling are briefly described below.

The dimensionless activation energy for rate or adsorption constant (as written in equation 3.4.1), can be scaled using a reference temperature $T = T_r$ and can be written as,

$$\widehat{E} = \frac{E}{RT_r}. \quad (3.3.7)$$

The scaled pre-exponential in the inhibition terms of equation 2.4.3 is given as

$$\widehat{A}a_i = Aa_i e^{-\widehat{E}a_i} c_r x_{r,i}, \quad \text{where } c_r = c(T_r) = \frac{p}{RT_r}. \quad (3.3.8)$$

Finally the scaled pre-exponential for the rate constant is

$$\widehat{A}_i = \frac{V a_i}{w_r} A_i e^{-\widehat{E}_i} c_r^2 x_{r,i} x_{s,O_2}, \quad (3.3.9)$$

where a_i is the site-density and x_{s,O_2} is the reference mole-fraction for O_2 (present in excess). The scaling of the activation energies and pre-exponential terms of the rate and adsorption constants will allow each of these constants to be expressed in $O(1)$.

The definition of the objective function is the key to successful parameter optimization. The objective function or norm which is used for the optimization process is based on either the gas phase species exit mole-fractions (x_g) or the difference between the inlet and the outlet gas phase mole-fractions ($\Delta x_g = x_{g,in} - x_{g,out}$) according as the experimental conversion for a species in particular test point is less

than or greater than 50%. The 50% barrier is picked for simplicity since either choice works equally well for moderate conversions. A similar procedure is employed even plotting the results. Δx_g comparison is plotted for tests which have less than or equal to 50% conversions and x_g comparison is plotted when conversions are over 50%.

This norm is suitably scaled by the number of species being considered in any particular optimization ($n_{sp'}$), the number of temperatures being considered (n_T), and the number of points at each temperature (n_j), such that each data point contributes equally at each temperature, and each temperature and species contributes equally to the overall norm calculation. The norm definition is given in equation (3.3.10), where the sum of the two log terms is interpreted as taking one term or the other depending on the conversion for that species.

$$\text{norm}^2 = \frac{1}{n_{sp'}} \sum_{i=1}^{n_{sp'}} \frac{1}{n_T} \sum_{j=1}^{n_T} \frac{1}{n_j} \sum_{k=1}^{n_j} \left[\log^2 \left[\frac{\Delta x_{g,i}^m}{\Delta x_{g,i}^e} \right]_{conv \leq 50\%} + \log^2 \left[\frac{x_{g,i}^m}{x_{g,i}^e} \right]_{conv > 50\%} \right] \quad (3.3.10)$$

The experimental error in measurement was taken into account in the norm calculations. Experimentally C_3H_6 , CO and NO were measured within 5 ppm. H_2 was measured more accurately and its error in measurement was 3 ppm. The THC measured by the FID was within 10 ppm, and the same significance tolerance was employed for DF. In essence we dropped from the summation any term whose corresponding x_g or Δx_g was less than 5 ppm (10 ppm for DF and 3 ppm for H_2) for norm calculation purpose.

3.4 Results and Discussion

3.4.1 Initial Rate Forms and Guesses for Optimization

As described earlier, the nature of the global rate generation process requires the specification of the rate forms and rate parameters for the various reactions of interest before any optimization is performed. For the scope of this study, a modified version of conventional Langmuir-Hinshelwood forms which are commonly used for similar work in the literature were used. Inhibition/enhancement terms were successively added/removed to check if there is a significant improvement in our norm at each stage of optimization. Roughly speaking, a term is added if there is a substantial improvement in the norm after re-optimization. A term was retained if the resulting norm worsens significantly upon its removal. Alternatively, a term was removed if nearly the same norm could be maintained without it.

Oxidation rates from Voltz *et al.* as written in Oh *et al.* were modified and used for this exercise. The rate forms in Oh *et al.* were first transformed so that they are functions of concentrations (mol/m^3) rather than mole-fractions. Then the second term in the inhibition (as given in Voltz *et al.*, namely $(1 + K_{\text{C}_3\text{H}_6, \text{CO}} c_{\text{C}_3\text{H}_6}^2 c_{\text{CO}}^2)$), was removed owing to its empirical nature, and to minimize the degrees of freedom. Next, the exponent for the NO concentration was set to unity to ensure that the rates are differentiable with respect to NO at zero NO concentration. Finally, we added the effect of DF in the inhibition term to allow for its effect on the rates along with the effects of C_3H_6 and CO. The rate forms which we used as a starting point for our optimizations are therefore given by equation (3.4.1).

$$r_i = \frac{k_i c_{s,i} c_{s,\text{O}_2}}{G_1} \left[\frac{\text{mol}}{\text{mol-site} \cdot \text{s}} \right], \quad (3.4.1)$$

where

$$G_1 = (1 + K_{s,DF}c_{s,DF} + K_{C_3H_6}c_{s,C_3H_6} + K_{CO}c_{s,CO})^2(1 + K_{NO}c_{s,NO}). \quad (3.4.2)$$

Note that c_i represents the concentration in $[mol/m^3]$ of species i . All rate and adsorption constants (k_i and K_i) are Arrhenius functions of temperature.

With the initial rate forms defined, the next step was to generate initial guesses for the various rate parameters, namely A_i and E_i , before optimizing for all the reaction parameters. The division of the temperature regime into discrete bins aids in the process of generating a proper initial guess in our case. For generating initial rate and adsorption constants for DF, C_3H_6 , CO and H_2 , NO was assumed to linearly vary between inlet and exit. Since in most of the cases there was very little NO conversion, the linear approximation for NO is well justified. The optimization is performed on individual k_i and K_i (rate and adsorption constants) for the rate forms given in equation (3.4.1) at a fixed temperature. Since the scaling ensures that the variables (scaled k_i and K_i) are $O(1)$, any number which is $O(1)$ is suitable as an initial guess. The results from the optimization at individual temperatures are plotted in an Arrhenius plot ($\log k_i$ vs $1/T$) to generate proper initial guesses for all pre-exponentials and activation energies. Typical Arrhenius plots generated for initial guess of the rate constant for DF (k_{DF}) is shown in figure (3.4).

3.4.2 NO Oxidation

Separate experiments which were conducted with only NO, NO_2 and O_2 is in the feed stream were used to infer the $NO + 0.5O_2 \rightleftharpoons NO_2$ rate. Note that this reaction is reversible and is limited by equilibrium. All the data obtained from these sets of experiments gave differential conversion data. The global reaction rate that was

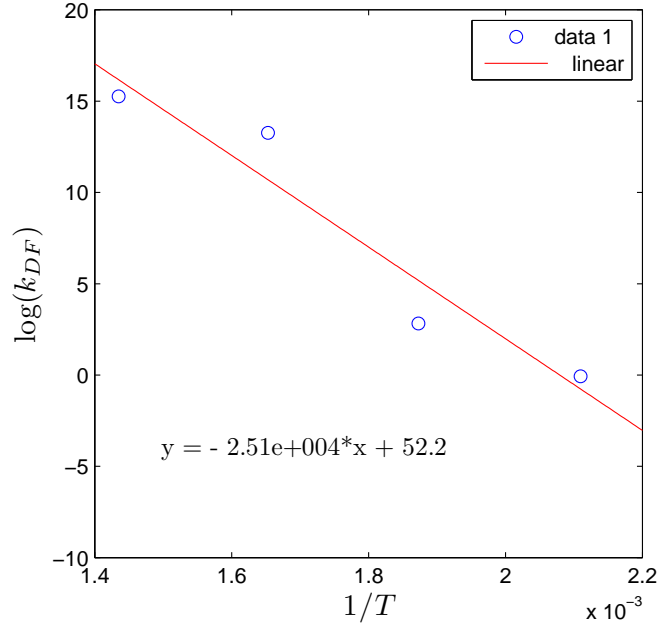


Figure. 3.4: Initial guess for A_{DF} and E_{DF} from optimization at individual temperatures

developed in the previous chapter for the NO oxidation (utilizing only NO+NO₂+O₂ feed) was used as a starting point for this work. This rate form represented the data for the Pt catalyst over wide concentration and temperature domain.

$$r_{NO} = \frac{k_{NO}}{(1 + K_{NO}c_{s,NO})} \left[c_{s,NO} \sqrt{c_{s,O_2}} - \frac{c_{s,NO_2} \sqrt{c_R}}{K_{eq}} \right] \quad (3.4.3)$$

c_R is the total concentration at the reference pressure of 1 atm. K_{eq} is the equilibrium constant, based on the free energy of the NO oxidation reaction.

$$K_{eq} = 1.5 \times 10^{-4} e^{6864/T} \quad (3.4.4)$$

k_{NO} and K_{NO} represent the rate constant and adsorption constants, respectively, both with Arrhenius forms of temperature dependency.

The rate expression given in equation (3.4.3) was first optimized for data obtained with feeds containing only NO, NO₂ and O₂. A parity plot obtained with the optimized parameters appears in figure (3.5). Note that we plot only $\Delta x_g = (x_g^{in} - x_g^{out})$

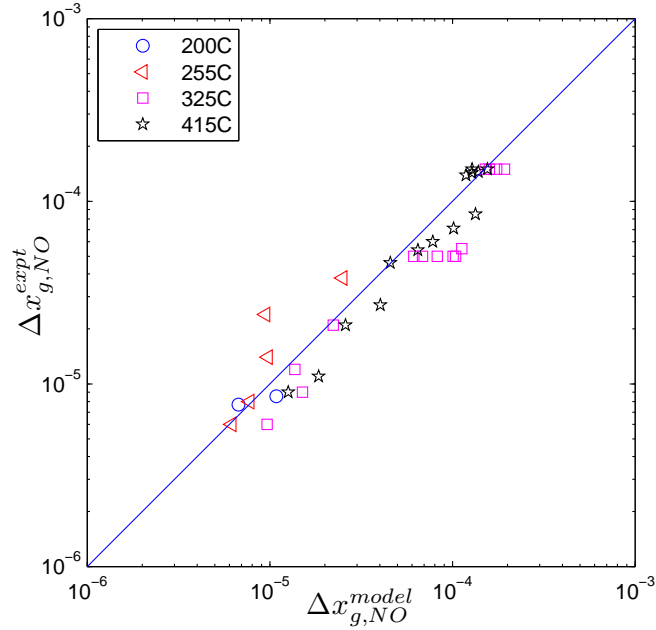


Figure. 3.5: Comparison of Δx_{NO} between model and experiment for cases which has only NO, NO₂ and O₂ in the feed-stream (no reductant)

because all the data generated for NO+NO₂+O₂ in the stream had conversions less than 50%. It was concluded that this model captured the experimental data well over the entire concentration and temperature regimes. However, this rate expression should also predict small NO conversions in the presence of reductant in the stream since no significant net NO oxidation reaction was observed in the presence of any reductants. To evaluate this rate the experimental Δx_{NO} is plotted against model Δx_{NO} in figure (3.6) for cases which have reductant in the stream.

The model clearly over-predicts the NO conversions by up to an order of magnitude in comparison to the experimental data when reductants are present in the feed. The rate hence needs to be modified when being used for these cases. As in the previous work, the similarity in the NO inhibition terms in equations (3.4.2) and (3.4.3) when the reductants are absent ($c_{s,DF} = c_{s,C_3H_6} = c_{s,CO} = 0$), was used to generalize equation (3.4.3) to equation (3.4.5). The final rate form which was used

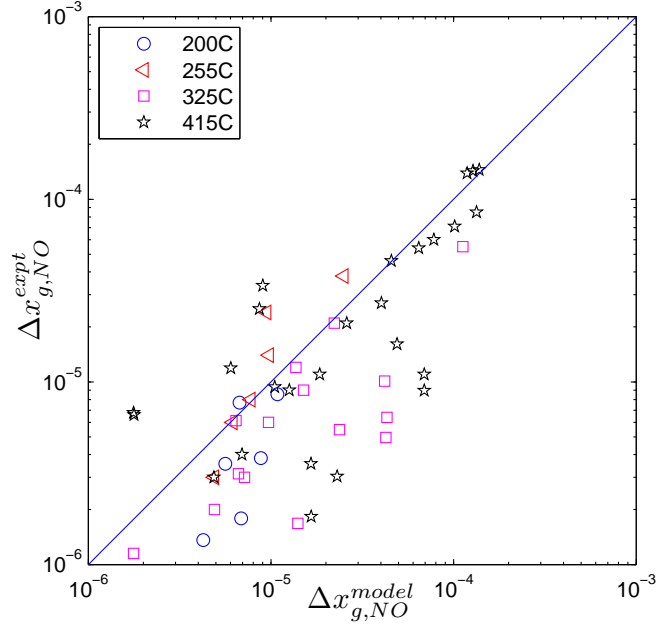


Figure. 3.6: Comparison of Δx_{NO} between model and experiment in the presence of reductants in the feed-stream using the rate form of equation (2.4.5).

as a starting point for NO oxidation is given as equation (3.4.5).

$$r_{NO} = \frac{k_{NO}c_{s,NO}\sqrt{c_{s,O_2}}}{G_1} \left[1 - \frac{c_{s,NO_2}}{K_{eq}c_{s,NO}} \sqrt{\frac{c_R}{c_{s,O_2}}} \right], \quad (3.4.5)$$

where G_1 is given by equation (3.4.2). The optimization of the rate constant k_{NO} in this last form is performed when the optimization of the full problem is considered in the next section.

3.4.3 Optimization of the Full Problem

With the rate forms (equations (3.4.1) and (3.4.5)) and initial guesses known, all the reactions (DF, C_3H_6 , CO, H_2 and NO (NO_2)) are optimized for the entire concentration and temperature domains. The objective function (norm) value at the end of the optimization was **0.4529**. A rate simplification process similar to the one described in chapter 2 was followed, wherein terms were systematically added or removed to account for rate inhibition/enhancement, in order to assess the mer-

its of the resulting rate forms in terms of simplicity and objective function. With each term individually removed, the full optimization with the resulting form was performed again to obtain a new solution (new set of A 's and E 's). Table 3.4 gives the value of the norm when DF, C_3H_6 , CO and NO were removed individually from the inhibition term. The objective function values given in table 3.4 are obtained

Term removed	Final norm
$K_{DF} c_{s,DF}$	0.4529
$K_{C_3H_6} c_{s,C_3H_6}$	0.4529
$K_{CO} c_{s,CO}$	1.1354
$K_{NO} c_{s,NO}$	0.7853

Table 3.4: Final norm after various terms in the inhibition terms were dropped

after each of the terms are removed individually and optimizing the overall problem without these terms present. The scaled pre-exponentials for the inhibition terms of DF and C_3H_6 (corresponding to Aa_{DF} and $Aa_{C_3H_6}$) were very small in magnitude at the end of the first optimization of the full problem. Hence their removal from the inhibition term as shown by table 3.4 resulted in a small perturbation from the solution where (DF+ C_3H_6 +CO+NO) are in the denominator. Once the exercise of removing individual terms from the rate was performed, the rate parameters in the inhibition terms were removed in sets of two to further simplify the overall rate expressions. Removing both the DF and C_3H_6 components from the inhibition and re-optimizing, as expected, did not lead to any perceivable change in the norm. As mentioned above, the scaled pre-exponentials for DF and C_3H_6 in the inhibition were very small at the end of the overall optimization for the first time. The lowest objective function value (= 0.4529) was retained when both these terms were removed. Removing CO or NO in addition to removing DF and C_3H_6 (discussed above) gave

an unacceptable norm value (>3 in case of CO and >2 in case of NO). Hence these terms (CO+NO) were retained in the inhibition term for all the rates.

H₂ was present in the feed stream, and hence a possible enhancement effect of H₂ on the other rates was also studied. A term, $(1 + K_{H_2}c_{s,H_2})$, was included in the numerator of all the rates to represent any H₂ enhancement. Re-running the optimization gave a very marginal improvement in the overall norm. The final norm with the inclusion of the H₂ enhancement term was **0.4527**. Such a small improvement in the norm was insufficient to justify the inclusion of the H₂ enhancement term and hence it was not included in the final rate forms.

The effect of the reductants on the NO rate would be captured by the first part of the inhibition term (equation (3.4.2)). The low-temperature data (200°C and 255°C) with reductant present showed almost no NO conversion, and none which passed the cut-off criteria ($\Delta x_g > 5$ ppm). Therefore this low temperature NO reaction data with reductant was not passed to the optimizer, and so it cannot serve to constrain the resulting rate form. This weakness in the data revealed itself when light-off curves generated with this solution (set of A 's and E 's) were compared against reactor generated light-off curves (figure (3.7)). The model shows too little inhibition, but, as explained above, the effect of the reductant inhibition on the NO rate is not quantitatively constrained by the results from the test matrix. Rather, this inhibition can be considered as extrapolated from behavior at higher temperature and constrained by the inhibition measured in the other rates, since this same inhibition term is being used throughout. Therefore, some adjustment to the reductant inhibition for the NO rate would be desirable and not inconsistent with the data in the

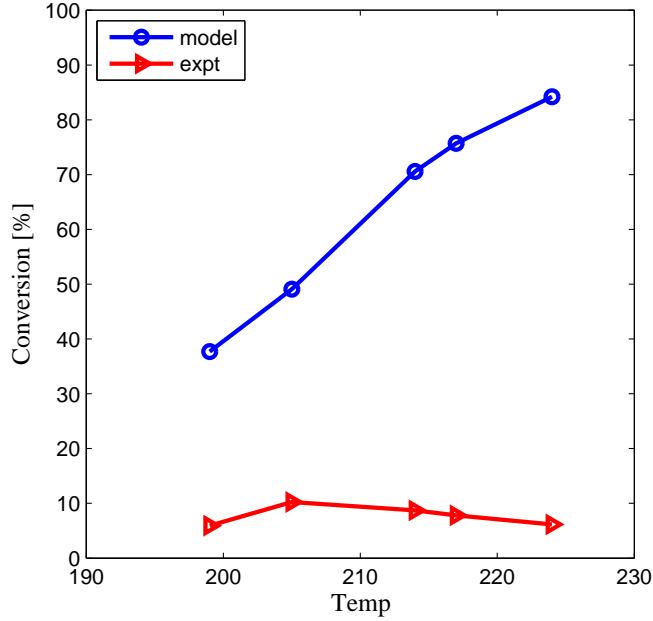


Figure. 3.7: Comparison of NO light-off curves between model which used NO rate based on CO and NO inhibition and small-scale reactor experiments. The inlet NO was 40 ppm.

test matrix. However, it is not desirable to go so far as to quantitatively match the light-off data in figure (3.7), since even 10% conversion of the 40 ppm inlet NO is below the measurement confidence threshold. Rather an alternate reductant inhibition term was desired, which results in qualitatively no NO conversion at the low temperatures typical of the light-off data shown. After a certain number of attempts, it was found that a similar, simple reductant inhibition for NO based on DF rather than CO solved this issue.

$$G_{NO} = (1 + K_{s,DF}c_{s,DF})^2(1 + K_{NO}c_{s,NO}) \quad (3.4.6)$$

A fundamental desirability for using the same inhibition term for all the rate is recognized. However, the overall goals of this work, including the description of the reactor behavior by simple rate expressions, were best served by making this compromise. All the rate expressions were re-optimized for with new NO inhibition term. The norm value corresponding to the final solution was **0.4529**, which is the

same as the previous norm value within the first four digits. The light-off curve comparison, generated using small-scale reactor measurements and the model which uses the corrected inhibition term is given in figure (3.8). Both curves show essentially

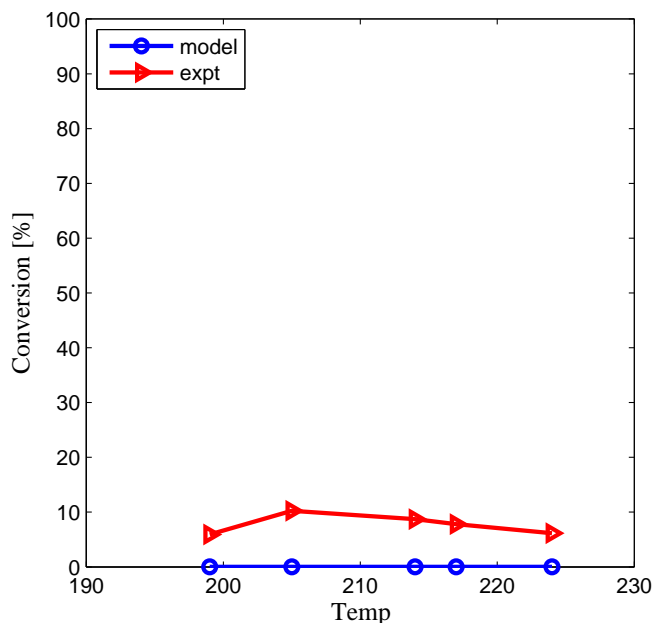


Figure. 3.8: Comparison of NO light-off curves between model which used NO rate based on DF and NO inhibition and reactor small-scale experiments

no conversion as desired.

The absence of the terms for inhibition by DF and C_3H_6 or for enhancement by H_2 , when considering the reactions for DF, C_3H_6 , CO or H_2 , should not be interpreted as precluding these effects. Detailed experiments designed specifically to elucidate these details for these individual reactions are needed to clarify the absence or presence of these commonly-observed effects. Rather, it is claimed that including these effects in the current global reaction scheme is not required to describe rates over the concentration and temperature regimes considered in this study, especially when it is emphasized to keep the total degrees of freedom represented by the kinetic

parameters small. While these results are designed to capture the overall trends quantitatively, the parity plots below show that predictions for individual cases can still contain substantial errors that could mask additional chemical effects.

The final rate forms resulting from the optimizations discussed above are given by equations (3.4.7) and (3.4.8).

$$r_i = \frac{k_i c_{s,i} c_{s,O_2}}{G} \quad \left[\frac{\text{mol}}{(\text{mol} - \text{site}) \cdot \text{s}} \right] \quad i = DF, C_3H_6, CO, H_2 \quad (3.4.7)$$

$$r_{NO} = \frac{k_{NO}}{G_{NO}} \left[c_{s,NO} \sqrt{c_{s,O_2}} - \frac{c_{s,NO_2} \sqrt{c_R}}{K_{eq}} \right] \quad \left[\frac{\text{mol}}{(\text{mol} - \text{site}) \cdot \text{s}} \right] \quad (3.4.8)$$

where

$$G = (1 + K_{CO} c_{s,CO})^2 (1 + K_{NO} c_{s,NO}), \quad (3.4.9)$$

$$G_{NO} = (1 + K_{DF} c_{s,DF})^2 (1 + K_{NO} c_{s,NO}), \quad (3.4.10)$$

$$k_i = A_i * e^{-E_i/RT}, \quad (3.4.11)$$

and

$$K_i = A_{a_i} * e^{-E_{a_i}/RT}. \quad (3.4.12)$$

The rate constants corresponding to these reactions are given in table (3.5). For modeling purposes DF concentrations should be specified as absolute concentrations (not on some ‘equivalent’ basis such as C₃ etc.) when using these rates. The corresponding heats of combustion which one needs to input to a more comprehensive DOC model that includes an energy equation are given in table (3.6).

Figures (3.9) - (3.13) show the parity plots comparing the model predictions versus the experimental observations for DF, C₃H₆, CO, H₂ and NO (NO₂) for all the operating points. All points with conversions less than 50% (experimental conversion) are plotted in a $\Delta x_g (x_g^{in} - x_g^{out})$ plot and all points

Rate constants	Value
A_{DF}	2.918×10^5
E_{DF}	2.42×10^4
$A_{C_3H_6}$	1.566×10^{19}
$E_{C_3H_6}$	1.594×10^5
A_{CO}	1.183×10^{12}
E_{CO}	8.133×10^4
A_{H_2}	9.830×10^4
E_{H_2}	1.531×10^4
A_{NO}	1.327×10^3
E_{NO}	6.721×10^3
Aa_{CO}	2.48×10^2
Ea_{CO}	5.113×10^3
Aa_{NO}	2.420×10^{-1}
Ea_{NO}	-4.042×10^4
Aa_{DF}	2.020×10^{-17}
Ea_{DF}	-2.347×10^5

Table 3.5: Rate constants as a result of the final optimization of the full problem - Final norm = 0.4529 and DF is $C_{14.6}H_{24.8}$

with conversion greater than 50% (experimental conversion) are plotted in a x_g (x_g^{out}) plot (exit concentrations) for the reasons discussed in the objective function definition section. It is noted that the proposed rate forms capture the experimental behavior over several orders of magnitude of concentrations and a wide temperature range.

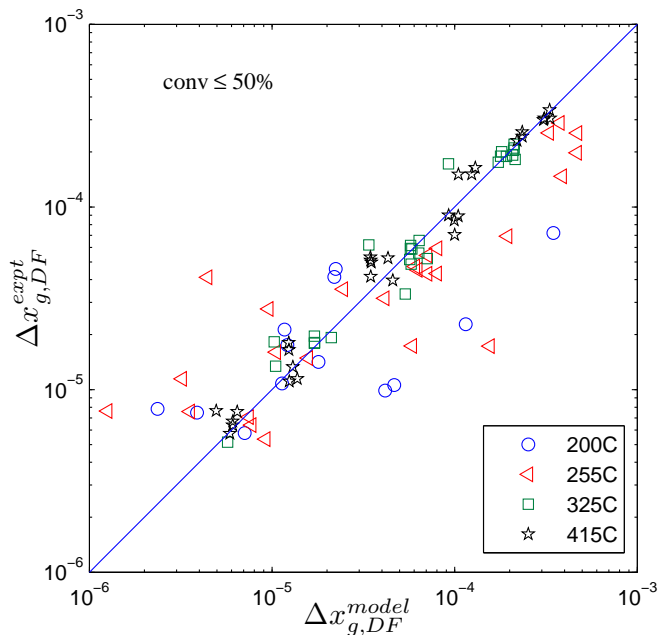
To capture the inhibition effects due to CO and NO, a simple alternative rate form would be

$$r_i = \frac{k_i c_i c_{O_2}}{(1 + K_{CO} c_{s,CO} + K_{NO} c_{s,NO})^2}, \quad (3.4.13)$$

where i is a typical species. Attempts to optimize for this rate form gave a norm value ≈ 0.6 , which was considerably higher than that obtained with the results re-

Reaction	ΔH_i
DF	-8560×10^3
C_3H_6	-1926×10^3
CO	-283×10^3
H_2	-242×10^3
NO	-57.1×10^3

Table 3.6: Heats of combustion

Figure. 3.9: Comparison between experiment and model predictions - Δx_g for DF

ported in this paper, so rate form was not explored further.

The clustering of points in the x_g plot for C_3H_6 is mainly because some of the experimental conversions at this end were transport limited (very fast reaction rate), so the outlet concentrations depend primarily on inlet C_3H_6 concentration, and space velocity, which themselves cluster at discrete values. In these cases the model should be able to predict a transport limited solution as it rightly does. The x_g comparison H_2 plot (figure (3.12)) in comparison to our previous results (chapter 2), shows a

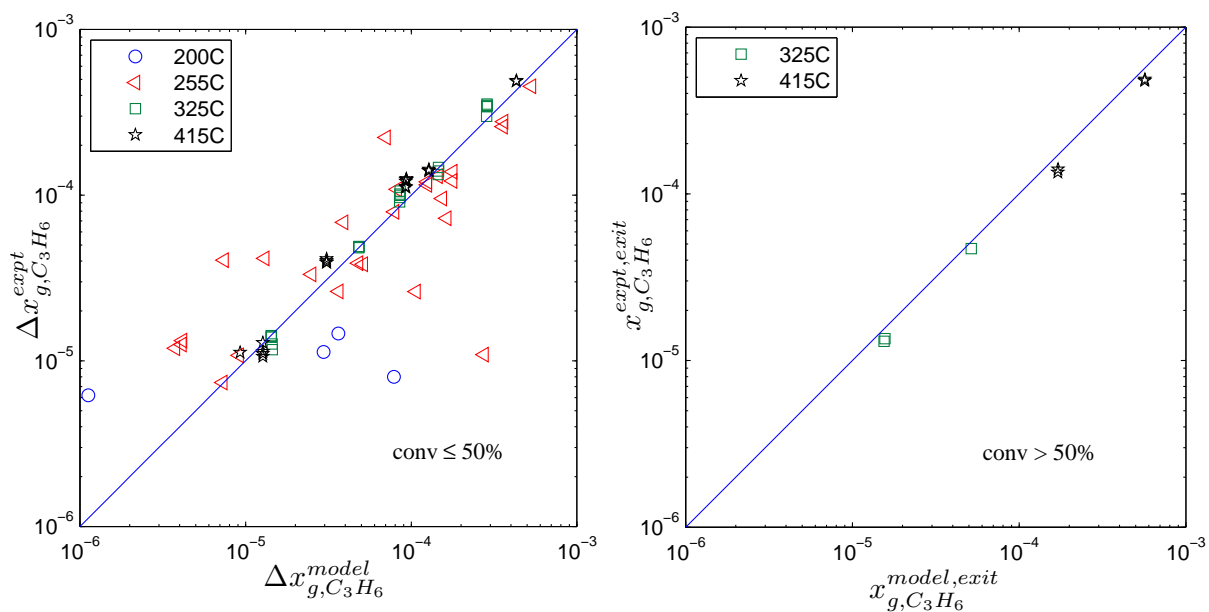


Figure. 3.10: Comparison between experiment and model predictions - Δx_g and x_g^{exit} for C_3H_6

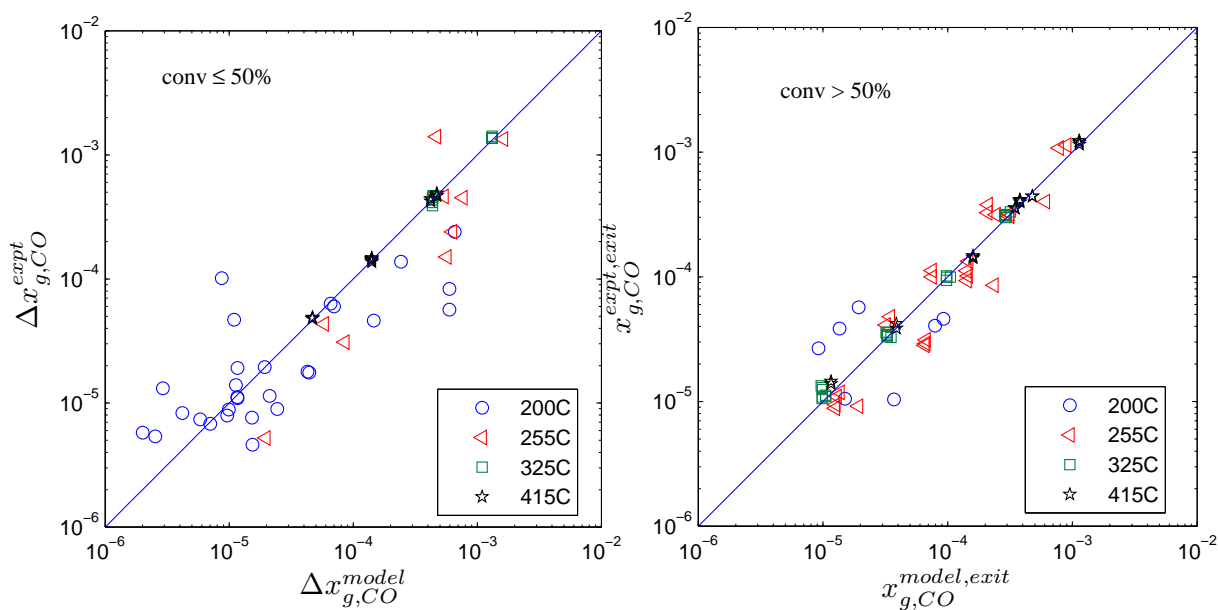


Figure. 3.11: Comparison between experiment and model predictions - Δx_g and x_g^{exit} for CO

better trend overall indicating that the experimental behavior was properly captured.

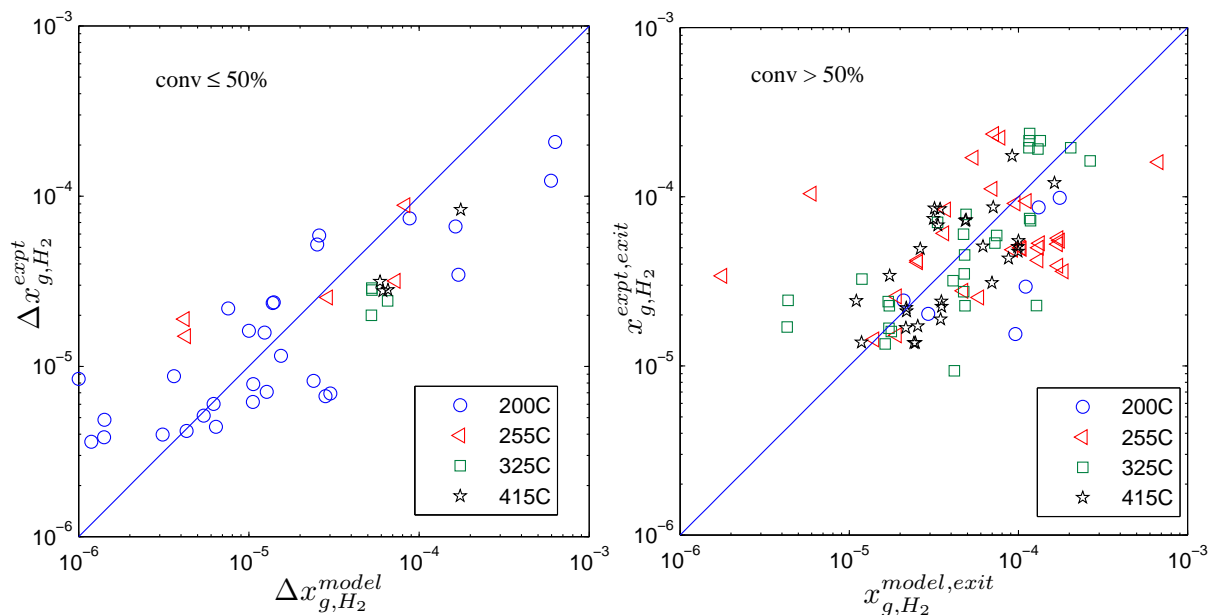


Figure. 3.12: Comparison between experiment and model predictions - Δx_g and x_g^{exit} for H_2

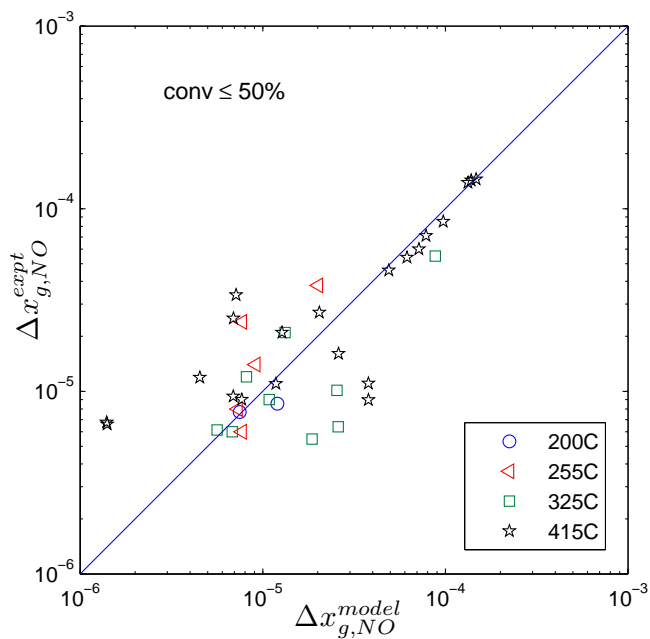


Figure. 3.13: Comparison between experiment and model predictions - Δx_g for NO - Feed consists of points with and without reductant

3.4.4 Reactor Validation

Light-off curves were generated using the same small-scale reactor which was used for generating data needed for the rate generation process by running at real-

istic (engine exhaust application) space velocities. This step serves as a transition between the development of reaction kinetics using the model and model application to engine-level aftertreatment systems. It also helps ensure that the small-scale laboratory reactor (which is used to infer rates) behaves like full-scale DOC under similar operating conditions. The inlet conditions used for generating the light-off curves are given in table 3.7.

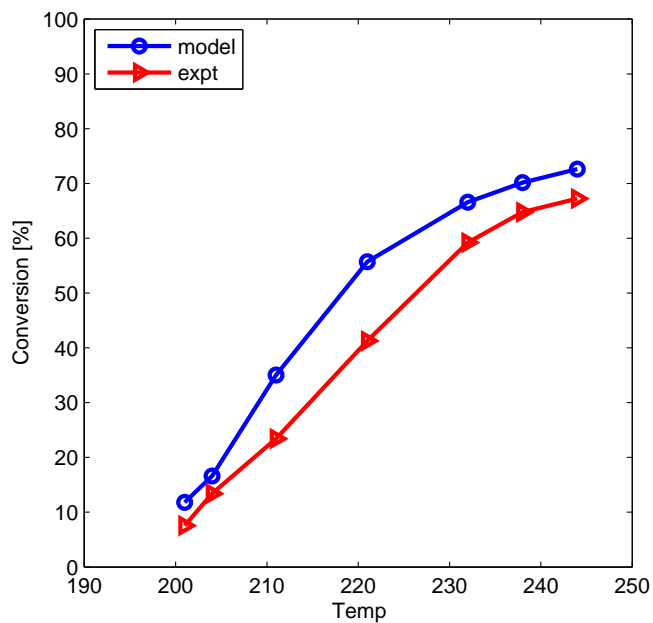
DF (C_3)	220 ppm
C_3H_6	130 ppm
CO	2000 ppm
H_2	435 ppm
NO	40 ppm
NO_2	0 ppm
O_2	8.5%

Table 3.7: Inlet conditions for light-off curves generated with small-scale reactor with realistic space velocities

For constant inlet feed the temperature was ramped up to get the desired curves. The space velocity was maintained at $60,000 \text{ h}^{-1}$, which is typical for a full-scale reactor. Temperature was varied between 200°C and 240°C . The comparisons between model and experiments are shown in figures (3.14(a)) - (3.15(b)). The validation for NO has already been shown in figure (3.8). The model clearly captures the overall trend for all the species very well.

3.4.5 Engine Validation

Light-off curves were generated for THCs and CO using the 1.7L Isuzu diesel engine described in chapter 2 and in Knafl *et al.* [64] in conjunction with a full scale DOC with the same catalyst formulation as that used with the bench scale reactor. This catalyst also followed the same aging procedure as the one used with



(a) DF

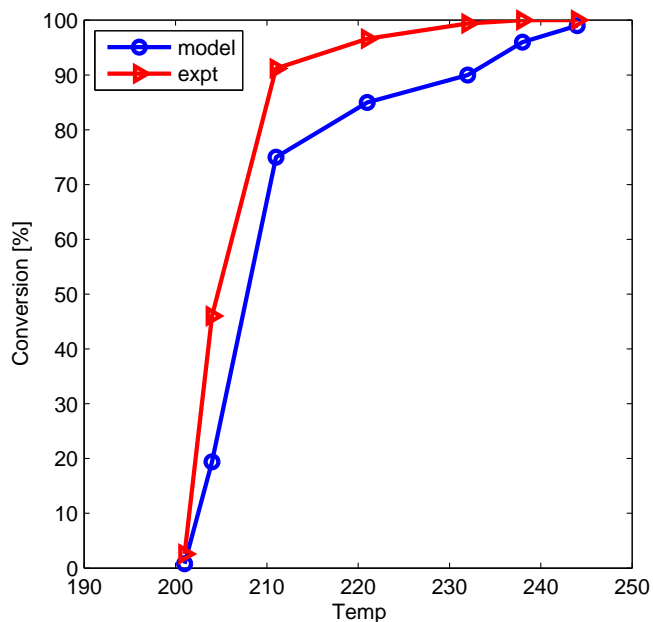
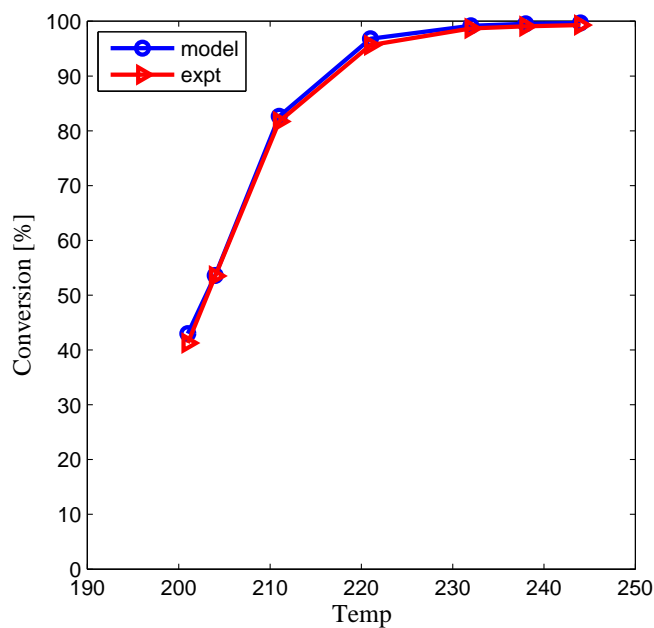
(b) C₃H₆

Figure. 3.14: Model validation with reactor data under simulated exhaust conditions at $60,000 \text{ h}^{-1}$ for DF and C₃H₆

the bench reactor. Since both the catalysts followed the same aging procedure, the same surface site density, a_j was used for model prediction with the engine data. Six sets of light-off curves, three with conventional combustion and three with PCI



(a) CO

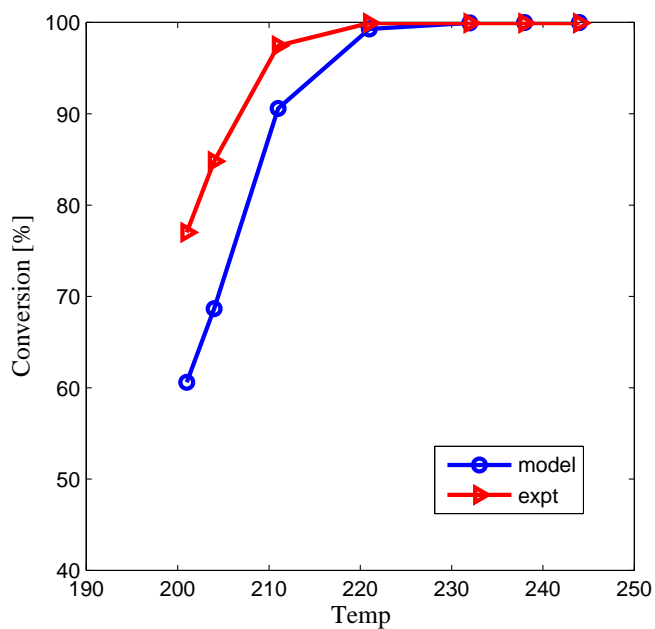
(b) H₂

Figure. 3.15: Model validation with reactor data under simulated exhaust conditions at $60,000 \text{ h}^{-1}$ for CO and H₂

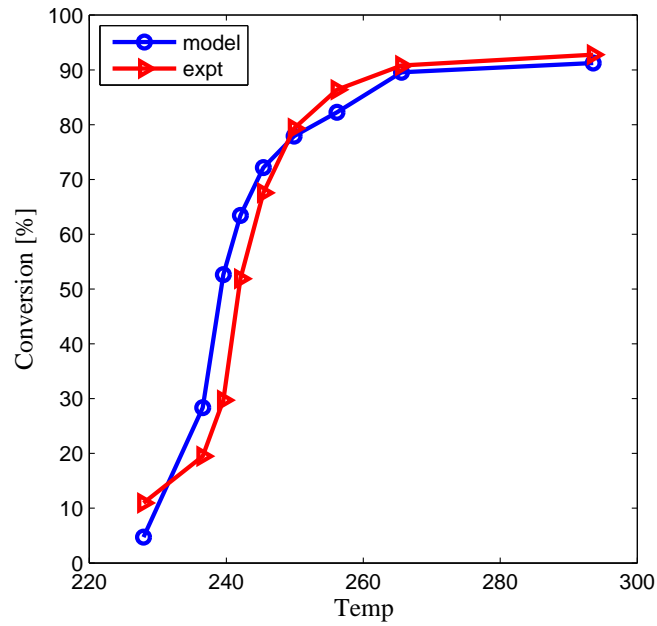
combustion were taken for validation purposes. The same model as the one used for the generation of the global rate expressions was for validation purposes. For these model calculations, rather than solving an energy balance equation, the temperature

field was estimated by linearly interpolating between the inlet and exit temperature measurements. While for brevity only one conventional and one PCI combustion case are shown here, these results are typical and other cases show similar agreement. Due to the lack of H_2 measuring capability with the engine, its validation is not presented here. For the case of NO, the $\Delta x_{g,NO}$ ($x_{g,NO}^{in} - x_{g,NO}^{out}$) was less than 10ppm and hence its validation with the engine was also not included.

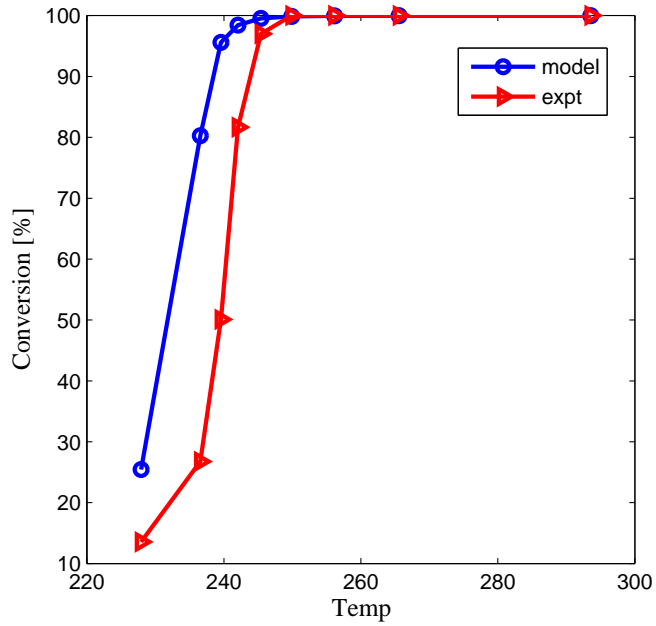
Figures (3.16(a)), (3.16(b)) show the comparison for a 2300 rpm conventional combustion case, and (3.17(a)), (3.17(b)) show the comparison for a 2300 rpm PCI combustion case. While engine measurements give a THC value for the inlet and conversion, the model needs individual inlets for DF and C_3H_6 . For all the comparisons presented here, it was assumed that 50% of the THC was unburnt DF and 50% was partially oxidized hydrocarbons, which in this work are represented by C_3H_6 . This value (50% DF + 50% C_3H_6) was chosen for simplicity. Experimentation with this ratio suggested that the model is weakly sensitive to this number and any value between 60-40 to 40-60 was a reasonable estimate.

3.5 Conclusions

Global oxidation reaction rates for diesel fuel (DF), propylene (C_3H_6), CO, H_2 and NO in the presence of excess oxygen were developed over the wide temperature and concentration ranges of practical interest. The total hydrocarbons in the diesel exhaust are categorized as DF, representing unburnt fuel, and C_3H_6 , representing the partially oxidized portion of the hydrocarbons. The concentration domain included exhaust which corresponds to both conventional and PCI combustion in the cylinder. A common NO inhibition term was used for all rates. An additional inhibition term, which was a function of CO, was found to be adequate for the ox-



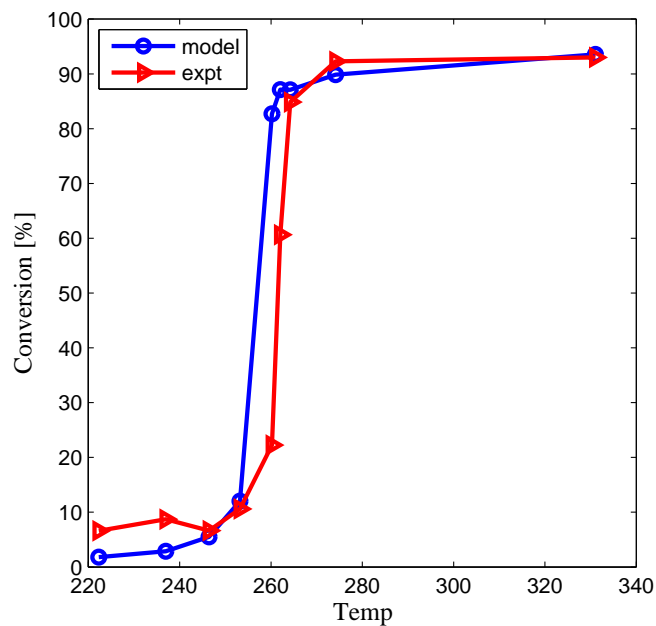
(a) THC



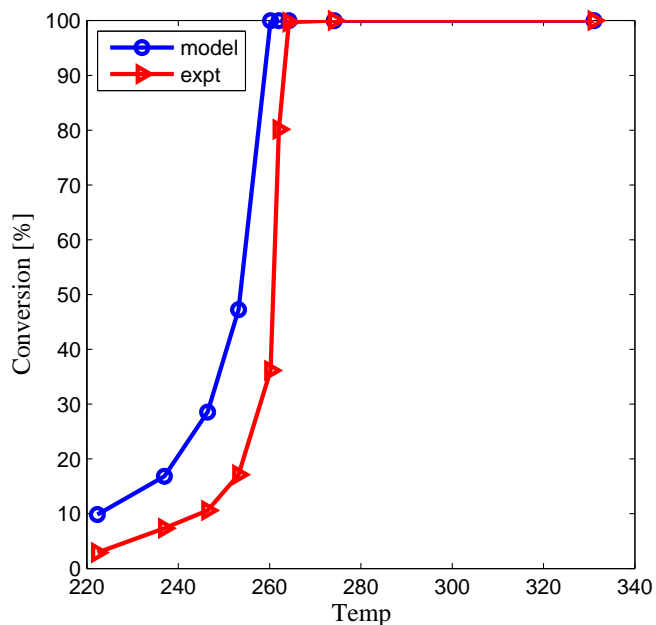
(b) CO

Figure. 3.16: Model validation with engine data obtained for 2300rpm with engine employing conventional combustion

validation of DF, C_3H_6 , CO and H_2 . For the NO oxidation, the additional inhibition was best represented by that induced by DF. The oxidation rates were developed using methodologies devised in chapter 2 [51]. This consisted of careful choice of



(a) THC



(b) CO

Figure. 3.17: Model validation with engine data obtained for 2300rpm with engine employing PCI combustion

the temperature and concentration domain, random sampling of data for reactor measurements, high space velocity capability reactor which can accurately conduct these measurements, optimization routines, reactor codes and finally an optimiza-

tion methodology to generate proper initial guesses and successively improve the rate forms. These rates were first validated against light-off curves generated by independent laboratory reactor experiments using realistic space velocities. The rates were further validated against actual engine data which was run both at conventional and PCI conditions. The kinetic models capture the full-scale DOC light-off curves well for a variety of testing conditions.

CHAPTER IV

Hydrocarbon storage modeling for diesel oxidation catalysts

This chapter discusses the development of a rate model that accurately captures the HC storage and release phenomenon on zeolites which are commonly used in DOCs. Experimental protocol and test matrices are detailed for the generation of this transient rate model. Simulations results are then presented from a full-scale 1D reactor model that incorporates oxidation kinetics from chapter 3 and the storage kinetics from the current chapter. A quantitative assessment on the need for a storage component in a DOC is explained.

4.1 Introduction

Reducing engine emissions resulting from cold start is a major impediment in meeting emissions standards. For late-model gasoline engines, nearly 60-70% of the total hydrocarbon (THC) emissions occur during cold start. In diesel engines, while the THC concentrations resulting from conventional combustion modes are low, advanced combustion strategies, such as pre-mixed compression ignition (PCI), which are being used to simultaneously reduce soot and NO_x , tend to produce significant

amounts of THC and CO. A diesel oxidation catalyst (DOC) which can oxidize all the THC and CO, is being proposed to meet the emissions standards in these scenarios. While such an oxidation catalyst is efficient in reducing THC and CO emissions after it is fully warmed-up, other strategies are being researched to address the cold start engine emissions.

Zeolites have proven to be effective in storing cold start hydrocarbons. Catalyzed hydrocarbon traps which contain an adsorbent material, such as zeolite, and noble metals are mixed in the same washcoat to provide both trapping and oxidation functions. The use of zeolites as efficient hydrocarbon trap systems to reduce cold-start hydrocarbon emissions has been well demonstrated for both gasoline [71] [72] [73] [74] and diesel [23] [24] [75] [76] applications. For diesel applications zeolite is typically part of the DOC which is used to oxidize CO and THC in the stream. This DOC will adsorb the hydrocarbons at low temperatures. As the temperature increases, hydrocarbons adsorbed on the zeolite desorb from the surface. However, if the noble metal becomes significantly active by this stage, the desorbed hydrocarbons are oxidized on the noble metals thus leading to near zero hydrocarbon emissions. CO is oxidized normally after catalyst light-off. Capturing THCs is more important since the CO oxidation occurs earlier compared to HC because the CO reaction rate is faster [52]. In cases where the desorption of hydrocarbons takes place before catalyst light-off, hydrocarbon slip is observed, which leads to undesired hydrocarbon emissions.

There are many different types of zeolites commercially available. The use of a particular type of zeolite is application specific. Classification of zeolite is commonly based on the Si/Al ratio. Two types of zeolites have been popular for automo-

tive applications namely, Y- and β -zeolites. These zeolites have 12 membered ring structures and larger pore sizes compared to other forms of zeolites. To differentiate between these two forms, the Y-zeolites commonly have a lower Si/Al ratio (1-25) and a smaller pore size. The β -zeolites have Si/Al ratios ranging between 10-100 and a larger pore size. There are obvious trade-offs between using these two types of zeolites. While smaller pores or a low pore volume may lead to pore blockage by coke and limit the diffusional transport of feed and product molecules, larger pores lead to lower surface area and consequently reduced catalytic contribution [77]. With respect to hydrocarbon adsorption, while Y-zeolite can adsorb straight chain hydrocarbons, β -zeolite can adsorb both straight and ring type hydrocarbons [78]. However, Y-zeolites are easier to produce and are known to have better performance characteristics with larger aliphatic hydrocarbons because of their higher bronsted acidity.

Equilibrium data for the adsorption-desorption reactions taking place in such systems have been successfully represented with Langmuir isotherms [79] [80] [81] [66]. Others in the literature have also used slightly more complicated representations such as the Freundlich isotherm to represent the equilibrium data [82]. For diesel adsorption-desorption modeling Tanaka *et al.* [67] used C_3H_6 as their representative hydrocarbons. Kryl *et al.* [66] used a combination of C_3H_6 , toluene (C_7H_8) and n-decane ($C_{10}H_{22}$) as representative hydrocarbons in diesel exhaust. They further assumed that C_3H_6 does not adsorb on the zeolite surface in the presence of larger hydrocarbons. This is a good assumption in the case of 3-D zeolites such as Y- or β -zeolites [83]. Their model however indicates that toluene and n-decane are adsorbed onto two independent zeolite sites. This has not been otherwise ob-

served in the literature. They also reported that both $C_{10}H_{22}$ and C_7H_8 have the same desorption activation energy and have nearly similar adsorption rate constants.

In the current work a simple storage-release model was developed for elucidating hydrocarbon storage on zeolites. This chapter starts by defining the experiments needed to generate adsorption and desorption rates, assuming that these are simple first-order processes on a single type of storage site, so as to obtain a Langmuir isotherm at equilibrium. Following the literature cited above, the HC content of the diesel exhaust is idealized with three representative hydrocarbons: propene (C_3H_6) as a partially oxidized HC, n-dodecane ($C_{12}H_{22}$) as a larger aliphatic HC, and toluene (C_7H_8) as an aromatic. C_3H_6 is not expected to adsorb, and preliminary testing showed no adsorption of toluene on catalyst sample used for this study. Therefore, transient experiments were conducted on a small scale reactor with n-dodecane ($C_{12}H_{22}$) representing adsorbable hydrocarbons. Total number of zeolite sites (N_{tot}), desorption activation energy (E_{des}) and the ratio of the adsorption and desorption pre-exponentials (A_{ads}/A_{des}) were determined based on equilibrium data. Then simple optimization techniques coupled with simplified reactor codes were used to estimate one of the pre-exponentials while other is inferred by their ratio. Once the adsorption-desorption kinetic parameters had been thus determined, this rate was incorporated into a full reactor model along with the oxidation rates developed in the previous chapter (also [52]) to understand the effect of various rates of heat-up the catalyst undergoes during start-up. This helped in assessing the effectiveness of the catalyst studied here in terms of reducing HC emissions due to HC storage, and in estimating the order of magnitude of the heat-up rate which would give improved performance due to the HC storage function.

Experimental

The hydrocarbon storage kinetics assumed here (i.e., Langmuir isotherm) allow the generation of the necessary adsorption-desorption rates with a minimum of four experiments for each hydrocarbon species involved in the system. The derivation of equations which leads to this conclusion are discussed in the ‘Modeling’ section. In this section the experimental procedures, choice of the HC species, temperature ranges considered and typical experimental results are discussed.

Test protocol

The experimental protocol should provide a means to infer the total number of moles of hydrocarbons that can be stored on a clean zeolite sample until equilibrium is reached. This equilibrium storage capacity is different from the total zeolite storage capacity and is a function of the hydrocarbon concentration and temperature of the system. The protocol should provide a means to validate the rate model thus developed, and should also include a procedure to clean the sample of any adsorbed hydrocarbons before attempting to run experiments on the same catalyst at a later stage.

All the experiments described in this section started with a clean zeolite sample. Each experiment was performed in three phases. In the first and second phases the temperature was held constant, and in the third phase the temperature was increased linearly with time at about 10°C/s. The inlet HC concentration was held constant during the first phase and then dropped to zero in the second and third

phases. Therefore, the first is an “adsorption phase”, in which the HCs adsorb on the zeolite surface until the outlet concentration reaches a constant value, that is, the equilibrium concentration for the given temperature. The second phase is then the “desorption phase” in which the negative concentration gradient between the surface and the gas phase HC concentrations cause the HCs to desorb from the zeolite surface. Rather than wait for the HC concentration at the outlet of the reactor to approach all the way to zero at the given temperature, this phase is ended when the outlet HC concentration shows a small gradient. Finally in the third phase a temperature programmed desorption (TPD) is performed to ensure that all the HCs are removed from the zeolite surface. These experiments are illustrated in figures 4.2(a), 4.2(b) and 4.3.

The adsorption phase data was utilized to develop the adsorption-desorption rate for the HC species under study. The desorption phase data was used to verify the reaction rate thus developed. While others in the literature have used the peak obtained during TPD for the calculation of desorption activation energy [67], this work did not use the same approach based on suggestions in de Jong *et al.* [84]. Minor temperature gradients were observed in the reactor during TPD which resulted from thermal inertia. Since the temperature in the reactor was not uniform, the TPD measurements were not used to estimate the activation energy for desorption. The third phase of the experiment is only used to clean the zeolite surface.

4.1.1 Test Matrix

With the test protocol defined, the HC species which will represent the potentially adsorbable components (on zeolite) of diesel exhaust need to be specified. Particular temperatures and HC concentrations which are to be used in the experiments should also be established.

The choice of the hydrocarbons for this study was based on the work described in chapter 3, where oxidation kinetics were developed for various species in diesel oxidation catalysts. These hydrocarbons were specified as partially oxidized hydrocarbons, represented by C_3H_6 , and unburnt fuel, represented by diesel fuel, and it was assumed that each of these components was $\sim 50\%$ of the THC_s on a molar C_3 basis. Here the unburnt fuel was further subdivided as a combination of n-dodecane ($C_{12}H_{24}$) and toluene (C_7H_8), again split equally for simplicity so that each of these components was 25% of the THC_s.

The test matrix consisting of two HC concentrations and two temperatures is given in table 4.1. From the earlier work it was expected that the maximum inlet THC_s concentration for a DOC would be around 2000 ppm on a C_3 basis, over the entire operating cycle. With the assumption that each potentially adsorbable representative HC (n-dodecane or toluene) might be 25% of the total, a reasonable concentration near the high end would be 340 ppm. The second concentration level chosen was half of this value. Note that these numbers will change when measured on an absolute scale, such as a C_{12} basis. The two temperatures, 116°C and 153°C, were chosen as representative of where adsorption and desorption would be significant, respectively. The lower temperature was also limited by the boiling points of

n-dodecane and toluene.

HC conc (ppm, C ₃)	Temperature (°C)
340 ppm	116
170 ppm	116
340 ppm	153
170 ppm	153

Table 4.1: Test matrix for generating a Langmuir isotherm

4.1.2 Reactor Set-up and Analysis

An 8g/ft³, 2:1 Pt:Pd/ γ -Al₂O₃ catalyst with zeolite was used for all the experiments. The monolith supported catalyst was hydro-thermally aged in a furnace at 650°C for 16 hours to account for de-greening of the noble metal and dealumination of the zeolite. A constant 2.2 L/min flow of 10% H₂O in air was fed to the furnace for the entire 16 hour aging period. The active site density (a_j) for the noble-metal was found to be 0.483 mole-site/m³ from CO chemisorption measurement, which corresponds to a dispersion of 26.1%. The description of the CO chemisorption method is given in chapter 2. The zeolite loading capacity was determined based on the Langmuir isotherm which is described in the next section.

The experimental set-up for this work is shown in figure 4.1. Other details of the reactor set-up are as follows:

- Monolith samples with thin washcoats (about 20 μ m) were used to minimize diffusion resistance within the washcoat.
- Experiments were carried out in a 2 inch OD stainless steel tubular reactor containing a sample which is 1.5 inch in diameter and 1.5 inch in length. Sam-

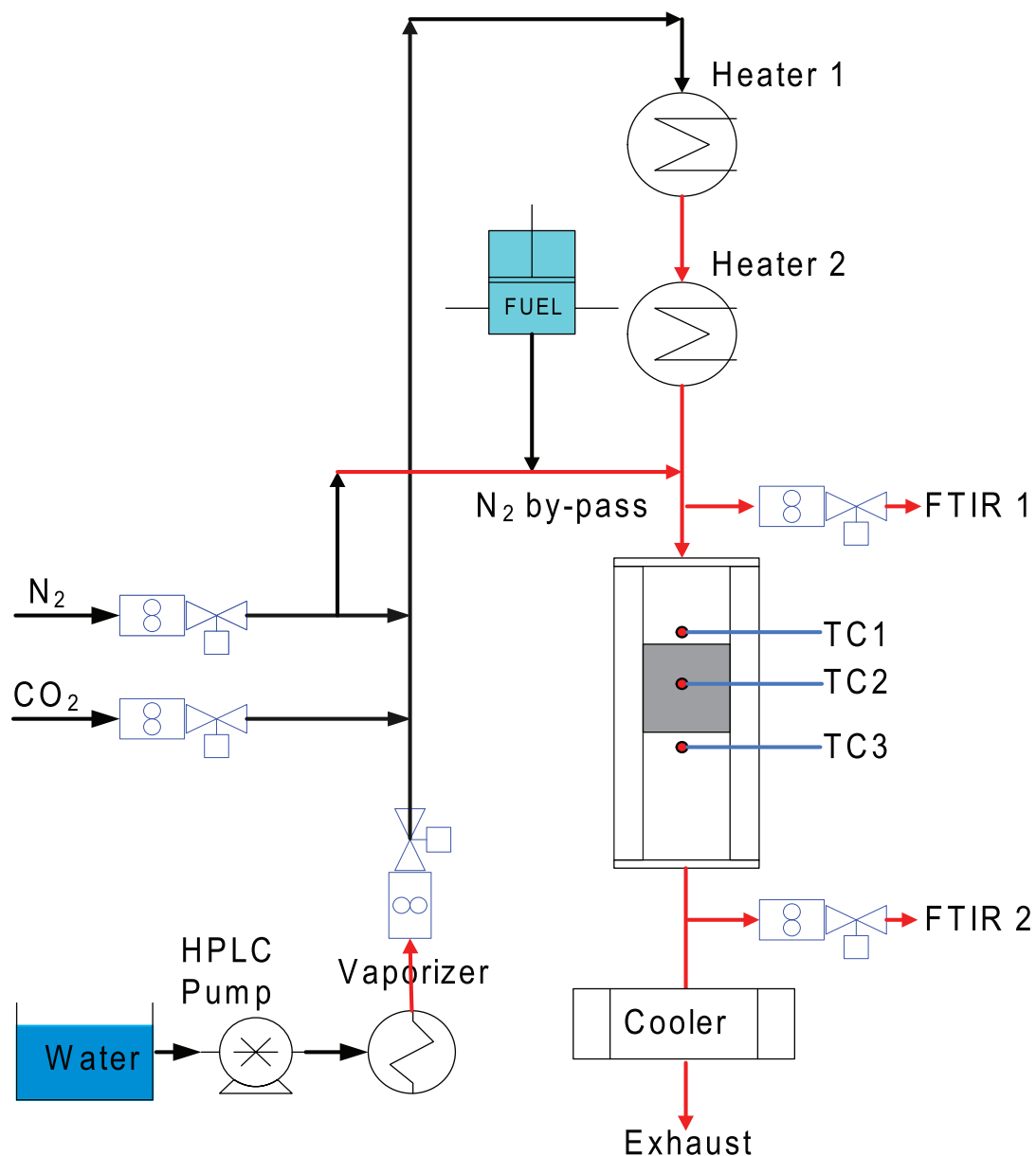


Figure. 4.1: Experimental set-up of the bench scale reactor for HC storage kinetics development

ples were held in place using a compressible ceramic paper wrap that prevented flow from bypassing the catalyst.

- The inlet gas contained 10% CO_2 , 8.7% H_2O and the remainder N_2 . Water was vaporized at $400^\circ C$ using a length of coiled 1/4 inch stainless steel tubing immersed in liquid tin. No O_2 was included to avoid interference of oxidation.

- A Cole-Parmer 74900-10 syringe pump was used to inject either dodecane or toluene into the system. The hydrocarbons were injected directly into a heated N_2 by-pass stream which helped vaporize and carry the fuel into the main flow. Since the mole-fraction of fuel after it enters the N_2 by-pass stream is very low (ppm level), the saturation temperature corresponding to its partial pressure is substantially lower than the temperatures of our experiments. Hence fuel condensation effects were not observed. The Fiberglass wick used for the work in chapter 3 to supply HCs was rejected for these transient experiments to decrease the response time for step changes in the HC concentration.
- Two inline heaters heated the inlet gas which in turn heated the catalyst. Reactor temperatures were monitored using three Type K thermocouples: one at the inlet, one at the outlet, and one inside the catalyst at the approximate axial midpoint.
- After the inline heaters, the heated feed stream was mixed with the HC/ N_2 mixture from the syringe pump. The complete inlet gas stream was then passed through a section of unheated silica mixing beads to attain the desired mixing and uniformity of the flow before entering the catalyst section.
- Two FTIRs were used to analyze the inlet and outlet gas simultaneously. MKS MultiGas 2030 process stream FTIRs were used to analyze n-dodecane ($C_{12}H_{26}$), toluene ($CH_3-C_6H_5$), H_2O or CO_2 . No measurable quantities of aldehydes, alcohols or CH_4 were detected during the experiments.
- All the experiments were at the slightly elevated pressure of 1.15 atm to ensure proper flow through both the FTIRs.
- All experiments were carried out at a space velocity of $35,281\text{ h}^{-1}$, which was

the actual space velocity as seen by the catalyst sample after subtracting the flow going through the inlet FTIR.

4.1.3 Typical Experimental Results

Figures 4.2(a) and 4.2(b) show typical results from the transient experiments conducted with dodecane and toluene. The temperatures measured by the upstream and downstream thermocouples are shown in figure 4.3. Note that during the adsorption and desorption phases the inlet temperature was held constant. After the desorption phase, the TPD continues until the HC concentration at the exit of the reactor is zero. For experimental purposes, 340 ppm on a C₃ basis was roughly estimated to be 100 ppm on a C₁₂ (dodecane) basis and 160 ppm on a C₇ (toluene) basis.

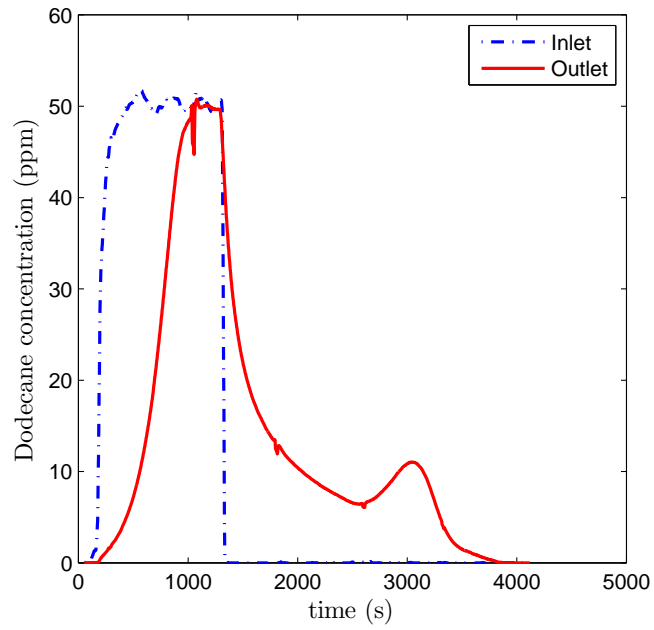
Based on the above plots it was concluded that n-dodecane exhibits storage behavior on the type of zeolite used for this study and that toluene does not. Therefore, the THCs in the exhaust are represented by C₃H₆, n-dodecane and toluene for purposes of modeling the HC oxidation and storage, with n-dodecane taken to be the only adsorbable hydrocarbon species on this zeolite.

4.2 Modeling

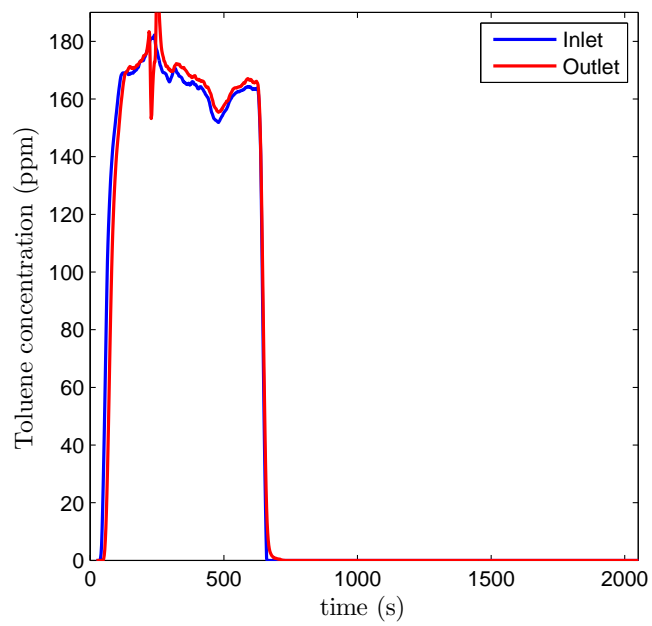
The adsorbable hydrocarbon species, which for this study was n-dodecane, are denoted by DF1. The storage-release reaction can then be written as,



Here Zeol refers to the zeolite sites which are not occupied by DF1, and DF1.Zeol represents the zeolite sites covered with hydrocarbons. In the discussion, the rate of the forward adsorption step, r_{ads} , and the reverse desorption step r_{des} are dis-



(a) Dodecane



(b) Toluene

Figure. 4.2: Typical adsorption/desorption experimental results for dodecane (a) and toluene (b)

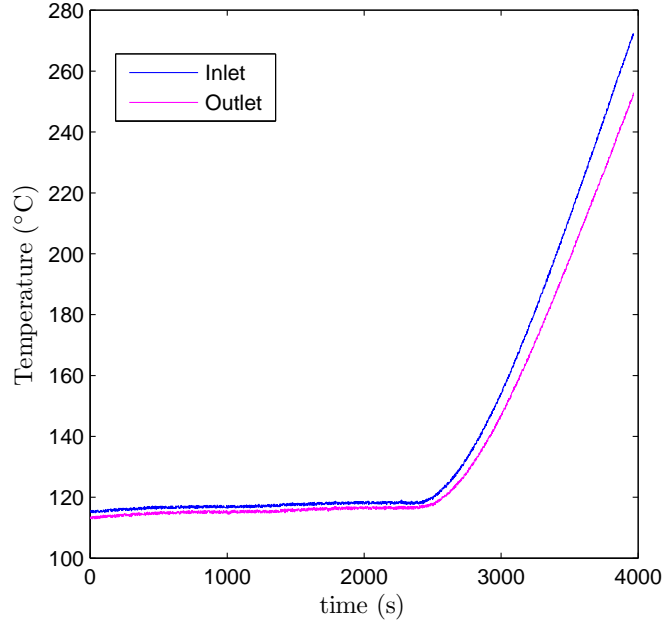


Figure. 4.3: Measured temperatures during the three phases of the experiment

cussed separately. It is commonly assumed that the adsorption rate constant is non-activated, but the desorption rate constant has Arrhenius dependence with temperature. Therefore a simple reaction rate model is proposed.

$$r_{ads} = A_{ads}c_{s,DF1}(N_{tot} - n_{DF1}) \quad (4.2.2)$$

$$r_{des} = A_{des}e^{-E_{des}/RT}n_{DF1} \quad (4.2.3)$$

The total storage capacity N_{tot} is not known *a priori* and can be estimated from a simple set of experiments as will be described in the following discussion.

It is useful to rewrite these rates in terms of the coverage θ_{DF1} , which refers to the fraction of the zeolite sites covered with HCs (that is, $\theta_{DF1} \equiv n_{DF1}/N_{tot}$).

$$r_{ads} = N_{tot}A_{ads}c_{s,DF1}(1 - \theta_{DF1}) \quad (4.2.4)$$

$$r_{des} = N_{tot}A_{des}e^{-E_{des}/RT}\theta_{DF1} \quad (4.2.5)$$

It is important to note that the adsorption rate is expressed as a function of the concentration (mol/m^3) rather than the mole-fraction of the HC species, DF1, to correctly capture the temperature dependence of this rate ($c = p/RT$).

From equation 4.2.2 and 4.2.3, it is clear that four constants, namely, A_{ads} , A_{des} , E_{des} and N_{tot} , are needed to define the adsorption and desorption rates. These constants are developed in the following discussion with the experimental data from the previous section. The ensuing discussion in this section is divided into three parts. The first part describes equilibrium calculations performed on the adsorption phase data from the four experiments described previously, to develop three of the four constants needed for the rates. The second part describes transient calculations which utilized a simplified transient reactor code integrated with optimization routines, to fit the adsorption phase data in order to generate the fourth constant. Finally, the desorption phase data was used to validate the rate model thus developed.

4.2.1 Equilibrium Calculations

At equilibrium, $r_{ads} = r_{des}$, so from equation 4.2.2 and 4.2.3,

$$A_{ads}c_{s,DF1}(N_{tot} - n_{eq,DF1}) = A_{des}e^{-E_{des}/RT}n_{eq,DF1}, \quad (4.2.6)$$

where $n_{eq,DF1}$ is the total number of moles of DF1 stored when the reactor reaches equilibrium. Re-arranging equation 4.2.6,

$$\frac{1}{n_{eq,DF1}} = \frac{1}{N_{tot}} + \frac{1}{K(T) * c_{s,DF1} * N_{tot}}, \quad (\text{Langmuir isotherm}) \quad (4.2.7)$$

where

$$K = \frac{A_{ads}}{A_{des}e^{-E_{des}/RT}}. \quad (4.2.8)$$

In the left-hand-side of equation 4.2.7, $n_{eq,DF1}$ can also be measured directly from the experiments by integrating the total measured HCs into the catalyst minus the total measured HCs coming out of the catalyst until equilibrium. That is,

$$n_{eq,DF1} = \int_0^{t_{eq}} (\dot{n}_{DF1,in} - \dot{n}_{DF1,out}) dt, \quad (4.2.9)$$

where t_{eq} is the time at which the outlet HC concentration is in equilibrium with the inlet concentration. Equation 4.2.7 is commonly referred to as the Langmuir isotherm. For a given temperature, it represents a line when $1/n_{eq,DF1}$ is plotted as a function of $1/c_{s,DF1}$. As there are no concentration gradients within the reactor at equilibrium, the inlet and outlet concentrations of n-dodecane indeed measure the concentration at the adsorber surface, $c_{s,DF1}$.

At a fixed temperature (e.g., one of the temperatures in the test matrix, table 4.1), two adsorption experiments at different HC concentrations, run all the way to equilibrium, will generate the two points that determine the line of the Langmuir isotherm. The slope and intercept of this line then determines the two coefficients in equation 4.2.7, essentially N_{tot} and K at this temperature. Repeating this at the second temperature, not necessarily with the same two HC concentrations, yields N_{tot} and K at this second temperature. Since N_{tot} is physically independent of temperature in the simplest case, the intercept of these two lines must be approximately the same, which is verified below with the data considered here. Then, K at two temperatures were used to generate an Arrhenius plot ($\log(K)$ vs. $1/T$), which yielded both the desorption activation energy and the ratio of the two pre-exponentials.

Langmuir Isotherm and Arrhenius Plot

Before attempting to use the four sets of adsorption phase data to generate the isotherm, two operations were performed to decrease the effects of noise in the experimental data upon subsequent calculations. First, after the target concentration was reached, the noisy inlet concentration was replaced with the constant target concentration. Second, during the initial period in which the concentrations rose rapidly to the target inlet concentration, all the experimental concentration data was smoothed with a 12-point moving average over the preceding 12 s of data.

The four sets of adsorption data, processed as above, were used to calculate the equilibrium molar capacities of n-dodecane, $n_{eq,DF1}$, from equation 4.2.9 and shown in table 4.2. Besides being converted from mole fractions, the concentrations shown

$n_{eq,DF1}$ (moles)	$c_{s,DF1}$ (C_{12} basis)	Temperature ($^{\circ}C$)
5.84×10^{-4}	3.5×10^{-3}	116
4.89×10^{-4}	1.8×10^{-3}	116
3.15×10^{-4}	2.9×10^{-3}	153
1.74×10^{-4}	1.4×10^{-3}	153

Table 4.2: $n_{eq,DF1}$ calculated for the experimental combinations of temperature and n-dodecane concentration. Concentrations were evaluated at the 1.15 atm of the experiments

here only approximate the intended values from table 4.1. These values resulted in the two Langmuir isotherms at 116 $^{\circ}C$ and 153 $^{\circ}C$ in figure 4.4. Because N_{tot} was assumed independent of temperature, the least squares fit for these lines was constrained to have a common intercept, but the high degree of consistency with the data provided credibility to this assumption. The results from this plot were used to calculate $N_{tot} = \mathbf{9.52} \times \mathbf{10}^{-4}$ mol for this sample of volume 45×10^{-6} m³.

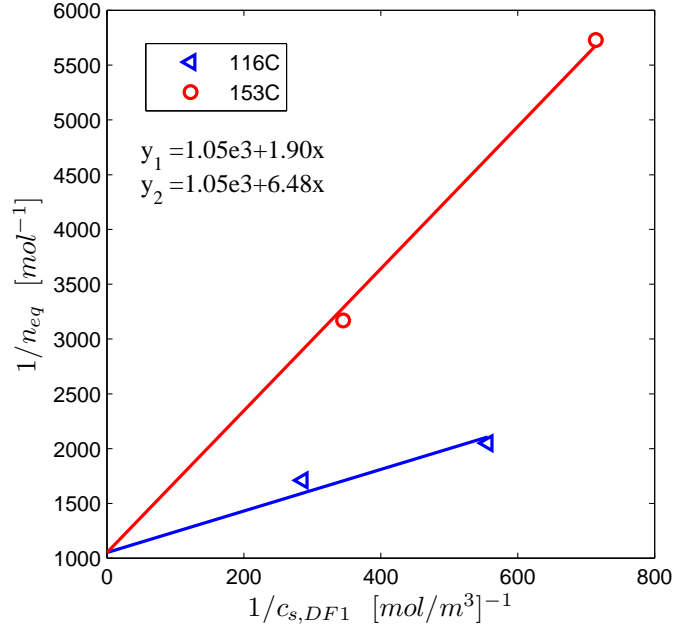


Figure. 4.4: Langmuir isotherms generated with the four concentration and two temperature combinations

Therefore the surface site density for zeolite, which was used to solve the species equations described in the next section, is given by $a_{ze} = \mathbf{21.2}$ mol/m³. From the slopes of the two lines, K at the two temperatures of 116°C and 153°C was **553** and **162** respectively. Figure 4.5 shows the Arrhenius plot generated by these two values of K , defined in equation 4.2.7. In the usual way, this yielded $E_{des} = \mathbf{4.56} \times 10^4$ J/mol and $A_{ads}/A_{des} = \mathbf{4.08} \times 10^{-4}$.

4.2.2 Transient Calculations

With N_{tot} , E_{des} and A_{ads}/A_{des} already known, estimating one of A_{ads} or A_{des} is enough to define all the constants. For the case described in this work, A_{ads} was chosen to be evaluated by fitting model predictions based on the above rate expressions to the experimental data.

The general method to generate reaction rate constants by matching experiments

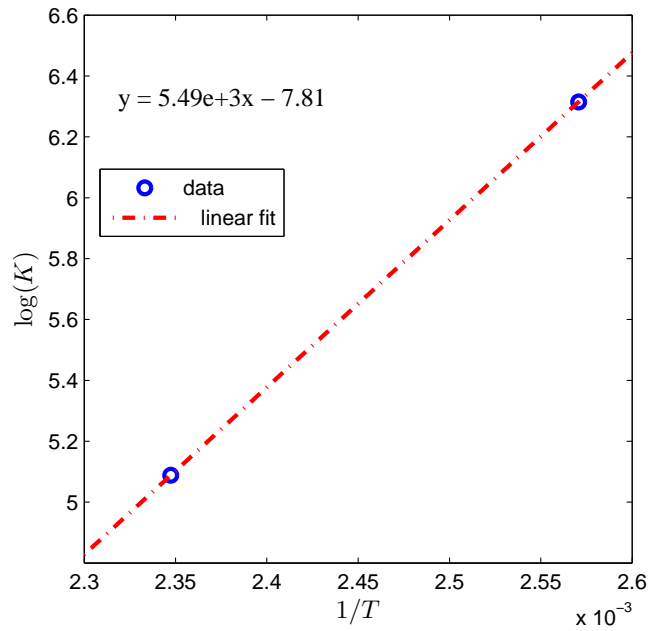


Figure. 4.5: Arrhenius plot of the ratio of rate constants

in this manner involves solving an outer problem and a corresponding inner problem. The outer problem is the optimization which minimizes the difference between the measured and calculated exit concentrations for all the tested conditions. The rate parameters are adjusted after every iteration to improve (decrease) the objective function, which measures how well the model predictions are in agreement with the experimental measurements. For each evaluation of the objective function we need solutions of a non-trivial inner problem where we predict the DF1 exit concentration as a function of time for each of the test conditions using the species conservation equations and the coverage equations. The objective function is then assembled as a weighted sum of the differences between measured and calculated exit DF1 concentrations.

Governing Equations of the Inner Problem

For the inner problem which solves for the species exit concentrations for given inlet conditions a simplified 1D reactor code was used. The basic assumptions of this model are as follows:

1. The temperature field was specified by linearly interpolating the two experimentally temperatures. No energy equation was solved.
2. The diffusion volume (used in the correlation determining the binary diffusion coefficient) of dodecane was assumed to be the same as that of diesel fuel as determined in chapter 3 [52].
3. No pore diffusion effects within the washcoat layer.
4. Transport properties of all species were calculated as though the bulk gas were N_2 .

In accepting the measured temperatures directly into the model in assumption 1, we are assuming mild temperature profiles within the reactor that can be well represented by a simple linear interpolant. This is justified since the adsorption and desorption phases are essentially isothermal, there is no local heat release from oxidation because oxygen was absent in all experiments, and the heat losses from our reactor are small. For assumption 2, dodecane, which is a long chain hydrocarbon, has nearly the same molecular weight as the molecular model for diesel fuel which was used in chapter 3. [52] (170 vs. 200). Since diffusion is largely dependent on the size of the molecule, the same diffusion volume was assumed. Other assumptions are fairly common in exhaust aftertreatment modeling and so their discussion is skipped.

Based on these assumptions the equations for the inner problem are given as follows:

$$\frac{w}{A} \frac{dx_{g,DF1}}{dz} = -k_{m,DF1} S(x_{g,DF1} - x_{s,DF1}) = a_{ze}(r_{des} - r_{ads}), \quad (4.2.10)$$

where

$$x_{s,DF1} = c_{s,DF1}/c \quad \text{and} \quad x_{g,DF1} = c_{g,DF1}/c \quad (4.2.11)$$

and,

$$\frac{d\theta_{DF1}}{dt} = A_{ads}c_{DF1}(1 - \theta_{DF1}) - A_{des}e^{-E_{des}/RT}\theta_{DF1} = r_{ads} - r_{des} \quad (4.2.12)$$

Note that a_{ze} is the surface site density of the adsorption-desorption reaction and was calculated by dividing N_{tot} by the volume of the reactor. The mass transfer coefficient is calculated based on the asymptotic Sherwood number and the binary diffusivity of individual trace HC within the mixture.

$$k_{m,DF1} = \frac{Sh}{D_h}(cD_{DF1,m}) \quad (4.2.13)$$

The binary diffusion coefficient for the trace species (hydrocarbon - DF1) is calculated based on the correlation given by Fuller *et al.* [62] as shown in equation 4.2.14 with the mixture approximated by N_2 .

$$cD_{DF1,m} = \frac{3.85 \times 10^{-5} T^{0.75} \sqrt{\frac{1}{M_{DF1}} + \frac{1}{M_{N_2}}}}{[\Sigma_{DF1}^{1/3} + \Sigma_{N_2}^{1/3}]^2} \quad (4.2.14)$$

Here M_{DF1} is 170 (g/mol), and Σ_{DF1} , which is the diffusion volume of DF1, is taken as 80 from [52].

The species equations were scaled according to the procedure described in our earlier work [51]. The coupled ODE in time (coverage equation) and DAE in space

(species equation) are solved using ‘ode15s’ (MATLAB) which is called recursively to solve both the time and space problem. Some minor modifications are made to ‘ode15s’ to improve the problem specific behavior.

Definition of Objective Function for the Outer Problem

The objective function for optimization defined below (equation 4.2.15) is based on the difference between the experimentally measured and model predicted DF1 exit concentration over the entire adsorption phase, i.e. until the outlet concentration reaches the equilibrium value. The summation over j refers to the four sets of experimental conditions listed in table 4.2.

$$\sqrt{\frac{1}{4} \sum_{j=1}^4 \int_0^{t_{eq}} \left(x_{g,DF1}^{expt-j}(L) - x_{g,DF1}^{model-j}(L) \right)^2 dt} \quad (4.2.15)$$

The optimization to generate the “best” value of A_{ads} was done using MATLAB’s ‘fmincon’, a constrained minimizer which uses local optimization methods.

Optimization Results

The value of the objective function at the end of the optimization was **86.5**. The final optimized value for A_{ads} was **13.5**. The value of A_{des} calculated based on the ratio of the pre-exponentials estimated from the Arrhenius plot was **3.31×10^4** . The results from the optimization are shown in figures 4.6(a)-4.6(d).

4.2.3 Validation

To validate the rate model developed in the previous sections, the model DF1 exit concentrations were compared with experimental DF1 exit concentrations over the entire desorption phase. Since the adsorption phase was used to estimate the reaction

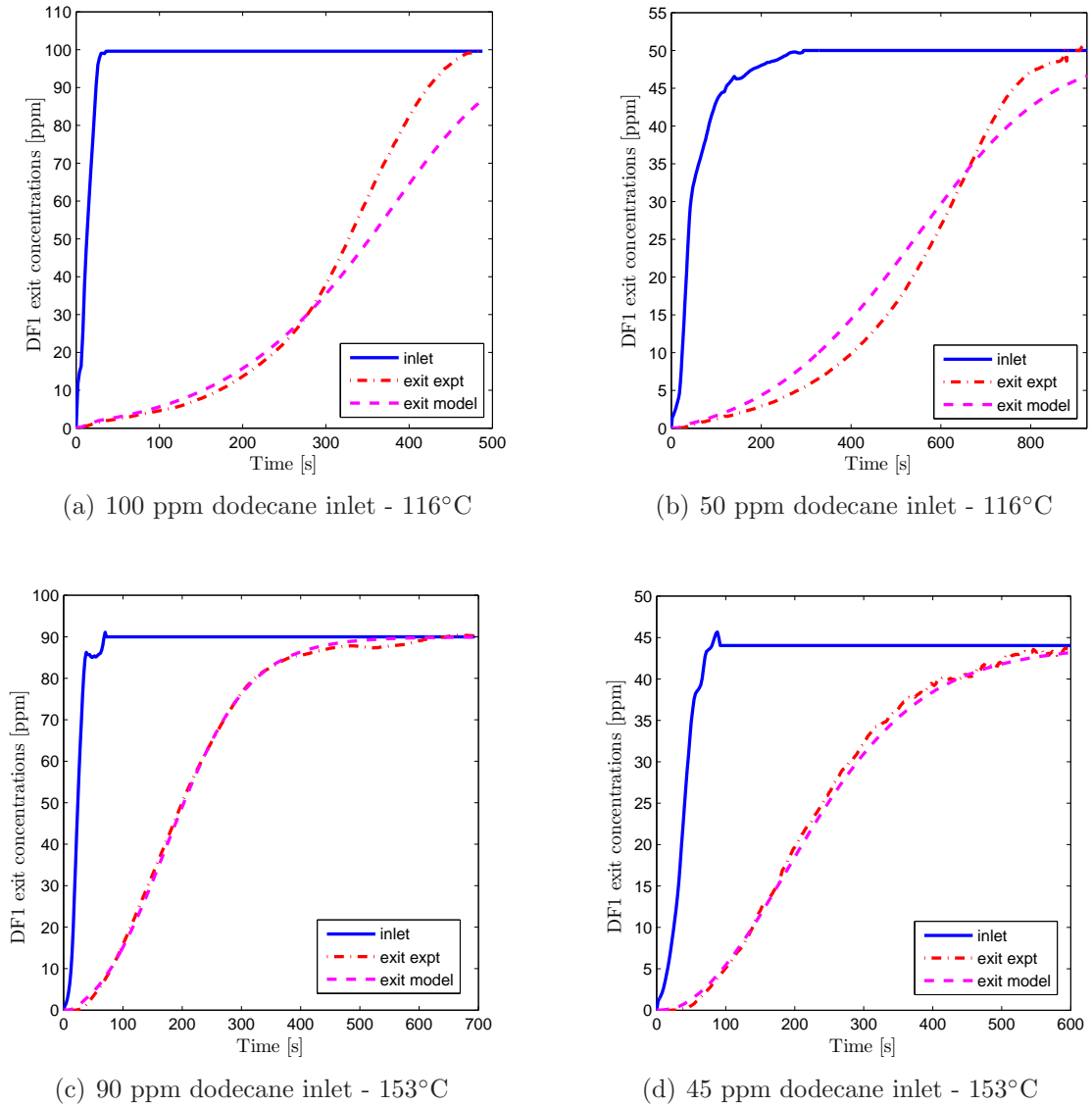
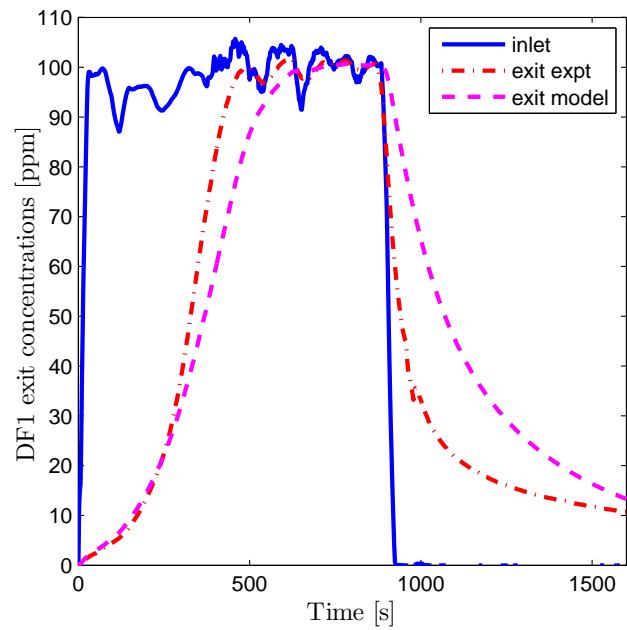


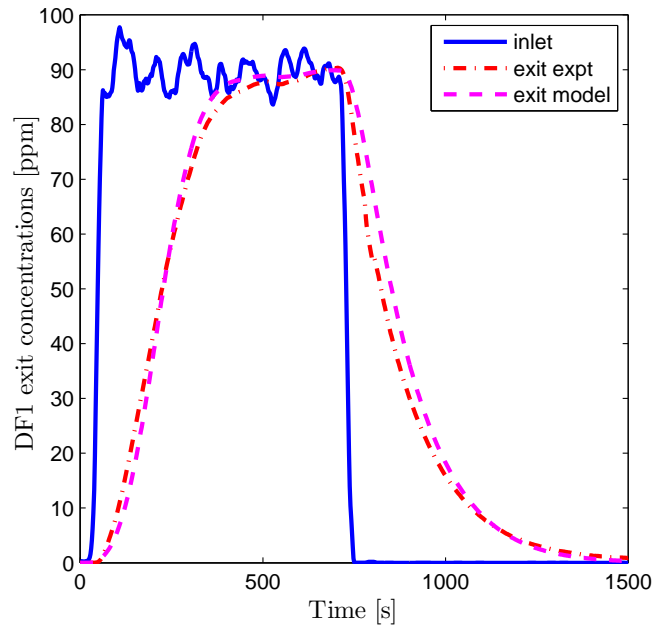
Figure. 4.6: Experimental results and model predictions during adsorption phase for the four test points at the optimized value of $A_{ads} = 13.5$. All concentrations are ppm dodecane on a C_{12} basis.

rate for adsorption and equilibrium calculations to determine the desorption rate, using the desorption phase data provides an independent means to check the desorption reaction rate. The two representative cases shown in figures 4.7(a)-4.7(b) show quite reasonable representation of the both the adsorption and desorption phases of the data. As the validation comparison is not particularly hindered by the presence of

experimental noise, these plots contain the fluctuations in inlet HC concentrations not present in figures 4.6(a)-4.6(d).



(a) 100 ppm dodecane inlet for adsorption phase - 116°C



(b) 90 ppm dodecane inlet for adsorption phase - 153°C

Figure. 4.7: Validation using desorption data. All concentrations are ppm dodecane on a C_{12} basis.

4.2.4 Full Scale 1D Adiabatic Reactor Model

The basic governing equations required to model both adsorption and oxidation are given below.

Solid phase energy which calculates for the surface temperature is given as:

$$\psi_s \frac{\partial T_s}{\partial t} = f_{sb} \lambda_{sb} \frac{\partial^2 T_s}{\partial z^2} + hS(T_g - T_s) - \sum_{j=1}^{nrct} a_j \Delta H_j r_j(T_s, \vec{c}_s, \vec{\theta}), \quad (4.2.16)$$

Here $nrct$ is the total number of reactions modeled for adsorption and oxidation. Conduction in the wash coat is neglected compared to that in the substrate. Monoliths which have very thin wash coats ($\sim 20\mu\text{m}$) are generally used to reduce pore diffusion. This assumption is hence very reasonable.

The effective heat capacity per unit volume of the reactor, ψ_s , is defined as:

$$\psi_s = \sum_{j=wb,wc} f_j \rho_{s,j} C_{ps,j} \quad (4.2.17)$$

Gas phase energy which solves for the gas phase temperature is described by:

$$\frac{w}{A} c_{pg} \frac{\partial T_g}{\partial z} = hS(T_s - T_g) \quad (4.2.18)$$

Trace species conservation are given as:

$$\frac{w}{A} \frac{\partial x_{g,i}}{\partial z} = -k_{mi} S(x_{g,i} - x_{s,i}) = \sum_{j=1}^{nrct} a_j s_{ij} r_j(T_s, \vec{c}_s, \vec{\theta}) \quad \text{for } i=1, \dots, nsp \quad (4.2.19)$$

where nsp includes all trace species modeled for adsorption and oxidation. This is equation 4.2.10 generalized to include the oxidation reactions and other oxidizing species.

The coverage of zeolite sites by DF1 is governed by:

$$\frac{d\theta_{DF1}}{dt} = A_{ads} c_{DF1} (1 - \theta_{DF1}) - A_{des} e^{-E_{des}/RT} \theta_{DF1} = r_{ads} - r_{des} \quad (4.2.20)$$

A more detailed description of the solution procedure for these equations is described elsewhere [85] and [86].

4.3 Results and Discussion

The intended function of a storage component such as zeolite in a DOC is to adsorb the hydrocarbons during early cold-start and then later release them after the noble metal is sufficiently warmed up to oxidize a substantial portion of the stored hydrocarbons. Adsorption and desorption are both occurring to some extent at all temperatures. However, since the desorption process is activated as compared to adsorption, desorption will become dominant as the reactor warms up, thereby releasing whatever hydrocarbons were stored at lower temperature when the desorption rate was small. The hope when introducing such storage devices is to oxidize the hydrocarbons immediately after there is net release from the adsorption sites, thereby minimizing early hydrocarbon emissions.

The value of adsorption-desorption kinetics comes after coupling with oxidation kinetics to accurately predict hydrocarbon emissions during cold-start. In this section, the adsorption/desorption kinetics are coupled with existing oxidation kinetics developed in the previous chapter to assess the advantage of having a storage component within a DOC. These kinetics are exercised with the “full adiabatic catalyst model” to assess the performance of a somewhat idealized but typical storage+oxidizer system. The basic governing equations used in the full model were given in the modeling section.

For the work in chapter 3, the total hydrocarbons in the exhaust were grouped

as diesel fuel, representing unburnt fuel component in the exhaust, and C_3H_6 , representing partially oxidized hydrocarbons in the exhaust. When validating model predictions with experiments using diesel engine exhaust, reasonable agreement was obtained when the THC from the engine were divided roughly equally, on a molar basis, between diesel fuel and C_3H_6 . For modeling purposes $C_{14.6}H_{24.8}$ was used to represent DF based on Heywood [68]. The molecular weight of this molecule is 200 (g/mol) and its diffusion volume which is used in the calculation of the binary diffusion coefficient is taken as 80.

By comparison, the adsorption/desorption rate developed here was for n-dodecane ($C_{12}H_{24}$) and not diesel fuel. However, it was noted earlier in the discussion that the difference in molecular weight is small and that the same diffusion volume was used for both the molecules. Also, toluene was found not to adsorb on the particular type of zeolite considered here. In other words, if the unburnt fuel is considered as some combination of long-chain and aromatic hydrocarbons, there should be a fraction of diesel fuel which does not adsorb on the zeolite. For simplicity this fraction is chosen to be 50% (All stated percentages for the THCs in this discussion should be interpreted as C_3 on a molar basis). In summary, to simulate diesel engine exhaust, the THCs are divided into three bins: 50% of the THC as C_3H_6 , 25% of the THC as DF1, which was considered as the adsorbable fraction of the unburnt fuel in the exhaust and, 25% of the THC as DF2, which was considered as the non-adsorbable fraction of the unburnt fuel in the exhaust. Both DF1 and DF2 were assumed to have the same oxidation rates (same oxidation rate as DF described in chapter 3); they only differ in their behavior towards storage on zeolite.

The following section begins with the study of a representative DOC which serves to demonstrate the value of the reactor model with both storage and oxidation kinetics combined, and also allows one to discern the specifics of the interaction between storage and oxidation that contribute to HC emissions during early warm-up. Of particular interest are the effects of different warm-up rates upon this representative catalyst. Finally, the effects of different heat-up rates on efficiency of this catalyst was demonstrated to assess its performance as a HC storage device.

4.3.1 A Representative Storage + Oxidation Catalyst

To make specific quantitative predictions with the reactor model, a representative DOC and somewhat idealized set of inlet conditions which describe exhaust warm-up were chosen. Catalyst dimensions used for this study are typical for a full scale DOC reactor in the exhaust of a 2L engine. The same catalyst specifications were used for all the parametric studies. The dimensions of the catalyst are given in table 4.3. To

L	0.2 m
A	$1.62 \times 10^{-2} \text{ m}^2$
cell density	400 cpsi
wsb	$1.65 \times 10^{-4} \text{ m}$
wwc	$3 \times 10^{-5} \text{ m}$
ρ_{sb}	$1.72 \times 10^3 \text{ kg/m}^3$
ρ_{wc}	$1.3 \times 10^3 \text{ kg/m}^3$
a_j (noble metal)	0.331 (mol-site/m ³)
a_j (Zeolite)	21.2 (mol-site/m ³)
\mathcal{W}	20 g/s

Table 4.3: Catalyst parameters for storage + oxidation studies

avoid attending to the details of an actual transient driving cycle, the reactor inlet

conditions during warm-up were idealized to a linearly increasing temperature with constant flow rate and species concentrations. For this study, the flow rate is given in table 4.3, and the typical inlet concentrations are given in table 4.4. These are

Species	Concentration
CO	1000 ppm
C ₃ H ₆	300 ppm
DF1 (adsorbable fuel)	25 ppm (C ₁₄ basis)
DF2 (non-adsorbable fuel)	25 ppm (C ₁₄ basis)
H ₂	200 ppm
NO	200 ppm
NO ₂	100 ppm
O ₂	10%
H ₂ O	8.7%
CO ₂	10%

Table 4.4: Species inlet concentrations for storage + oxidation studies

typical for a 2L engine during the cold start period of FTP operation. THC and CO emissions were chosen slightly on the higher side to critically evaluate the behavior of the DOC in effectively reducing these emissions. The temperatures are discussed below.

The transient nature of inlet gas during reactor warm-up was idealized as a steady ramp up to a constant. This allowed us to capture the single greatest factor driving the early stages of reactor warm-up with a single parameter, the temperature ramp rate. For each of the different ramp rates studied here, the inlet gas phase temperature was started from an ambient condition of 30°C and was linearly increased until it reached 240°C, where it is subsequently held constant. 240°C was chosen because the oxidation reactions studied here are significant by this temperature. After reach-

ing 240°C, the model was run at this temperature for 40 s to ensure that all reactions reached 100% conversion.

4.3.2 Effect of Heat-up Rate

10°C/min

Initially, a relatively slow ramp rate of 10°C/min was considered in order to easily see each stage of the adsorption/oxidation process. Figure 4.8 shows the DF1 (adsorbable hydrocarbon) concentration at the exit of the reactor plotted against time. For comparison the exit DF1 concentration that would result in the absence of a storage device is also shown. The following observations are made. Initially all the DF1 is adsorbed on the zeolite until about 600 s, when the inlet gas temperature reaches 130°C. After this, the catalyst starts net desorbing, leading to significant hydrocarbon emissions, until light-off of the oxidation reactions near 1100 s (214°C inlet gas), followed by zero DF1 emissions at later times.

To explain the various processes which occur in this system, a “rate plot” corresponding to this case (figure 4.9(a)) is proposed. The rate plot contains the cumulative oxidation rate and the net release rate (difference between desorption and adsorption rates) integrated over the entire reactor (“oxidation” in rate plot = $-\int_0^L r_{DF1} dz$ and “net release” in rate plot = $\int_0^L (r_{des} - r_{ads}) dz$). These spatial integrals provide a way to understand the gross behavior of the reactor at various times of its operation but do not provide any spatially resolved information. Referring these rates specifically to the DF1 concentration, the oxidation rate is shown here as negative since it depletes DF1 in the reactor. Similarly, net release produces DF1 in the reactor, so it is positive when desorption dominates and negative when adsorption dominates.

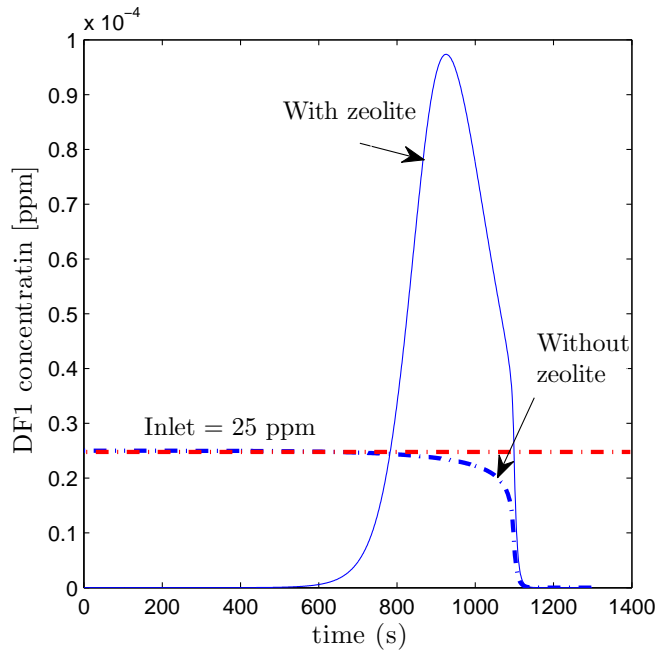


Figure. 4.8: DF1 emissions for a 10°C/min ramp rate

To aid the explanation of figure 4.9(a), axial profiles for the gas phase temperature, surface coverage of DF1 on zeolite and DF1 concentration profiles at specific times of interest are also plotted as figures 4.9(b), 4.9(c) and 4.9(d). For each time of interest, the behavior of the rate plot is explained by using these three auxiliary profile figures.

Details of the earliest phase, in which adsorption is dominant, are evident in the profiles at 400 s. Temperatures are too low for appreciable desorption or oxidation. The coverage profiles in figure 4.9(c) and the DF1 concentration profiles in figure 4.9(d) show that storage occurs first in the upstream portion of the reactor and that emissions of the adsorbable HCs represented by DF1 are zero.

At around 700 s, desorption, which is much more sensitive to temperature, begins to become significant as shown by the rapid increase in net release in figure 4.9(a). By 780 s, there is overall more DF1 desorbing and exiting the reactor than adsorbing,

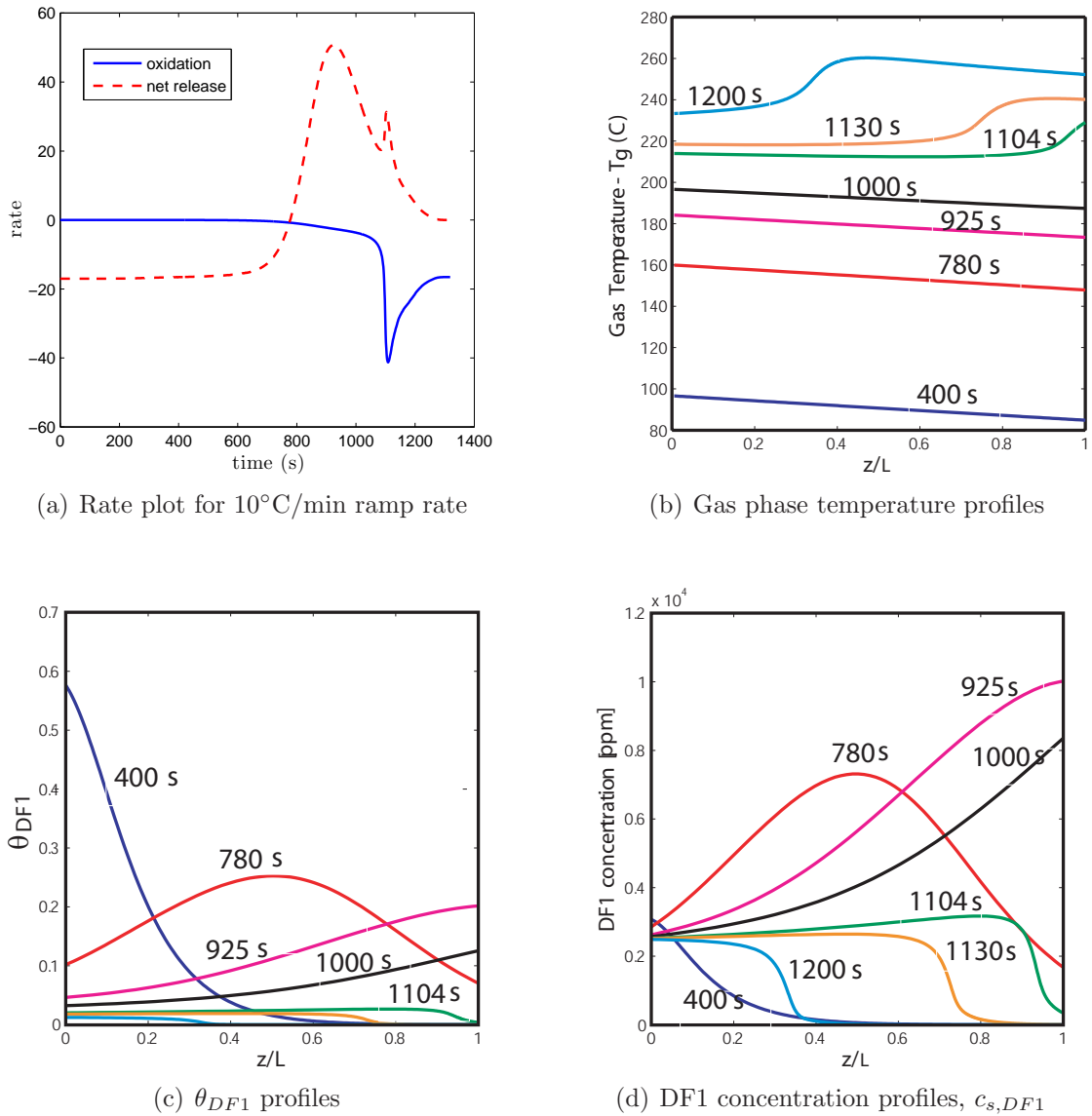


Figure. 4.9: Profiles at various times when the inlet gas phase temperature is ramped up at 10°C/min

since the net release switches to positive values then. The coverage profiles in figure 4.9(c) and the DF1 concentration profiles in figure 4.9(d) show that net desorption is occurring in about the first half of the reactor and net adsorption in the second half. By ~ 925 s, the net release in figure 4.9(a) reaches its maximum, marking the point where the coverages have fallen so low that they can no longer sustain their current level of overall net release. By 1000 s, coverages are small throughout the

reactor and still falling. HC oxidation rates have increased only slightly up to this point, and no significant exotherms are yet evident.

At 1104 s in figure 4.9(a), HC oxidation has just become very significant, and this time is very close to the sharp peaks in both rate curves. From figure 4.9(b), rapid oxidation has begun by this time, and all the profiles show that the reaction initiates at the downstream end of the reactor. The spatial gradients of both DF1 and CO (profile not shown) favor downstream light-off, while the small temperature gradient favors light-off upstream. Detailed comparison of conditions in the front and rear of the reactor at this time shows that the temperature has a very minor effect, with the CO gradient being the major factor. Because CO lights off slightly sooner than HCs, there is already a gradient in CO established by the time temperatures rise enough to initiate significant HC oxidation. The short second increase to a spike in net release near 1104 s is driven by the rapid oxidation of HCs. Specifically, while oxidation rapidly drives $c_{s,DF1}$ to zero at the exit, the adsorption rate, which is proportional to $c_{s,DF1}$, is temporarily more strongly affected than the desorption rate, which is proportional to θ_{DF1} . $c_{s,DF1}(z = L) = 0$ at the tip of this spike. At later times, oxidation is dominant and prevents any more DF1 from exiting the reactor, whether it comes from the inlet gas or is desorbed from the remainder stored on the zeolite, as the reaction front moves upstream through the reactor (e.g., 1130 s or 1200 s).

The following observations are made based on the above discussion. Substantial amount of DF1 emissions are observed for slow heat-up rates of the catalyst, such as the one discussed above. The net release curve shows two peaks for such cases: first corresponding to significant desorption and the second corresponding to

oxidation. Ideally the time between these peaks should be minimized because this is the period during which stored HCs are released without being oxidized. Second, this case exhibits “wrong way” behavior similar to a case noted by Oh *et al.* [63], where the local wall temperature at the downstream face rose above the inlet gas temperature. Oh *et al.* observed this effect during catalyst cool down when they stepped the gas phase inlet temperature down to room temperature with increased combustible species concentrations in the exhaust. In the case presented here this behavior is observed due to lower CO inhibition at the downstream end of the reactor.

4.3.3 Varying Heat-up Rates

In the initial case studied above, the slow ramp rate of 10 °C/min made it easier to distinguish the separate time intervals when adsorption, desorption, and oxidation were dominant. However, this separation of these phases also make a HC storage device rather ineffective in controlling HC emissions since, from figure 4.8 prior to light-off, most of the stored HC’s desorbed before they could be oxidized. To improve emissions performance of the DOC, it is clear that the oxidation peak must be moved earlier relative to the net release peak. In the setting of idealized inlet conditions we consider here, this is accomplished by increasing the temperature ramp rate, which is illustrated in figures 4.10(a) - 4.10(d) where we plot the rate plots for ramp rates of 10°C/min, 20°C/min, 40°C/min and 90°C/min in. At the highest ramp rate, the oxidation spike is even pushed slightly before the desorption peak.

Figure 4.11 shows the DF1 concentration exiting the reactor for the various ramp rates considered here. Cases with faster ramp rates show lower DF1 emissions. There

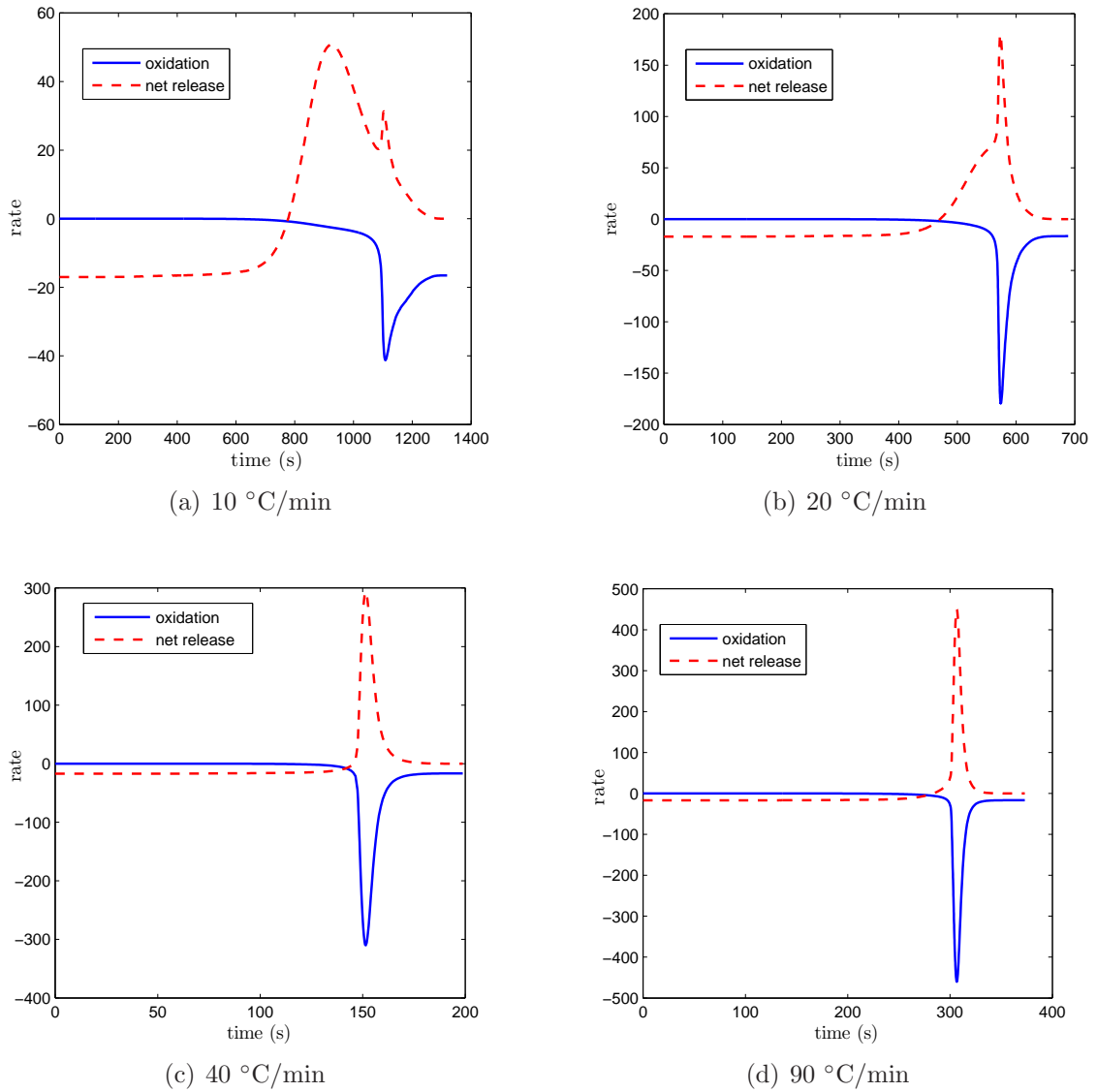


Figure. 4.10: Rate plots for varying ramp rates for inlet gas temperature

are at least 2 main factors to note that influence this conclusion. First, if a time to full light-off is defined as the time at which the exit DF1 concentration reaches zero, then cases with faster ramp rates will necessarily reach full light-off sooner and produce correspondingly less emissions. This effect is not related directly to HC storage. Second, even for times before full light-off, cases with higher ramp rates oxidize a larger fraction of their (lower) total incoming HC's because there is less time between the start of net desorption and the start of significant oxidation. As

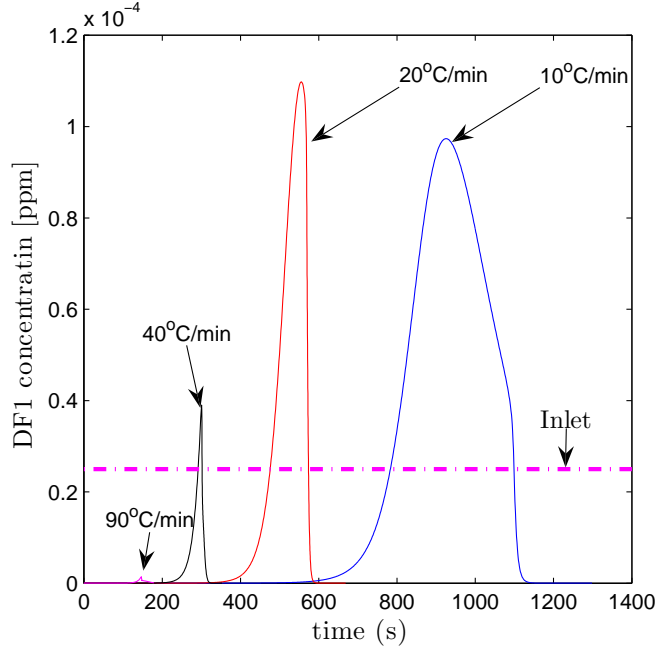


Figure. 4.11: DF1 (adsorbable hydrocarbon) emissions for varying ramp rates

a point of reference, FTP cycles for diesel engines produce heat-up rates of around 45-65°C/min depending upon the size of the engine. Therefore, for the particular catalyst and conditions studied here, good performance from the storage component of this DOC could be expected at practical warm-up rates. It is also important to realize that with the increase in the heat-up rate, the total amount of time available for adsorption also decreases, thus decreasing the coverage on the zeolite surface. For heat-up rates which give low DF1 emissions, it was observed that the coverage θ_{DF1} is very low ($\leq 10\%$), thus implying lower utilization of the storage component.

To quantify how well increasing the heat-up rate improves the performance of this adsorber+oxidizer system, and to understand the importance of the presence of the adsorber in a typical DOC, a parameter η is defined as follows:

$$\eta = \frac{\text{Cumulative DF1 emissions for an adsorber+oxidizer system}}{\text{Cumulative DF1 emission for an oxidizer system}} \quad (4.3.1)$$

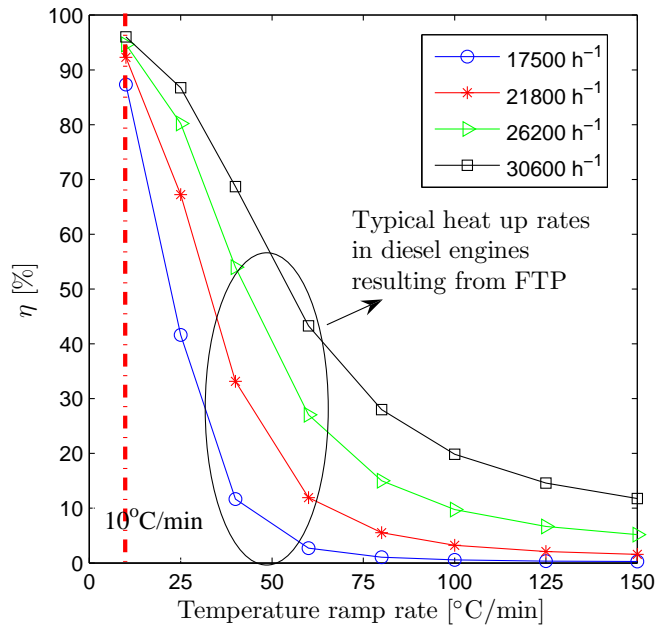


Figure. 4.12: η comparison for varying heat-up rates and space velocities

Thus $\eta = 1$ means that the adsorber is ineffective and has no effect on HC emissions. Lower values of η indicate increasing effectiveness.

A comparison of η values for various heat-up rates of the catalyst and a variety of typical total flow rates are plotted in figure 4.12. For each of these cases the inlet concentrations from table 4.4 were used for the predictions.

For any of these realistic flow rates, the figure expectedly shows poor performance at the lowest ramp rates and the best performance as the ramp rate approaches arbitrarily large values. Assuming η indeed is an appropriate measure of HC storage performance, the figures also show that the expected practical range of heat-up rates of 45-65°C/min is generally within the favorable intermediate performance interval. That is, the ramp rate is sufficiently high to give improved performance, but not too large so that the performance is insensitive to changes in the rate. As a point

of reference, the cases represented by figures 4.10(a) - 4.10(d) are also represented within the curve in figure 4.12 for the case where the flow rate is 20 g/s (17500 hr^{-1}). As may also have been somewhat evident from figures 4.10 and 4.11, increasing the heat-up rate beyond $40^\circ\text{C}/\text{min}$ at this flow rate would not give any substantial improvement in the HC storage performance as measured by η .

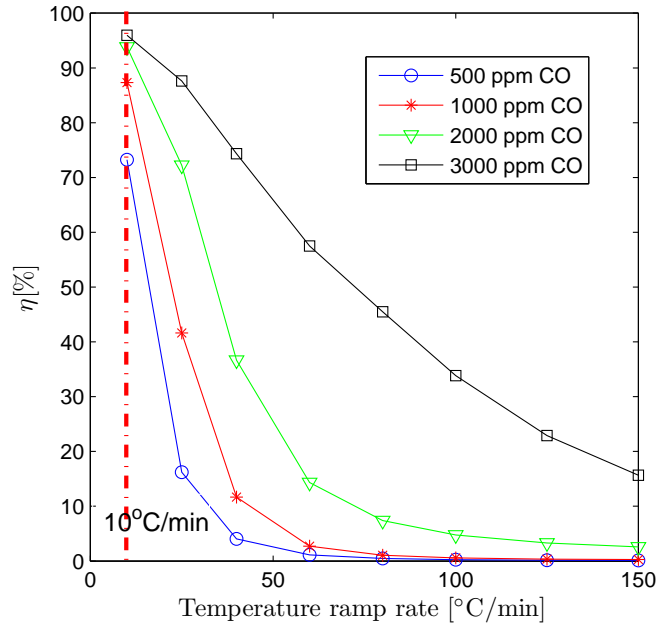


Figure. 4.13: η comparison for varying heat-up rates and CO concentrations

Figure 4.13 shows how the η varies with different heat-up rates and CO concentrations. Excluding very high concentrations of CO ~ 3000 ppm, which are possible during PCI (pre-mixed compression ignition) operation in diesel engines, all other CO concentrations show reasonably similar behavior in terms of their effect on η . Similar studies on NO concentration showed smaller effect of NO on η due to the fact that the range and magnitude of NO concentration is much smaller than that of CO during typical operation.

Summary

This work has two purposes. The principal purpose is to develop simple reaction rate expressions for adsorption and desorption of hydrocarbons on zeolites. Secondly, the need to exercise these adsorption kinetics with DOC oxidation kinetics developed previously to make some general, useful observations on the combined adsorber+oxidizer system. The conclusions for the first part of the work are as follows:

1. The reaction kinetics for hydrocarbon adsorption/desorption on zeolite can be adequately described by first order adsorption and desorption on a single site, including a Langmuir isotherm to represent equilibrium.
2. The diesel exhaust HC's were represented by a mixture of propylene (partially oxidized HC's from the engine), n-dodecane (aliphatic unburned fuel), and toluene (aromatic unburned fuel). Only n-dodecane adsorbed significantly on the zeolite studied here.
3. A minimum of **four** experiments were found to be sufficient to generate the necessary kinetic constants. Elementary analysis and direct measurements during adsorption yield the total zeolite storage capacity (N_{tot}), the activation energy for desorption (E_{des}) and the ratio of the pre-exponentials for adsorption and desorption. One of these pre-exponentials was then evaluated by fitting model predictions to the experimental adsorption data using a simplified 1D reactor code integrated within optimization routines in Matlab.
4. The resulting adsorption-desorption rate was validated with additional experimental data obtained during the later phases of the four tests.

The observations from exercising the adsorber+oxidizer model are as follows:

1. For the idealized warm-up conditions studied here, the HC's in the DOC light off from the downstream section of the catalyst. This is primarily because the CO starts reacting earlier, creating a gradient of CO, which then produces decreased inhibition of the HC oxidation at the rear.
2. The rate of heating of the inlet gas to the DOC plays an important role in determining overall system performance.
3. A "rate plot" was developed from the model predictions to separately reveal the rates of HC adsorption, desorption and oxidation while they are interacting during a typical warm-up. This plot clarifies the sequence of individual events that influence the performance of the zeolite in helping reduce HC emissions.
4. The zeolite studied here is reasonably effective in reducing exhaust hydrocarbon emissions. Specifically, for the exhaust conditions considered here (including realistic flow rates and inlet temperatures which increase at realistic rates of 45-65°C/min), storage on the zeolite reduced HC emissions during warm-up by at least a factor of 2 compared to cases with oxidation alone.

CHAPTER V

Conclusions and Future Work

5.1 Conclusions

This work reported the global oxidation and storage kinetics for DOCs. Oxidation kinetics were developed for hydrocarbons, CO, H₂ and NO for a Platinum and a commercially available DOC over wide concentration and temperature domain. A methodology was developed which could be used for the development of global rate models in general. Hydrocarbon storage kinetics were also developed for a zeolite catalyst that are commonly used in conjunction with the noble metals in a DOC. The oxidation and storage kinetics were integrated in a 1D adiabatic reactor model to study typical DOC performance under varying start-up conditions.

For the purpose of generating the specific global oxidation rate kinetics for a Pt DOC, a systematic methodology as described below was developed and implemented:

1. Careful choice of the concentration and temperature domain. Concentrations ranged between the typical inlet concentrations of the various species as seen at the inlet of a DOC and the very small concentrations (10's of ppm) expected near the rear of the reactor under conditions of high conversions.
2. Random and uniform sampling of test points within the domain.

3. Measurements of reactor conversions of aged samples at the chosen test points. Experiments were performed at high space velocities (up to 2 million hr^{-1}) to maintain modest temperature gradients and limit the range of local kinetic rates that occur along the length of the reactor for each test.
4. Development of a 1D reactor code coupling mass-transfer with reaction rates. Since the range of kinetic rates within the reactor for each test was, in general, too large for differential reactor operation, this was necessary to predict exit concentrations from our proposed reaction rate expressions. An experimentally measured temperature profile was used to allow the modeling of the system without solving for energy balance equations. This minimized the assumptions regarding the heat capacities and heat loss for the reactor.
5. Development of an objective function which is critically sensitive to differences between model predictions and experimental measurements at all conversion levels and which makes balanced and effective use of all the data.
6. A method to develop proper initial guesses that effectively exploit local optimization methods to determine the rate constants.
7. Modifying the rates, all of the Langmuir-Hinshelwood type, by successively and systematically adding or removing terms to arrive at the final expression. Re-optimization was performed at each step to ensure that the goodness of the fits was retained.
8. Final validation of the rate forms by comparing model predictions with light-off curves measured with a 1.7L Isuzu engine at University of Michigan.

The global rate expressions developed on the Pt DOC catalyst for the oxidation reac-

tions of C_3H_6 , CO, H_2 and NO provide reasonably good agreement with experimental data obtained over the wide concentration and temperature range. However, using only C_3H_6 to represent all the HCs in the diesel exhaust was found to be inadequate and a more complex HC representation was recommended.

For the purpose of generating specific oxidation kinetics for a commercial DOC, the systematic methodology developed previous was successfully used. The salient features of this work are as follows:

1. THCs in the diesel exhaust were speciated as C_3H_6 , representing the partially oxidized HCs in the exhaust and diesel fuel (DF), representing the unburnt fuel component in the diesel exhaust.
2. For experimental purposes Swedish low sulfur diesel fuel was used.
3. Rate models were incorporated in a converter model to validate the same against light-off curves generated from a small scale reactor with simulated diesel exhaust and realistic space velocities.
4. Finally, the rate models were validated with light-off curves generated using the 1.7L Isuzu diesel engine. Light-off curves were generated by using both conventional and PCI modes of combustion.

These rate models showed excellent agreement with the bench scale reactor data which was generated using simulated diesel exhaust, and with the engine data operated under both conventional and PCI combustion modes.

The HC storage work had two purposes. The principal purpose was to develop simple reaction rate expressions for accurately capturing the adsorption and desorp-

tion of hydrocarbons on zeolites. The second purpose was to exercise these storage kinetics with the previously developed DOC oxidation kinetics to make some general, useful observations on the combined adsorber+oxidizer system. The conclusions for the first part of the work are as follows:

1. The reaction kinetics for hydrocarbon adsorption/desorption on zeolite can be adequately described by first order adsorption and desorption on a single site, including a Langmuir isotherm to represent equilibrium.
2. For this work, diesel exhaust HC's were represented by a mixture of propylene (partially oxidized HC's from the engine), n-dodecane (aliphatic unburned fuel), and toluene (aromatic unburned fuel). Only n-dodecane was found to adsorb significantly on the zeolite studied here.
3. A minimum of **four** experiments were found to be sufficient to generate the necessary kinetic constants. Elementary analysis and direct measurements during adsorption yield the total zeolite storage capacity (N_{tot}), the activation energy for desorption (E_{des}) and the ratio of the pre-exponentials for adsorption and desorption. One of these pre-exponentials was then evaluated by fitting model predictions to the experimental adsorption data using a simplified 1D reactor code integrated within optimization routines in Matlab.
4. The resulting adsorption-desorption rate was validated with additional experimental data obtained during the later phases of the four tests.

The observations from exercising the adsorber+oxidizer model are as follows:

1. For the idealized warm-up conditions studied here, the HC's in the DOC light off from the downstream section of the catalyst. This is primarily because

the CO starts reacting earlier, creating a gradient of CO, which then produces decreased inhibition of the HC oxidation at the rear.

2. The rate of heating of the inlet gas to the DOC plays an important role in determining overall system performance.
3. A “rate plot” was developed from the model predictions to separately reveal the rates of HC adsorption, desorption and oxidation while they are interacting during a typical warm-up. This plot clarifies the sequence of individual events that influence the performance of the zeolite in helping reduce HC emissions.
4. The zeolite studied here was found to be reasonably effective in reducing exhaust hydrocarbon emissions. Specifically, for the exhaust conditions considered here (including realistic flow rates and inlet temperatures which increase at realistic rates of 45-65°C/min), storage on the zeolite reduced HC emissions during warm-up by at least a factor of 2 compared to cases with oxidation alone.

5.2 Thesis Contributions

The main contributions from this thesis are as follows:

1. A systematic methodology was defined that could be used for the development of steady global reaction kinetics in general. This methodology consisted of developing a procedure to generate a realistic concentration and temperature domain over which the rates are intended, an experimental set-up consisting of a bench scale integral reactor which was used to measure conversions of various species at the specific test conditions, a simplified 1D reactor model to calculate species exit concentrations, an objective function which critically evaluates

differences between model and experiments at all conversions, a method to generate initial guesses for optimization and finally validating the rate models with reactor and engine data.

2. Global oxidation kinetics that are valid over a wide concentration and temperature domain were generated for C_3H_6 , CO, H_2 , NO and NO_2 under lean conditions over a platinum DOC. Engine comparison indicated that C_3H_6 cannot be used to represent all the HCs in the diesel exhaust.
3. Global oxidation kinetics were developed for diesel fuel, C_3H_6 , CO, H_2 , NO and NO_2 under lean conditions over a commercial DOC. HCs in the diesel exhaust were speciated into two bins with C_3H_6 representing the partially oxidized component and diesel fuel representing the unburnt fuel component. These kinetics are valid for exhaust conditions which include both conventional and PCI combustion.
4. A methodology was proposed for generating transient kinetics which define the adsorption and desorption of HCs in zeolites. A quantitative assessment of the storage component in a DOC was presented which indicated that its presence reduces the overall HC emissions during typical start-up conditions by at least a factor of 2.

5.3 Recommendations for Future Work

Based on the work reported in this document, several potential future research areas have been identified. The current work could be used as a framework for all the following future developments.

1. The methodology developed and used for the generation of oxidation kinetics in

the DOC could be used for developing steady global reaction kinetics for chemical reactors which exhibit reasonably fast reaction rates such as the three way catalytic converter used for gasoline aftertreatment and auto-thermal reactor used for fuel processing applications.

2. Oxidation kinetics reported in chapter 3 were for a commercially available DOC which was intended primarily for removing the HCs and CO from the exhaust. As mentioned in the introduction section, the DOC could also be used as a heat source for DPF regeneration or LNT desulfation. Such a “heat-up” DOC would have a different noble metal composition, and the kinetics for the oxidation of various species would change considerably. Rather than using the methodology developed previously for developing kinetics for every DOC catalyst formulation, one could generate kinetics for two of the most representative DOC formulations and generate an interpolation strategy for the kinetics of any DOC formulation. For example, a 2:1 Pt/Pd catalyst is typically used for clean-up (removing HCs and CO from the exhaust) applications and a 1:2 Pt/Pd catalyst is typically employed for heat-up (e.g. regenerating DPF) purposes. Generating kinetics for these two formulations and generating a suitable interpolating strategy would be helpful in predicting kinetics for catalysts whose compositions are between the above two formulations (or are slight perturbations).
3. The methodology developed for HC storage-release study (experimental protocol and modeling framework) could be extended to study O₂ storage in gasoline three-way catalytic converters.

BIBLIOGRAPHY

BIBLIOGRAPHY

- [1] Krieger, R. B.; Siewert, R. M.; Pinson, J. A.; Gallopoulos, N. E.; Hilden, D. L.; Monroe, D. R.; Rask, R. B.; Solomon, A. S. P.; Zima, P.; Diesel Engines: One Option to Power Future Personal Transportation Vehicles, *SAE Paper 972683*, **1997**.
- [2] Kittelson, D. B.; Engines and Nanoparticles: A Review, *J. Aeros. Sci.*, vol. 29 (5-6), p-575, **1998**.
- [3] Seaton, A.; MacNee, W.; Donaldson, K.; Godden, D.; Particle Air Pollution and Acute Health Effects, *The Lancet*, vol. 345, p-176, **1995**.
- [4] Turns, S. R.; An Introduction to Combustion, Concepts and Applications, 2nd Edition, *McGraw-Hill*, **2000**.
- [5] Bernstein, J. A.; Alexis, N.; Barnes, C.; Bernstein, I. L.; Bernstein, J. A.; Nel, A.; Peden, D.; Diaz-Sanchez, D.; Tarlo, S.M.; Williams, P.B.; Health Effects of Air Pollution, *J. Allergy and Clinical Immunology*, vol. 114(5) , p-1116, **2004**.
- [6] Pourazar, J.; Diesel Exhaust Exposure Enhances the Expression of IL-13 in the Bronchial Epithelium of Healthy Subjects, *J. Resp. Med.*, vol. 98(9), p-821, **2004**.
- [7] Dieselnet Technology Guide, Emissions Standards, <http://www.dieselnet.com/standards>, **2007**.
- [8] Kamimoto, T.; Bae, M.; High Combustion Temperature for the Reduction of Particulate in Diesel Engines, *SAE 880423*, **1988**.
- [9] Jacobs, T. J.; Simultaneous Reduction in NO_x and Particulate Matter Emissions from a Light-Duty Diesel Engine Using Combustion Development and Diesel Oxidation Catalyst, *Dissertation, University of Michigan*, **2005**.
- [10] Okude, K.; Mori, K.; Shiino, S.; Moriya, T.; Premixed Compression Ignition (PCI) Combustion for Simultaneous Reduction of NO_x and Soot in Diesel Engine, *SAE*, 2004-01-1907, **2004**.
- [11] Herzog, P. L.; Bürgler, L.; Winklhofer, E.; Zelenka, P.; Cartellieri, W.; NO_x Reduction Strategies for DI Diesel Engines, *SAE 920470*, **1992**.

- [12] Epping, K.; Aceves, S.; Bechtold, R.; Dec, J.; The Potential of HCCI Combustion for High Efficiency and Low Emissions, *SAE* 2002-01-1923, **2002**.
- [13] Gary, A. W.; Yaacob, I. I.; Synthesis of PdO/CeO₂ Mixed Oxides Catalyst for Automotive Exhaust Emissions Control, *Catalysis Today*, vol. 96, p-165, **2004**.
- [14] Twigg, M. V.; Roles of Catalytic Oxidation in Control of Vehicle Exhaust Emissions, *Catalysis Today*, vol. 117, p-407, **2006**.
- [15] Liu, Z.; Woo, S. I.; Recent Advances in Catalytic DeNO_x Science and Technology, *Catalysis Reviews*, vol. 48, p-43, **2006**.
- [16] Burch, R.; Millington, P. J.; Walker, A. P.; Mechanism of the Selective Reduction of Nitrogen Monoxide on Platinum-based Catalysts in the Presence of excess Oxygen, vol. 4 (1), p-65, **1994**.
- [17] Held, W.; König, A.; Richter, T.; Puppe, L.; Catalytic NO_x Reduction in Net Oxidizing Exhaust Gas, *SAE* 900496, **1990**.
- [18] Taylor, K. C.; Schlatter, J. C.; Selective Reduction of Nitric Oxide Over Noble Metals, *Journal of Catalysis*, vol. 63, p-53, **1980**.
- [19] Shibata, J.; Takada, Y.; Shichi, A.; Satakawa, S.; Satsuma, A.; Hattori T.; Influence of Zeolite Support on Activity Enhancement by Addition of Hydrogen for SCR of NO by Propane over Ag-zeolites, *Applied Catalysis B.*, vol. 54, p-137, **2004**.
- [20] Blakeman, P. G.; Chiffey, A. F.; Phillips, P. R.; Twigg, M. V.; Walker, A. P.; Developments in Diesel Emission Aftertreatment Technology, *SAE*, 2003-01-3753, **2003**.
- [21] Khair, M.; A Review of Diesel Particulate Filter Technologies, *SAE*, 2003-01-2303, **2003**.
- [22] Theis, J. R.; Li, J. J.; Ura, J. A.; Hurley, R. G.; The Desulfation Characteristics of Lean NO_x Traps, *SAE*, 2002-01-0733, **2002**.
- [23] Kamijo, M.; Kamikubo, M.; Akama, H.; Matsushita, K.; Study of an Oxidation Catalyst System for Diesel Emission control Utilizing HC adsorption, *JSAE Review*, vol. 22, p-277, **2001**.
- [24] Adams, K. M.; Cavataio, J. V.; Sale, T.; Rimkus, W. A.; Hammerle, R. H.; Laboratory Screening of Diesel Oxidation Catalysts and Validation with Vehicle Testing: The Importance of Hydrocarbon Storage, *SAE*, 962049, **1996**.
- [25] Blackwood, A.; Tidmarsh, D.; Willcock, M.; The Effect of an Oxidation Catalyst on Cold Start Diesel Emissions in the First 120 Seconds of Running, *SAE*, 980193, **1998**.

- [26] Brisley, R. J.; Collins, N. R.; Law, D.; *European Patent Application 95308884*, **1995**.
- [27] Eastwood, P.; Critical Topics in Exhaust Gas Aftertreatment, *Research Studies Press Ltd.*, **2000**.
- [28] Heck, R. M.; Farrauto, R. J.; Automobile Exhaust Catalysts, *Applied Catalysis A.*, vol. 221, p-443, **2001**.
- [29] Phillips, P. R.; Chandler, G. R.; Jollie, D. M.; Wilkins, A. J. J.; Twigg, M. V.; Development of Advanced Diesel Oxidation Catalysts, *SAE 1999-01-3075*, **1999**.
- [30] Farrauto, R. J.; Voss, K. E.; Monolith Diesel Oxidation Catalysts, *Applied Catalysis B.*, vol. 10, p-29, **1996**.
- [31] Verdier, S.; Innovative Materials for Diesel Oxidation Catalysts with High Durability and Early Light-off, *SAE*, 2005-01-0476, **2005**.
- [32] Tashiro, K.; Ito, S.; Oba, A.; Yokomizo, T.; Development of Oxidation Catalyst for Diesel Passenger Car, *JSAE Review*, vol. 16, p-131, **1995**.
- [33] Voss, K.; Yavuz, B.; Hirt, C.; Farrauto, R.; Performance Characteristics of a Novel Diesel Oxidation Catalyst, *SAE*, 940239, **1994**.
- [34] Morlang, A.; Neuhausen, U.; Klementiev, K. V.; Schütze, F. -W.; Mieke, G.; Fuess, H.; Lox, E. S.; Bimetallic Pt/Pd Diesel Oxidation Catalysts Structural Characterisation and Catalytic Behavior, *Applied Catalysis B.*, vol. 60, p-191, **2005**.
- [35] Yao, H. C.; Yu Yao, Y. F.; Ceria in Automotive Exhaust Catalysts, *Journal of Catalysis*, vol. 86, p-718, **1984**.
- [36] Bera, P.; Patil, K. C.; Jayaram, V.; Subbanna, G. N.; Hegde, M. S.; Ionic Dispersion of Pt and Pd on CeO₂ by Combustion Method: Effect of Metal - Ceria Interaction on Catalytic Activities for NO Reduction and CO and Hydrocarbon Oxidation, *Journal of Catalysis*, vol. 196, p-293, **2000**.
- [37] Summers, J. C.; Ausen, S. A.; Interaction of Cerium Oxide with Noble Metals, *Journal of Catalysis*, vol. 58, p-131, **1979**.
- [38] Heck, R. H.; Wei, J.; Katzer, J. R.; Mathematical Modeling of Monolith Catalysts, *AIChE Journal*, vol. 22(3), p-177, **1976**.
- [39] Hoebink, J. H. B. J.; Harmsen, J. M. A.; Scholz, C. M. L.; Marin, G. B.; Schouten, J. C.; Structured Catalysts and Reactors, *Chapter 9 - Modeling of automotive exhaust gas converters*, ISBN 0-8247-2343-0, **2005**.
- [40] Hayes, R. E.; Kolaczkowski, S. T.; Mass and Heat Transfer Effects in Catalytic Monolith Reactors, *Chemical Engineering Science*, vol. 49(21), p-3587, **1994**.

- [41] Young, L. C.; Finlayson, B. A.; Mathematical Models of the Monolith Catalytic Converter: Part I and II, *AIChE Journal*, vol. 22(2), p-331, **1976**.
- [42] Dumesic, J. A.; Rudd, D. F.; Aparicio, L. M.; Rekoske, J. E.; Treviño, A. A.; The Microkinetics of Heterogeneous Catalysis, *ACS professional reference book*, American Chemical Society: Washington, DC, **1993**.
- [43] Knox, D.; Dadyburjor, D. B.; Bounds for Acceptable Values of Adsorption Entropy, *Chemical Engineering Communication*, vol. 11, p-99, **1981**.
- [44] Boudart, M.; Djéga-Mariadassou, G.; Kinetics of Heterogeneous Catalytic Reactions, *Princeton University Press*, Princeton, NJ, **1984**.
- [45] Fogler, S., H.; Elements of Chemical Reaction Engineering, *Prentice-Hall International Series in Physical and Chemical Engineering*, ISBN 0130473944, **2005**.
- [46] Koltsakis, G. C.; Konstantinidis, P. A.; Stamatelos, A. M.; Development and Application Range of Mathematical Models for 3-way Catalytic Converters, *Applied Catalysis B.*, vol. 12, p-161, **1997**.
- [47] Montreuil, C. N.; Scott, C. W.; Andrew, A. A.; Modeling Current Generation Catalytic Converters: Laboratory Experiments and Kinetic Parameter Optimization - Steady State Kinetics, *SAE 920096*, **1992**.
- [48] Pattas, K. N.; Stamatelos, A. M.; Pistikopoulous, P. K.; Koltsakis, G. C.; Konstantinidis, P. A.; Volpi, E.; Leveroni, E.; Transient Modeling of 3-way Catalytic Converter, *SAE 940934*, **1994**.
- [49] Shamim, T.; Shen, H.; Sengupta, S.; Son, S.; Adamczyk, A. A.; A Comprehensive Model to Predict Three Way Catalytic Converter Performance, *Journal of Engineering for Gas Turbines and Power, Transactions. ASME* vol. 124, p-421, **2002**.
- [50] Koltsakis, G. C.; Kandylas, I. P.; Stamatelos, A. M.; Three Way Catalytic Converter Modeling and Applications, *Chemical Engineering Communications*, vol. 164, p-153, **1998**.
- [51] Sampara, C.S.; Bissett, E. J.; Chmielewski M.; Global Kinetics for Platinum Diesel Oxidation Catalysts, *Industrial and Engineering Chemistry Research*, vol. 46 (24), p-7993, **2007**.
- [52] Sampara, C. S.; Bissett, E. J.; Chmielewski, M.; Global Kinetics for a Commercial Diesel Oxidation Catalyst with Two Exhaust Hydrocarbons, *Industrial and Engineering Chemistry Research*, vol. 47 (2), p-311, **2008**.
- [53] Sampara, C. S.; Bissett, E. J.; Assanis, D.; Hydrocarbon Storage Modeling for Diesel Oxidation Catalysts, *Submitted to Chemical Engineering Science*, **2008**.

- [54] Voltz, S. E.; Morgan, C. R.; Liederman, D.; Jacob, S. M.; Kinetic Study of Carbon Monoxide and Propylene Oxidation on Platinum Catalysts, *Industrial and Engineering Chemistry Product Research and Development*, vol. 12(4), p-294, **1973**.
- [55] Yung-Fang Yu Yao, The Oxidation of CO and Hydrocarbons Over Noble Metal Catalysts, *Journal of Catalysis*, vol. 87, p-152, **1984**.
- [56] Morooka, Y.; Ozaki, A.; Regularities in catalytic properties of metal oxides in propylene oxidation, *Journal of Catalysis*, vol. 5, p-116, **1966**.
- [57] Yentekakis, I. V.; Tellou, V.; Botzoulaki, G.; Rapakousios, I. A.; A Comparative Study of the $C_3H_6+NO+O_2$, $C_3H_6+O_2$ and $NO+O_2$ Reactions in Excess Oxygen Over Na-Modified Pt/ γ - Al_2O_3 Catalysts, *Applied Catalysis B.*, vol. 56, p-229, **2005**.
- [58] Olsson, L.; Persson, H.; Fridell, E.; Skoglundh, M.; Andersson, B.; A Kinetic Study of NO Oxidation and NO_x Storage on Pt/ Al_2O_3 and Pt/BaO/ Al_2O_3 , *Journal of Physical Chemistry B.*, vol. 105, p-6895, **2001**.
- [59] Després, J.; Elsener, M.; Koebel, M.; Kröcher, O.; Schnyder, B.; Wokaun, A.; Catalytic Oxidation of Nitrogen Monoxide Over Pt/ SiO_2 , *Applied Catalysis B.*, vol. 50, p-73, **2004**.
- [60] Majewski, A. W.; Ambs, J. L.; Bickel, K.; Nitrogen Oxides Reactions in Diesel Oxidation Catalysts, *SAE*, 950374, **1995**.
- [61] Bissett, E. J.; Oh, S. H.; Sinkevitch, R. M.; Pt Surface Kinetics for a PrOx Reactor for Fuel Cell Feed Stream Processing, *Chemical Engineering Science*, vol. 60, p-4709, **2005**.
- [62] Fuller, E. N.; Schettler, P. D.; Giddings, C. J.; A New Method for Prediction of Binary Gas-Phase Diffusion Coefficients, *Industrial and Engineering Chemistry*, vol. 58(5), p-19, **1966**.
- [63] Oh, S. H.; Cavendish, J. C.; Transients of Monolith Catalytic Converters: Response to Step Changes in Feedstream Temperature as Related to Controlling Automobile Emissions, *Industrial and Engineering Chemistry Product Research and Development*, vol. 21, p-29, **1982**.
- [64] Knafl, A.; Busch, S. B.; Han, M.; Bohac, S. V.; Assanis, D. N.; Szymkowicz, P. G.; Blint, R. D.; Characterizing Light-off Behavior and Species-Resolved Conversion Efficiencies During *in-situ* Diesel Oxidation Catalyst Degreening, *SAE*, 2006-01-0209, **2006**.
- [65] Bohac S. V.; Han M.; Jacobs T. J.; López A. J.; Assanis D.N.; Szymkowicz P. G.; Speciated hydrocarbon emissions from an automotive diesel engine and DOC utilizing conventional and PCI combustion, *SAE*, 2006-01-0201; **2006**.

- [66] Kryl D.; Kočí P.; Kubíček M.; Marek M.; Maunula T.; Härkönen M.; Catalytic Converters for Automotive Diesel Engines with Adsorption of Hydrocarbons on Zeolites, *Industrial and Engineering Chemistry Research*, vol. 44, p-9524, **2005**.
- [67] Tanaka Y.; Hihara T.; Nagata M.; Azuma N.; Ueno A.; Modeling of Diesel Oxidation Catalyst, *Industrial and Engineering Chemistry Research*, vol. 44, p-8205, **2005**.
- [68] Heywood J. B.; Internal Combustion Engine Fundamentals, *McGraw-Hill international editions*, ISBN: 0-07-100499-8, **1988**.
- [69] Han, M.; Hydrocarbon Emission Profiles from Advanced Diesel Combustion Using Gas Chromatography and Novel Heat-up Diesel Oxidation Catalyst Development, *Ph.D. Dissertation*, University of Michigan, **2007**.
- [70] Poling B. E.; Prausnitz J. M.; O'Connell J. P.; The Properties of Gases and Liquids, *McGraw-Hill*, ISBN:0-07-011682-2, **2000**.
- [71] Mitsuishi, S.; Mori, K.; Nishizawa, K.; Yamamoto, S.; Emission Reduction Technologies for Turbocharged Engines, *SAE*, 1999-01-3629, **1999**.
- [72] Yamamoto, S.; Matsushita, K.; Etoh S.; Takaya, M.; In-line Hydrocarbon (HC) Adsorber System for Reducing Cold-Start Emissions, *SAE*, 2000-01-0892, **2000**.
- [73] Nishizawa, K.; Momoshima, S.; Koga, M.; Nissan's Gasoline SULEV Technology, *SAE*, 2000-01-1583, **2000**.
- [74] Kanazawa, T.; Development of Hydrocarbon Adsorbents, Oxygen Storage Materials for Three-Way Catalysts and NO_x Storage-Reduction Catalyst, *Catalysis Today*, vol. 96, p-171, **2004**.
- [75] Banno, Y.; Hihara, T.; Nagata, M.; Tanaka, Y.; Pre-Filter Diesel Oxidation Catalyst Development for DOC-CSF System, *SAE*, 2004-01-1427, **2004**.
- [76] Lafyatis, D. S.; Ansell, G. P.; Bennett, S. C.; Frost, J. C.; Millington, P. J.; Rajaram, R. R.; Walker, A. P.; Ballinger, T. H.; Ambient Temperature Light-off for Automobile Emission Control, *Applied Catalysis B.*, vol. 18, p-123, **1998**.
- [77] Weitkamp, J.; Puppe, L.; Catalysis and Zeolites: Fundamentals and Applications, (Eds.), *Springer-Verlag*, ISBN 3-540-63650-1, **1999**.
- [78] Corma, A.; Inorganic Solid Acids and Their Use in Acid-Catalyzed Hydrocarbon Reactions, *Chemical Reviews*, vol. 95, p-559, **1995**.
- [79] Goralski, C. T. Jr.; Chanko, T. ; Lupescu, J.; Ganti, G.; Experimental and Modeling Investigation of Catalyzed Hydrocarbon Trap Performance, *SAE*, 2000-01-0654, **2000**.

- [80] Otto, K.; Montreuil, C. N.; Todor, O.; McCabe, R. W.; Gandhi, H. S.; Adsorption of Hydrocarbons and Other Exhaust Components on Silicalite, *Industrial and Engineering Chemistry Research*; vol. 30, p-2333, **1991**.
- [81] Koltsakis, G. C.; Stamatelos, A. M.; Modeling of Hydrocarbon Trap Systems, *SAE*, 2000-01-0655, **2000**.
- [82] Watanabe, Y.; Asano, A.; Banno, K.; Yokota, K.; Sugiura, M.; Application of Numerical Modeling of Selective NO_x Reduction by Hydrocarbon Under Diesel Transient Conditions in Consideration of Hydrocarbon Adsorption and Desorption Process, *Catalysis Today*, vol. 69, p-209, **2001**.
- [83] Czaplowski, K. F.; Reitz, T. L.; Kim, Y. J.; Snurr, R. Q.; One-dimensional Zeolites as Hydrocarbon Traps, *Microporous and Mesoporous Materials*, vol. 56, p-55, **2002**.
- [84] de Jong, A. M.; Niemantsverdriet, J. W.; Comparative Test of Procedures for Thermal Desorption Analysis, *Vacuum*, vol. 41 (1-3), p-232, **1990**.
- [85] Oh, S. H.; Bissett, E. J.; Battiston, P. A.; Mathematical Modeling of Electrically Heated Monolith Converters: Model Formulation, Numerical Methods and Experimental Verification, *Industrial and Engineering Chemistry Research*, vol. 32, p-1560, **1993**.
- [86] Bissett, E. J.; Oh, S. H.; Mathematical Modeling of Electrically Heated Monolith Converters: Model Formulation and Numerical Methods, *General Motors research publication, GMR-7582*, **1992**; Also presented at the 40th anniversary meeting of *Society for Industrial and Applied Mathematics*, CA, July 19-24, **1992**.